
THE UNIVERSITY *of* EDINBURGH

# Discovery of retinal biomarkers for vascular conditions through advancement of artery-vein detection and fractal analysis

*Devanjali Relan*

Doctor of Philosophy

University of Edinburgh

2016

# Declaration

I declare that this thesis has been composed by myself and that the work contained therein is my own, except where explicitly stated otherwise in the text. I declare that it has not been submitted, either in whole or in part, in any previous application for a degree. I confirm that where I have consulted the published work of others, this is always clearly attributed. I have taken good care to acknowledged all main sources of help.

( *Devanjali Relan*)

# Abstract

Research into automatic retina image analysis has become increasingly important, not just in ophthalmology but also in other clinical specialities such as cardiology and neurology. In the retina, blood vessels can be directly visualised non-invasively in-vivo, and hence it serves as a "window" to cardiovascular and neurovascular complications. Biomarker research, i.e. investigating associations between the morphology of the retinal vasculature (as a means of revealing microvascular health or disease) and particular conditions affecting the body or brain could play an important role in detecting disease early enough to impact on patient treatment and care. A fundamental requirement of biomarker research is access to large datasets to achieve sufficient power and significance when ascertaining associations between retinal measures and clinical characterisation of disease.

Crucially, the vascular changes that appear can affect arteries and veins differently. An essential part of automatic systems for retinal morphology quantification and biomarker extraction is, therefore, a computational method for classifying vessels into arteries and veins. Artery-vein classification enables the efficient extraction of biomarkers such as the Arteriolar to Venular Ratio, which is a well-established predictor of stroke and other cardiovascular events. While structural parameters of the retinal vasculature such as vessels calibre, branching angle, and tortuosity may individually convey some information regarding specific aspects of the health of the retinal vascular network, they do not convey a global summary of the branching pattern and its state or condition. The retinal vascular tree can be considered a fractal structure as it has a branching pattern that exhibits the property

of self-similarity. Fractal analysis, therefore, provides an additional means for the quantitative study of changes to the retinal vascular network and may be of use in detecting abnormalities related to retinopathy and systemic diseases.

In this thesis, new developments to fully automated retinal vessel classification and fractal analysis were explored in order to extract potential biomarkers. These novel processes were tested and validated on several datasets of retinal images acquired with fundus cameras.

The major contributions of this thesis include: 1) developing a fully automated retinal blood vessel classification technique, 2) developing a fractal analysis technique that quantifies regional as well as global branching complexity, 3) validating the methods using multiple datasets, and 4) applying the proposed methods in multiple retinal vasculature analysis studies.

# Lay Summary

Retinal imaging provides relatively inexpensive means to view inside the human body and observe the activity of blood vessels closely. Thus, through the human eye, a small window exists into which one can study diseases and conditions which affect the blood vessels, with bearing on the health of the heart, kidneys and brain. By developing a software to detect features that reveal the state or condition of retinal blood vessels, the possibility for retinal imaging to be used in the large-scale screening programmes to help detect early onset of conditions such as, for example, heart disease and dementia seems both feasible and achievable.

The changes that appear in the human eye during the onset of various conditions can affect the small retinal arteries and veins differently. It is therefore important to classify retinal blood vessels into arterioles and venules for the computerised analysis so that tell-tale signs or markers of disease might be determined. Further, fractal analysis provides a means of analysing the vessels by measuring how complex (or not) the circulatory system is in the retina, with direct relevance to vascular health elsewhere in the body and brain.

The focus of this thesis was to devise new computer processes (software's) to identify retinal blood vessel features from retinal images which reveal disease, with the potential to impact on early detection of disease as well as diagnosis and the management of treatments. Against this backdrop, new developments to fully automated retinal vessel classification and fractal analysis were enacted. These novel process were then tested and validated on several datasets of retinal images.

*To my loving daughter,* ***Saranya Relan***

# Acknowledgement

First of all, I would like to take this opportunity to express my sincere gratitude to my supervisor, Dr. Tom MacGillivray for his excellent guidance, helpful insights, valuable support and time throughout my Ph.D research. I want to thank him for his immense understanding and patience in accommodating all my requests and needs throughout the research process. I am thankful to him for helping me during the writing of this thesis and for proof reading.

Besides my supervisor, I would like to express my deep gratitude to Prof E. Trucco with whom I enjoyed discussing different ophthalmic research aspects. I would like to thank him for his bright research ideas that he provided during my research work. My sincere thanks goes to Dr. Tom MacGillivray and Prof E. Trucco, who provided me an opportunity to join their team and for their constant encouragement and advice. Without their precious support it would not be possible to conduct this research.

I would like to thank my colleagues Gavin Robertson and Lucia Ballerini for their support and stimulating discussions. I would like to thanks all the people who participated in retinal meetings for their useful suggestions and discussions. Many thanks to Ms. Clair Young for being able to solve just about anything administrative while I concentrated on my research.

I would like to thank my loving husband for being next to me in so many different ways throughout this research journey. I really enjoyed the technical discussion with him which gave me new ideas to move further into my research work. This journey

would not be smooth without his support and care. I would like to express my special thanks to my mother-in-law who despite being ill supported herself alone in India while I concentrated on my research.

I would like to extend special thanks to my parents for their love and support and for listening to my cries on the phone when I was home sick and for helping to cheer me up and encouraging me to continue on with my research.

I would like to express my thanks to my beloved daughter Saranya Relan, a source of unending joy and love, for being such a good girl throughout the dissertation process. I am also thankful to the people whom I did not mention, but have had a valuable contribution in this research.

This research would not have been possible without the financial support from Leverhulme Trust. Last but not the least, I thank the University of Edinburgh for giving me this great opportunity. I feel proud to have been part of this excellent institution.

Thank you all very much!

# Contents

# List of Figures

# List of Tables

# Acronyms

| | |
|---|---|
| **1D** | One-dimensional |
| **2D** | two-dimensional |
| **3D** | Three-dimensional |
| **AF** | Autofluorescence |
| **AI** | Asymmetry Index |
| **AMD** | Age-related Macular Degeneration |
| **AVR** | Arteriolar to Venular width Ratio |
| **BA** | Bland Altman |
| **BC** | Branching Coefficient |
| **BCM** | Box-Counting Method |
| **BP** | Blood Pressure |
| **CHD** | Coronary Heart Disease |
| **CI** | confidence interval |
| **CRAE** | Central Retinal Artery Equivalent |
| **CRVE** | Central Retinal Vein Equivalent |
| **DRIVE** | Digital Retinal Images for Vessel Extraction |

**EM** Expectation-Maximisation

**FA** Fluorescein Angiography

**FD** Fractal Dimension

**FFA** Fourier fractal analysis

**FFD** Fourier fractal dimension

**FLD** Fisher Linear Discriminant

**FN** False Negative

**FoV** field of view

**FP** False Positive

**GMM** Gaussian Mixture Model

**GMM-EM** Gaussian Mixture Model with an Expectation-Maximisation

**HLDA** Heteroscedastic Linear Discriminant Analysis

**HSL** Hue Saturation Lightness

**HSV** Hue Saturation Value

**INSPIRE-AVR** Iowa Normative Set for Processing Images of the Retina

**kNN** k-Nearest Neighbour

**LDA** Linear Discriminant Analysis

**LOA** Limit of agreement

**LPI** Locality Preserving Indexing

**LPP** Locality Preserving Projection

**LS** Laplacian Score

**LS-SVM** Least Square-Support Vector Machine

**max** maximum

**MFA** Multifractal Analysis

**MG** Mean of Green

**MH** Mean of Hue

**MICI** Maximal Information compression index

**min** minimum

**MR** Mean of Red

**MRI** Magnetic Resonance Imaging

**NN** Neural Network

**NPDR** Non-proliferative Diabetic Retinopathy

**OCT** Optical Coherence Tomography

**OCT-A** OCT Angiography

**OD** Optic Disk

**OLPP** Orthogonal Locality Preserving Projections

**ORCADES** Orkney Complex Disease Study

**PCA** Principal Component Analysis

**QDA** Quadratic Discriminant Analysis

**RGB** Red Green Blue

**RMSD** Root Mean Square Deviation

**ROC** Receiving Operating Characteristics

**ROI** Region Of Interest

**SLO** Scanning Laser Ophthalmoscopy

**SMI** Squared-loss Mutual Information

**SMIC** Squared-loss Mutual Information Clustering

**STARE** STructured Analysis of the REtina

**std** standard deviation

**SVM** Support Vector Machine

**TN** True Negative

**TP** True Positive

**VAMPIRE** Vasculature Assessment and Measurement Platform for Images of the REtina

**VR** Variance of Red

**WMH** White Matter Hyperintensities

# Chapter 1

# Introduction

## 1.1 Motivation

A number of systemic diseases such as diabetes and cardiovascular disease not only affect the retina (through diabetic retinopathy and hypertensive retinopathy, respectively) but they are also the leading causes of morbidity and mortality in economically developed nations, leading to thousands of premature deaths per year [1] [2] [3] [4]. Furthermore, neurodegenerative diseases affecting the retina such as glaucoma and macular degeneration lead to blindness if left untreated [3] [5] [6], while debilitating conditions linked to cerebral vascular disease such as lacunar stroke and vascular dementia also have retinal manifestations [7]. In order to reduce the burden associated with these devastating conditions, there is a need to predict who is at risk or to spot the early stages of disease and target clinical interventions. Thus the identification of discriminatory biomarkers is highly prized.

Retinal imaging provides a non-invasive, in-vivo assessment of the human body's microcirculation, thus offering the means for examining microvascular health [2] [8] [9]. Different imaging methods or modalities reveal, amongst other features, the retina's vascular structure. These include fundus photography, scanning laser ophthalmoscopy (SLO), optical coherence tomography (OCT), fluorescein

angiography (FA), autofluorescence (AF) and more recently, OCT Angiography (OCT-A). The detection and characterisation of the retinal vascular structure from imaging can be used to quantify the presence and severity of many vascular disorders in the retina [3] [5] [10], brain [3] [11] [12] [13] [14] [15] [16] and body [17] [18] [19] [20]. Developments in retinal image processing and automated diagnostic systems open up the possibility for retinal imaging to be used in the large-scale screening programmes to detect early onset of otherwise debilitating conditions, with substantial resource savings and significant impact on healthcare [21].

The focus of this thesis is to devise a framework and algorithms to aid the identification of retinal vascular biomarkers (i.e. subtle changes in features such as vessel widths, tortuosity, and the complexity or sparsity of the vascular network) measured in images of the retina taken with fundus camera imaging, which may aid early detection or characterisation of diseases with vascular components. If retinal image analysis can help in determining disease progression, then retinal biomarkers could also be used in diagnosis and the management of treatments. Software tools which can process large numbers of images in an efficient and reliable manner are in great demand as manual measurements of retinal features are not only time-consuming and laborious, but may also miss the often subtle markers of vascular change and disease. Manual assessment of the retinal vasculature further impedes the analysis of the large numbers of patients needed to power the biomarker discovery process, which an effective computational analysis system could more readily deliver.

Crucially, the vascular changes that appear during the onset of disease often affect arteries and veins differently [3] [20] [22] [23]. For example, the pathophysiological changes in the retina in response to blood pressure elevation, referred to as hypertensive retinopathy, results in retinal arteriolar narrowing in which the arteriolar to venular width ratio (AVR) decreases [24] [25], while wider venules are associated with an increased risk of vascular dementia [26]. It is, therefore, essential to classify vessels appearing in images of the retina into arterioles and venules in order to extract clinically useful biomarkers from the eye. Further, the human retinal vasculature displays fractal properties [27] [28]. Studies have shown that the fractal

dimension quantified from the retina can reveal vascular changes, and so measuring this (through fractal analysis) is a further potential source of biomarkers [29] [30].

## 1.2 Aims and Objectives

One of the key objectives investigated in this thesis is the development and implementation of automatic artery-vein classification in fundus camera images. This work is geared towards enabling efficient and accurate AVR and other biomarker quantification for the VAMPIRE (Vasculature Assessment and Measurement Platform for Images of the REtina) software [12].

A number of automatic retinal image analysis algorithms have been proposed for extracting the vascular structure and measuring different morphological parameters [1] [25] [31] [32]. A common approach to adopt in vessel classification is *supervised* classification [33][34][35], but in spite of high levels of accuracy such algorithms require large volumes of clinical annotations (i.e. manual labelling of vessels into veins and arteries) to generate the requisite training data. In practical terms this is often not very easy to source and thus an *unsupervised* approach to classification (i.e. without the need for training data) is proposed in this thesis along with a *supervised* one that only requires a small amount of training.

The second key objective of this thesis is to investigate and implement novel fractal analysis, with a focus on distinguishing between normal and pathological vascular patterns in retinal images. This thesis looks at whether different regions of the fundus might hold discriminatory power compared to what has previously been reported.

Against this backdrop, the main aims of the thesis are to:

1. Develop, validate and test *supervised* and *unsupervised* artery-vein classification (a/v) framework.

2. Implement and test AVR measurements, utilising artery-vein classification.

3. Develop, validate and test different approaches for fractal analysis as a source of retinal biomarkers for disease.

## 1.3 Outline of thesis

This thesis is organised as follows:

In Chapter 2, the anatomy of the retina is introduced along with the main modes or methods of imaging the retina. Common features or indicators of disease in the retinal are also discussed. Chapter 3 reviews related work in the fields artery-vein classification, AVR and fractal analysis. Algorithms to calculate the AVR are also introduced. Chapter 4 presents the artery-vein classification framework that has been developed for fundus camera images, which utilises both unsupervised and supervised approaches. Chapter 6 presents the two methods adopted for fractal analysis and describes how these are used to investigate regional changes in vascular network complexity. Chapter 5 details the results of artery-vein classification and the measurement of AVR. Chapter 7 presents the results of fractal analysis. The thesis concludes with Chapter 8 which summarises the findings of the work and suggests areas for future investigation.

# Chapter 2

# The Retina

## 2.1 Introduction

It is possible to acquire images of the back of the eye or retina non-invasively using low cost imaging devices and observe small blood vessels inside the human body. The retina is thus a unique and accessible site for studying systemic and brain diseases with vascular components to their pathophysiology. To start, section 2.2 of this chapter gives an overview of the key anatomy of the human eye. In section 2.3, the principal modes or techniques of retinal imaging are introduced while in section 2.4, various pathologies along with their respective appearances in retinal imaging are discussed. Section 2.5 gives an overview of different processing and analysis techniques for analysing retinal images. Finally, conclusions are summarised in section 2.6.

## 2.2 Anatomy of the Eye

The human eye has a number of key components such as the retina, cornea, iris, pupil, lens, macula, optic nerve, choroid and vitreous (see Figure 2.1). In an adult human, the retina is around 22mm in diameter and approximately spherical in shape. The retina,

which is the inner surface of the eye, is a light sensitive tissue [17].

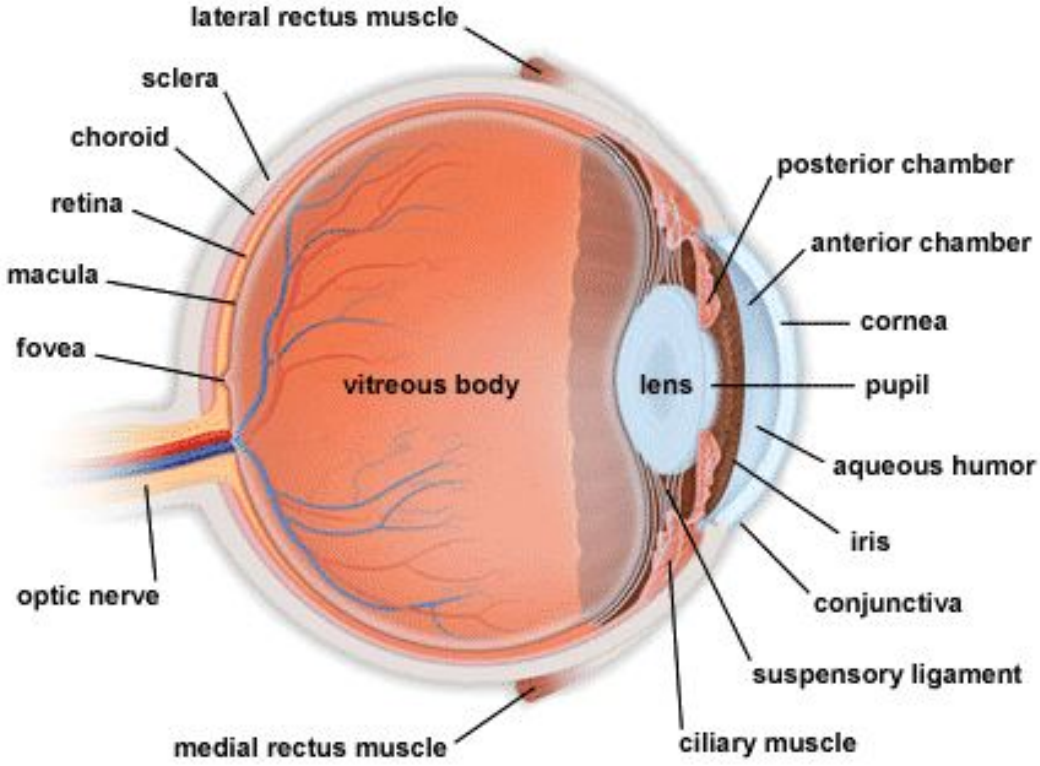


Figure 2.1: Schematic view of the anatomy of the eye showing its key anatomical components (source: [36])

The cornea transmits and focuses light into the eye, while the iris regulate the amount of light reaching the retina by controlling the diameter and size of the pupil [39]. The lens focuses the light rays onto the retina, which contains photosensitive cells that convert incident light into signals which are carried by the optic nerve to the visual cortex of the brain [39] [40] [41].

The fovea, which is located in the middle of the macular region on the retina, is responsible for the sharp central vision. The macula contains special light-sensitive cells which help to visualise fine details [39]. The optic nerve is the point where the small blood vessels pass into and out of the retina and is located 3 to 4 mm to the nasal side of the fovea [39].

The output neurons of the retina are known as ganglion cells and these are located in the innermost layer of the retina, closest to the lens. See Figure 2.2(a). The photosensors or photoreceptors, the rods and cones, are located in the outermost

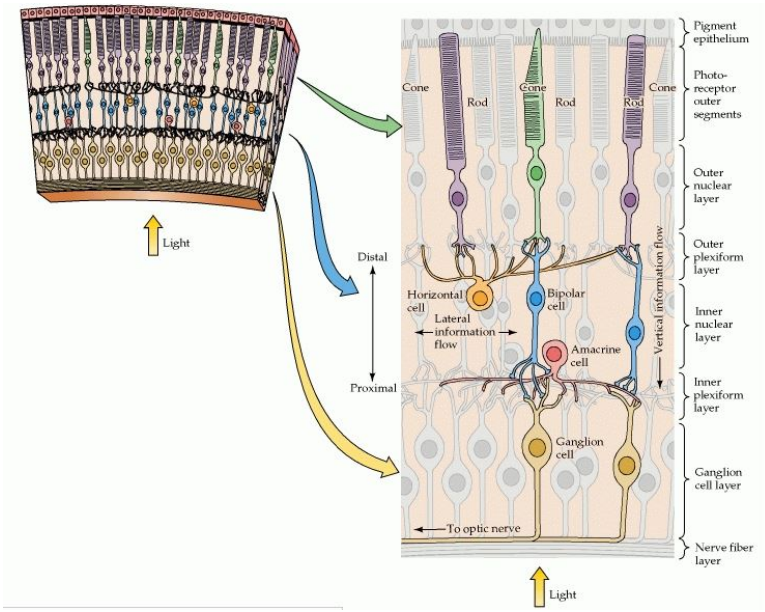


(a)

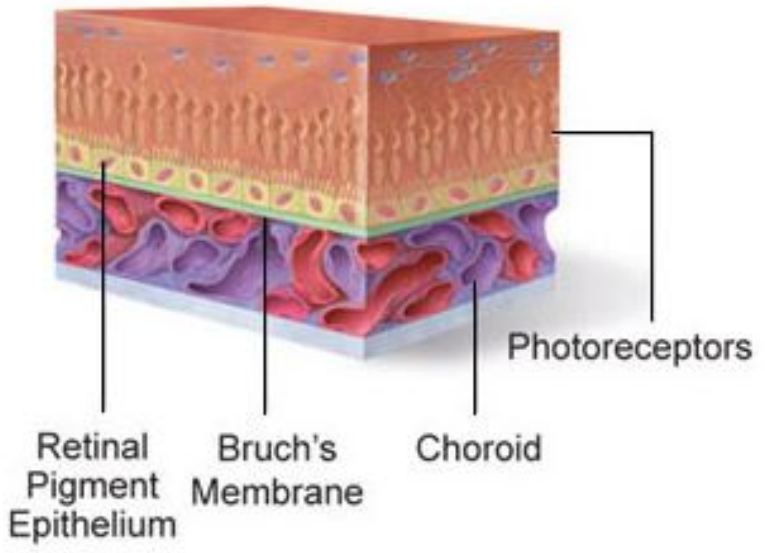


(b)

Figure 2.2: (a) The layers of the retina (source: [37]). Light enters from the bottom and passes through all the superficial layers before it reaches the photoreceptors: rods and cones. (b) The basic structure of the retina showing the main retinal layers (source: [38]).

layer against the pigment epithelium and choroid [42]. See Figure 2.2(b). Thus light first passes through the thickness of the retina before it strikes the rods and cones. The photoreceptors convert light into a biochemical message and then to an electrical message due to absorption of photons by the visual pigment [42]. These electrical messages stimulate all the succeeding neurons of the retina. The retina creates a message concerning an input image projected onto its surface and transforms it into nerve impulses which are then transmitted to the brain from the spiking discharge pattern of the ganglion cells [42].

## 2.3 Imaging the Retina

The retinal vasculature is the only part of the human circulation that can be directly visualised non-invasively in vivo [21] [39]. Thus retinal imaging is an accessible means of examining micro-vascular health and systemic disease [2] [21] [39] [43]. Furthermore, retinal blood vessels share similar anatomic, physiological, and embryological characteristics with cerebral blood vessels and may act as a surrogate marker for them [7] [44]. Hence the retina reflects pathological changes that occur due to microvascular disease with conditions such as diabetes, hypertension [7] [43] [45], stroke [46], dementia and Alzheimer's disease [1] [3] [14] [25] [26] [47]. It has already been shown in various studies that quantitative structural analysis of the retinal vasculature (i.e. extracting different morphological measurements or parameters) aids the characterisation of pathological condition of the retinal and other vascular systems [1] [14] [25] [26] [47] [48] [49]. For example, narrowed retinal arterioles are associated with hypertension [14] [50].

For acquiring images of the retina, different imaging machines and modes are available. This section introduces some of the main techniques and outlines the principal imaging technologies.

1. Fundus Photography

A fundus camera generates a two-dimensional (2D) image of the interior three-dimensional (3D) surface of the eye or retina. Fundus photography involves the use of a digital camera to photograph the regions of the retina containing the optic nerve and macula, i.e. the fundus. It is the most commonly used technique in ophthalmological imaging [41] and the main source of images studied in this thesis. A typical fundus photograph is shown in Figure 2.3

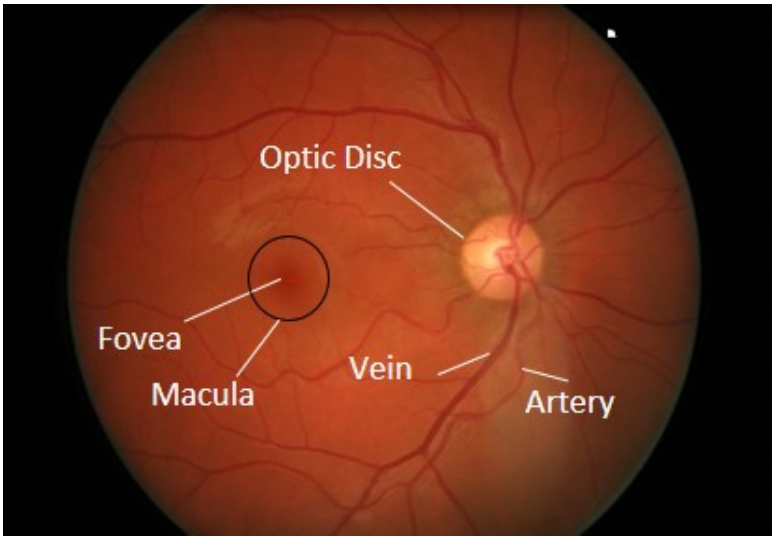


Figure 2.3: An example of an image acquired via fundus photography showing the fovea, optic disc, and macula. An artery and a vein are also labelled. It can be noticed that arteries are brighter and thinner than veins [33].

The optic nerve head or optic disk (OD) appears as a bright region in the image, where all the blood vessels emanate and converge. The macula is a dark region where few blood vessels are present. The retinal vasculature - arterioles and venules, have different appearance or features, which helps to distinguish them from each other. Arterioles are a slightly brighter red in colour and thinner than venules, which have a darker and fatter appearance. Also, the central reflex (i.e. the bright strip commonly seen in the centre of a vessel) is more often obvious in arterioles since they carry blood rich in oxygen [6] [33] [51].

Fundus images can be taken with either a mydriatic or a non-mydriatic camera. For imaging using the former, the pupil is dilated with eye drops before in order to get an acceptable view of the retina to photograph. There is no need to dilate

with a non-mydriatic camera, though eye drops can sometimes be used to get better quality pictures. The field of view (FoV), i.e. the extent by which the retina can be observed at any given moment (and is measured as a viewing angle), is usually between $30\,^{\circ}$ to $50\,^{\circ}$ depending on the optics of the imaging system used. To capture a fundus image, the retina is illuminated (typically by a flash of the white light) and the reflected light is captured via the system's optics by a digital sensor or camera.

Retinopathy such as haemorrhages, exudates and cotton wool spots can be detected using fundus photography. Hence, fundus photography is commonly used in screening programmes (e.g. diabetic retinopathy) where the photos are used to monitor the progression of pathology. In a screening programme, where hundreds of thousands of fundus photographs might be taken, it is laborious work for the ophthalmologist to manually examine or grade each and every photo. Hence semi-automatic methods have already been introduced to partially alleviate the workload [12] [52].

2. Fluorescein Angiography (FA)

   FA is a technique for examining the circulation of the retina using fluorescent dye tracing [53]. Though the imaging technology is still a fundus camera, it is an invasive method that involves injection of sodium fluorescein into the systemic circulation. Images are taken after dye is injected into the patient′s arm. The dye then eventually flows through the blood vessels in the retina. The dye absorbs the blue spectrum (465-490 nm) of the illuminating light source and emits or fluoresces yellow-green light. An angiogram is obtained by photographing the fluorescence as the dye travels through the blood vessels by taking a series of retinal images in quick succession [17] [40]. This yields high-contrast images such as the one shown in Figure 2.4. Use of FA can have serious side effects including nausea and in rare cases death from anaphylaxis [17] [41] [54].

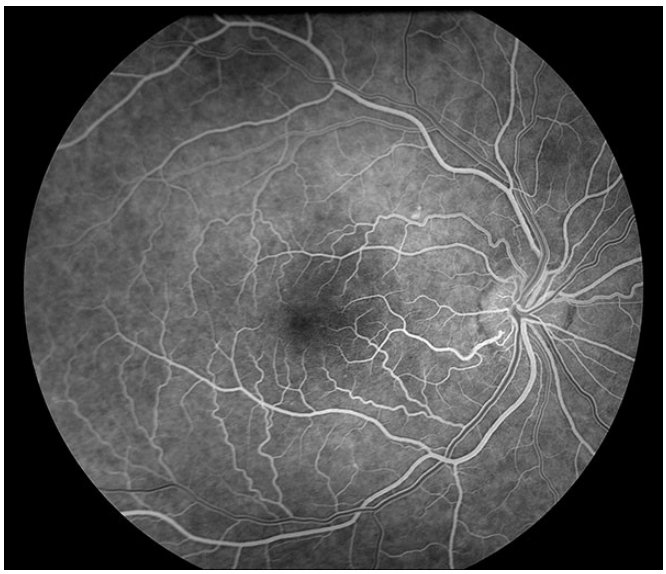

Figure 2.4: An example of a fluorescein angiogram showing retinal blood vessels illuminated with fluorescing dye (source: [55]). The blood vessels are clearly observed, exhibiting a high contrast difference with that of the surrounding retinal background.

3. Scanning Laser Ophthalmoscopy (SLO)

   SLO, like fundus photography, creates a 2D image of the retina, but instead uses confocal laser scanning microscopy and scans a laser beam across the retinal surface [41] [54] [56]. The retina is scanned point by point and the reflected light is captured through a small aperture called the confocal pinhole. This prevents blurring of the image by suppressing light scattered from outside of the focal plane. Regions of the retina not accessible with fundus photography are reachable using scanning mirrors to direct the laser beam [41]. FoV varies by instrument but can be comparable to a fundus camera (i.e. $45\,^{\circ}$ - $65\,^{\circ}$) right up to $200\,^{\circ}$ which is commonly referred to as the ultra-widefield [41]. Figure 2.5 shows an example of a SLO image.

4. Optical Coherence Tomography (OCT)

   OCT captures cross-sectional images of the internal retinal layers using infrared light and interferometry, and is also useful for monitoring retinal physiology [17] [41] [40]. Various studies have been performed which show the feasibility of OCT for the diagnosis and monitoring of many retinal diseases such as glaucoma, macula holes, macular edema, age-related macular degeneration

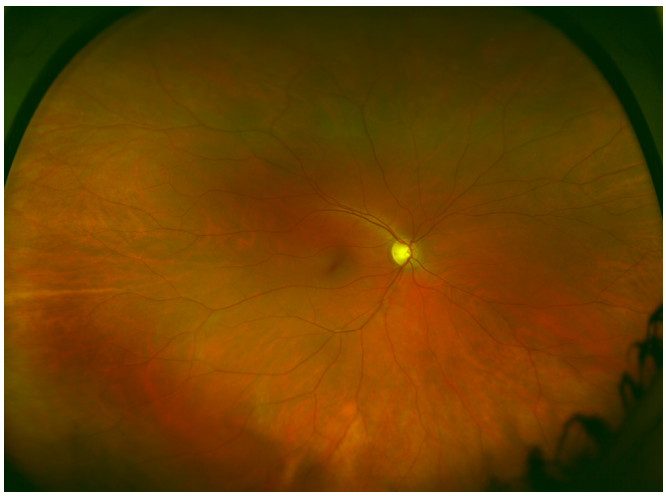

Figure 2.5: An example of an ultra-widefield SLO image showing the OD, fovea and retinal vasculature (source: [57]). The larger area of coverage compared to the fundus camera is clearly observable, though at a sacrifice to image resolution i.e. the SLO images more of the retina in one go, but the fundus camera reveals more detail, albeit over a smaller region.

(AMD) and optic disc pits [58] [59] [60] [61] [62] [63] [64] [65] [66]. An example of an OCT image is shown in Figure 2.6.

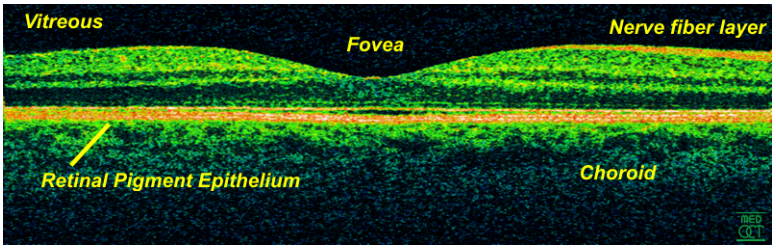


Figure 2.6: Optical coherence tomography of retina. Red region shows high reflectivity, black shows low reflectivity region while green indicates region of intermediate reflectivity (source: [67]).

## 2.4 Retinal Pathologies

Retinal pathologies may affect one or more of the retinal landmarks as observed with a fundus camera - i.e. macula, OD and vasculature [40]. Some of the common eye problems affecting our society today are cataracts, glaucoma, AMD and diabetic retinopathy [40] [68]. Abnormalities (vascular and retinopathy) and their manifestation

in fundus camera imaging (the main source of images in this thesis) are presented in the following section.

### 2.4.1 *Vascular abnormalities*

Retinal microvascular abnormalities such as arteriovenous nicking, arteriolar narrowing and venular dilation are often related to conditions such as hypertension, diabetes [2] and dementia [26]. The key observable (and measurable) features are described below.

1. Tortuosity

   Retinal blood vessels are normally straight or gently curved but in certain diseases such as in high blood flow, angiogenesis and blood vessel congestion, the blood vessels become dilated and take on a serpentine path, i.e. they become tortuous [31]. This occurs due to radial and longitudinal stretching of the blood vessels [31]. This change or abnormality may occur in only small regions of retinal blood vessels or it may affect the entire retinal vascular tree [31]. Tortuosity can have very different course in arteries and veins while retinopathy progresses [69]. Figure 2.7 shows an example of the fundus camera images with tortuous and non-tortuous blood vessels.

2. Generalised Arteriolar Narrowing

   In generalised arteriolar narrowing the ratio between the diameters or calibres of the retinal arteries to the veins decreases [69]. This is one of the early signs of retinopathy [70]. For example, in hypertension the earliest retinal vascular change is the thinning of the retinal arterioles. Narrowing of the arterioles is usually directly proportional to the degree of elevation of blood pressure [69].

3. Focal Arteriolar Narrowing

   Local irregularities in the calibres of retinal blood vessels is known as Focal Arteriolar Narrowing [69]. It appears as a thinning or narrowing of the blood

(a)

(b)

Figure 2.7: Examples of fundus camera images showing (a) tortuous vessel (indicated by arrows) and, (b) normal vessels.

column in specific or localised areas. See Figure 2.8.

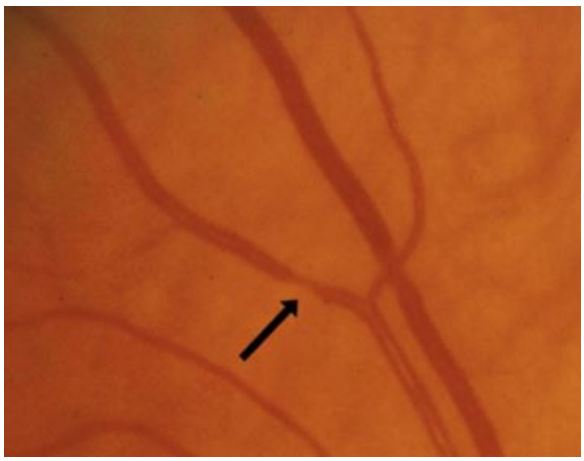

Figure 2.8: Section of a fundus camera image showing an example of focal arteriolar narrowing (indicated by the arrow) (source: [71]).

4. Suboptimal Bifurcations The branching or bifurcation angle is the angle between the two daughter vessels [72] [73] [74]. See Fig. 2.9(a). In order to achieve the fastest transport of the blood for the least amount of work, the optimum bifurcation angle between the vessel branches is naturally formed. The optimum value of this angle is widely considered to be $72^\circ$ and it is dependent upon the energy spent in blood transport, the diffusion distance and the efficiency of flow [72] [73] [74]. If the bifurcation angle becomes too large then the efficiency of flow decreases. The deviation of branching angles from the optimum value may suggest vascular abnormalities in the presence of disease [69] [74] such as in the case of diabetic retinopathy (see Figure 2.9(b)). The retinal vessel width relationship at the vessel branching points is another important biomarker of microvascular health, and has associations with conditions such as ischaemic heart disease and hypertension [24] [75]. Increased arteriolar branching coefficient (i.e. the ratio of the sum of the cross-sectional areas of the two daughter vessels to the cross-sectional area of the parent vessel [76]) has previously be found to be associated with periventricular white matter hyperintensities (an indicator of poor cerebral vascular health) and ischaemic heart disease, and decreased branching coefficient with deep white matter hyperintensities (i.e. poor brain health) [75].

5. Arteriovenous Nicking

   Arteriovenous nicking occurs when an arteriole cross and compresses a venule with a bulge on either side of the crossing. The arteriole's thicker walls push against those of the venule forcing the venule to collapse. This is an irreversible long-term marker of hypertension and sclerosis [78]. Compression of an underlying venule by an overlying arteriole may impede the blood return, so that the venules become distended. This is the so called Gunn's sign [69] [79]. In Salus's sign, venules cross arterioles at the right angle and appears as S-shaped at the bend instead of crossing arterioles obliquely. In Salus's sign, deflection of the venules from its normal course at the crossing point take place [69] [79]. Figure 2.10 shows examples in the retinal vasculature.

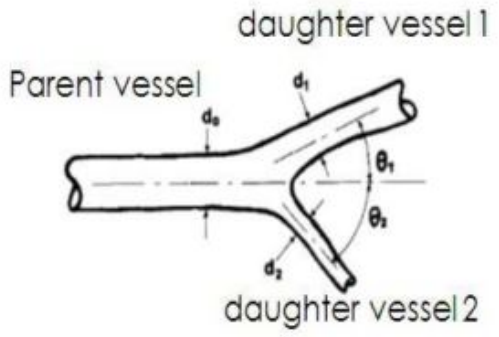


(a)

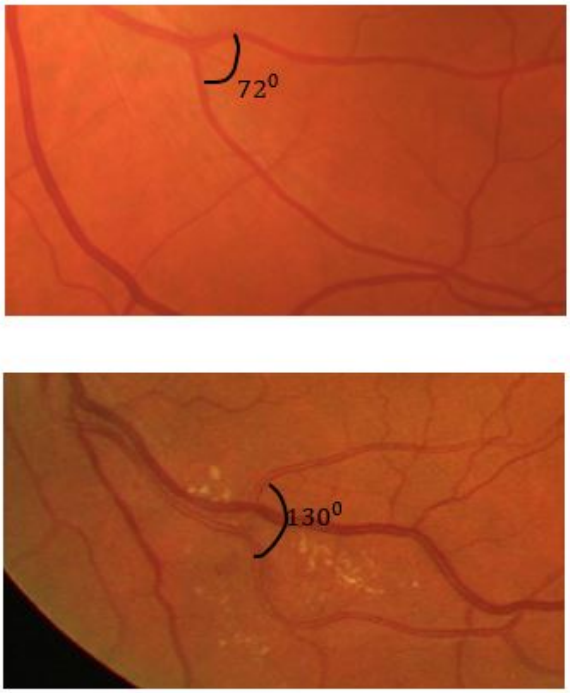


(b)

Figure 2.9: (a) Diagram illustrating the measurements of retinal vessel branching angle and branching coefficient (source: [77]) (b) Measurements of bifurcation angles in fundus camera images for a normal person (72 °) and a person with diabetic retinopathy (130 °)

.

6. The Arteriole-to-Venule Ratio (AVR)

   AVR is defined as the ratio of the arteriole width to the venular width and it is used to quantify global changes to vessel diameters [1] [78]. It is determined by measuring the diameters or calibres of a sample of arteries and veins appearing in fundus camera images [1]. An AVR of 1.0 indicates that arteriolar diameters are, on average, the same as venular diameters, and a smaller AVR indicates either

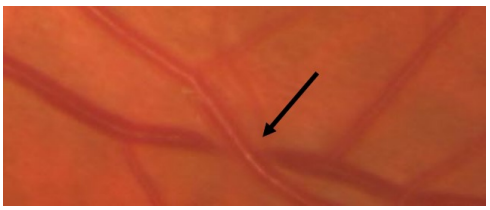

(a)

(b)

Figure 2.10: Sections of fundus camera images showing examples of (a) Gunn′s sign - vein compression and (b) Salus′s sign - vein deflection (source: [80]).

a narrower arteriole, relative to venule, or a wider venule relative to arteriole [46]. A smaller AVR, reflecting narrowed arterioles or enlarged venules, is associated with risk of incident stroke [81] and coronary heart disease (CHD) [22]. Decreased retinal arteriolar calibre is associated with hypertension [46], while larger retinal venular calibre has been associated with inflammation, smoking, hyperglycaemia, obesity, dyslipidaemia [1] [20], dementia [26] and Alzheimer's disease [47]. AVR is also inversely related to higher blood pressure levels [82] [83]. There are various ways of calculating AVR, which is discussed in more detail in section 3.3 for further discussion on this.

### 2.4.2 *Retinopathy*

Retinopathy is persistent or severe damage to the retina and frequently occurs in the eye due to systemic disease such as diabetes or hypertension. The main manifestations detectable with fundus camera imaging are described below.

1. Microaneurysms

   A retinal microaueurysm is a dilation of a capillary wall and shows an area of deficient capillary cell wall. They appear as small red dots in a fundus camera image. It may be associated with abnormal vascular leakage [84] and is a proven earliest lesion indicator of diabetic retinopathy [69]. See Figure 2.11(a).

2. Haemorrhages

   Retinal haemorrhages are blood deposits on the retina and occur due to the breaking of a vessel wall or a microaneurysm. They can be caused by hypertension, retinal vein occlusion or diabetes mellitus. They have very different shapes [69]. Haemorrhages can spread out on the retinal surface where they take on a flame appearance [84]. Haemorrhages disappear, if the blood is reabsorbed with time and in such situations haemorrhage margins fade. In such cases the characteristic red colour turns to a faint greyish-red before it disappears completely [69]. Figure 2.11(a) shows an example.

3. Hard Exudates

   Exudates are deposits of lipoproteins caused by abnormal vascular leakage and appear as white or yellowish-white with sharp margins [69]. They occur in the diabetic retinopathy. See Figure 2.11(a) Precipitation of lipids and proteins diminishes the extravascular fluid which increases the number of exudates [84]. They may appear as individual dots, confluent patches or rings surrounding microanaeurysms [69].

4. Cotton Wool Spots

   Cotton wool spots are small round or oval whitish fluffy superficial lesions that are a result of the retinal ischaemic events, due to precapillary arterioles stenosis [69] [84]. Diabetes and hypertension are the two most common diseases that cause these spots. These spots occur due to the swollen nerve axons caused by a localised obstruction of the blood supply in the nerve fibre layer [69]. They obscure underlying blood vessels [84] and usually appear along the major vessel

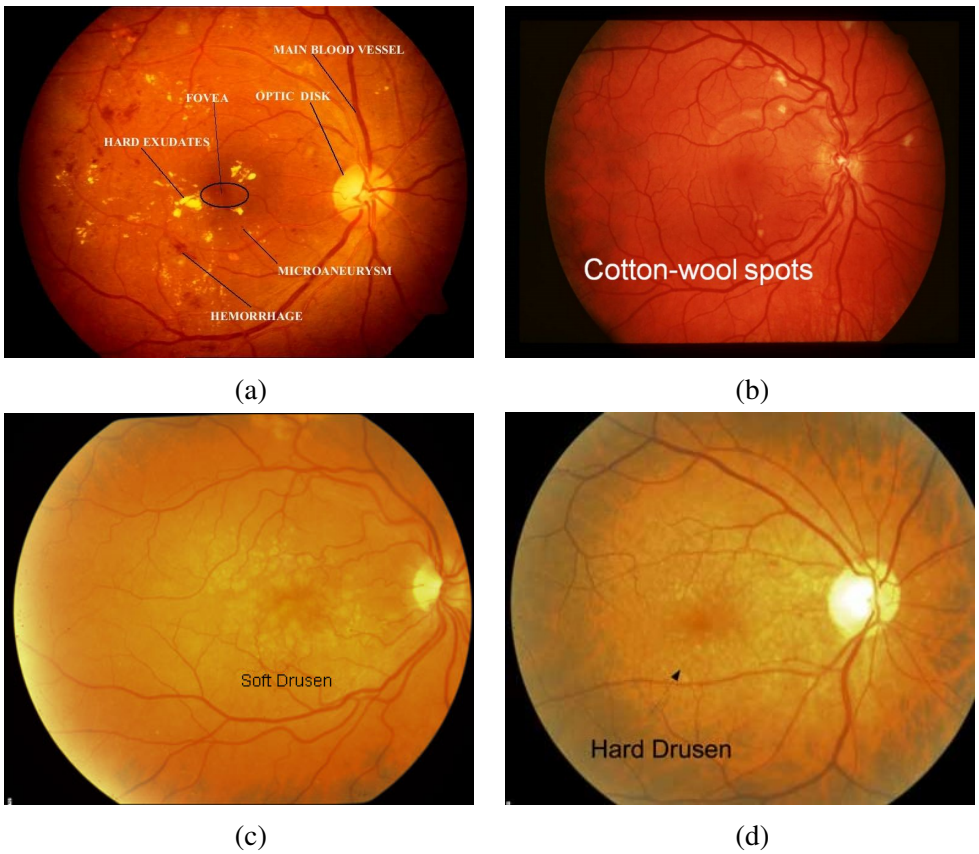


(a) (b)

(c) (d)

Figure 2.11: Examples image showing different Retinopathies (a) Microaneurysms Haemorrhages and Hard Exudates (source: [86]), (b) cotton-wool spot (source: [87]), (c) Soft Drusen (source: [88]) and (d) Hard Drusen (source: [88]).

arcades, parallel to the nerve fibres [69]. See Figure 2.11(b).

5. Drusen

   Drusen are usually round with deep yellowish-white dots that exist in a layer called Bruch's membrane (see Fig. 2.2(b)), which lies beneath the retina and the adjacent retina pigment epithelium layer [69] [85]. Figure 2.11(c) and 2.11(d) shows an example. Drusen are associated with ageing and macular degeneration. They are found both in the macula and the peripheral retina. Drusen are deposits associated with the thinning or the hypopigmentation of the retinal pigment epithelium [69].

## 2.5 Retinal Image Analysis

Vascular changes in the retina are often very subtle and may be missed by visual observation and conventional retinal image inspection or grading. In addition, certain quantitative measures such as tortuosity and fractal dimension cannot be calculated manually. Moreover, conducting manual measurement is very time-consuming, which significantly hinders the analysis of the large numbers of images. Therefore, an automated system with advanced image processing capabilities is needed to compute parameters in an objective, effective and efficient manner.

### 2.5.1 Vessel Assessment and Measurement Platform for Images of the REtina

Vessel Assessment and Measurement Platform for Images of the REtina (VAMPIRE) is a software application for the efficient, (semi-) automatic quantification of the retinal vascular properties in large collections of fundus camera images. The main image processing features of VAMPIRE are an automatic segmentation of the blood vessels [89], the detection of other retinal landmarks (i.e. OD and macula/fovea vasculature), and quantification of key morphometric retinal parameters (i.e. vessel widths and tortuosity) used frequently in investigative biomarker studies [12] [52]. The software had been used for various studies including investigations into retinal microvascular abnormalities in diabetic retinopathy, stroke, cerebrovascular disease and hypertension. [7] [15] [16] [21] [75] [90] [91] [92] [93] . Most of the processing is hidden from the user, who is expected to provide only a minimal level of intervention after all the processing is completed. The work presented in this thesis on artery-vein classification, AVR and fractal analysis was designed to expand the functionality of VAMPIRE and empower biomarker investigations. The main software features of the (existing) platform are briefly explained.

1. Vascular Segmentation

   For vessel segmentation a multi-scale, 2-D Gabor wavelet is applied to emphasise the appearance of vessels, followed by the supervised pixel classification with a Bayesian classifier [89]. Thereafter, the software creates a graph or tree-like representation of the vasculature as a pre-processing step for further measurements [12].

2. Landmark Localisation

   The software locates the OD centre and fovea centre in digital fundus images based on the computation of likelihood values for pixels to be OD or fovea centre, derived from the Fast Radial Symmetry transform and vessel density estimation. OD detection is a novel algorithm based on in-painting and a symmetry transform, which performs very competitively in tests with a public data set and images from a local diabetes screening program [94] [95].

3. Vessel Width/Calibre

   An algorithm proposed by the authors of [96] is used for the accurate measurement of vessel width. It makes use of a novel parametric surface model of the cross-sectional intensities of the vessels and ensembles of the bagged decision trees to estimate the local width from the parameters of the best-fit surface.

4. Tortuosity

   The authors in [97] assessed the performance of five of the most used quantitative tortuosity indices in total, using the publicly available RET-TORT dataset [98]. Among these indices, the one offering the best performance in terms of robustness to different sampling rates and noise is represented by the mean squared curvature normalised by the vessel's arc-length to allow fair comparison among short and long vessels [97] [99]. Based on the recent work by Annunziata et al. [100], multi-scale tortuosity will be added to VAMPIRE in order to offer a new and more discriminative tortuosity measurement compared to less discriminative single-index tortuosity measure.

## 2.6 Conclusions

In this chapter the key anatomical components of the eye were introduced and described the main technologies for imaging the retina. Furthermore, important retinal abnormalities relating to microvascular and ocular health were presented with a particular focus on fundus on camera imaging, the main technology utilised in this thesis. The chapter also provided background on retinal image analysis, highlighting its importance in aiding clinical research. The main features of the VAMPIRE software for quantifying parameters in fundus camera images were also discussed.

# Chapter 3

# Retinal Image Analysis

## 3.1 Introduction

In this chapter several key approaches to retinal image analysis for fundus camera imaging are introduced and discussed. This includes automatic classification of the small retinal vessels visible in fundus images into arterioles and venules, the driving motivation behind which is presented in section 3.2 along with a review of related work in the field. Then section 3.3 discusses three different approaches for calculating the AVR, a key biomarker of vascular change relating to disease that utilises automatic vessel classification. In section 3.4 an overview of related work in the area of fractal analysis of the visible vasculature in retinal images is presented and discussed. Finally, section 3.5 concludes with a summary of this chapter.

## 3.2 Artery/Vein Classification

Quantitative structural analysis of the retinal vasculature helps in the diagnosis of retinopathies as well as provides candidate biomarkers of systemic diseases. An essential part of any computerised system used for retinal vasculature characterisation

in fundus camera images is an automatic method for classifying the small retinal vessels into arteries and veins. The retinal vessel segmentation is the preceding step to a/v classification. The vessel classification enables the extraction of useful diagnostic indicators or disease biomarkers such as the AVR, which is a well-established predictor of stroke and other cardiovascular events [14] [25] [50].

### 3.2.1 Clustering vs. Classification

There are two distinct approaches of finding hidden patterns in any data namely *clustering* and *classification*. In clustering, no prior information about the characteristics of similarity of the data (or samples) is known (or assumed) and similar variables/objects can be grouped together to achieve some degree of homogeneity within and heterogeneity between the clusters [101]. In other words, clustering is a way of grouping related data points together without labelling them explicitly. In contrast, classification is a way of assigning instances (i.e. data or samples) to pre-defined classes, i.e. a training set containing data that have been previously categorised or labelled is needed, and based on this information, a classification algorithm finds the category to which new data belong [101] [102]. This is often described as supervised learning, while clustering is referred to as unsupervised learning as no training set is required [103] [104] [105]. In order to handle high dimensional data (containing many representative features) adequately and efficiently, its dimensionality often needs to be reduced using appropriate dimensionality reduction techniques. Dimensionality reduction is mapping of a high dimensional data to a lower dimensional space such that the reduced representation has a dimensionality that corresponds to the intrinsic dimensionality of the data [106] [107]. Similar to data classification, dimensionality reduction can be achieved in either a supervised or unsupervised manner.

### 3.2.2 General Remarks

In a supervised framework, a training dataset is first generated by identifying the classes (in this case arterioles or venules) manually. This training set is then used as prior knowledge to classify new unseen data into the two classes. Use of supervised classification methods for retinal vessels have been previously reported in [33] [34] [35], but such algorithms require large volumes of manual annotations on images to generate requisite training labels and this may not be easy to source in prospective investigations. In an unsupervised setting, unseen data is classified or clustered into different classes without any prior knowledge about the data. Thus, an unsupervised framework appears to be an attractive approach to adopt for the classification of arterioles and venules. However, supervised approaches generally results in higher classification accuracy as compared to unsupervised methods [108] [109].

To discriminate between retinal vessel classes, it is generally assumed that veins and arteries are distinguishable using colour features [33] (see Fig. 3.1). A number of studies in the field of vessel classification have been performed based upon different colour features extracted from each of the channels of RGB, HSL, HSV images etc. Therefore, brief introduction to each colour channel is now presented:

- **RGB** colour space or system reproduce broad range of colour from different combination of red, green and blue colours. The red, green and blue use 8 bits each, which have integer values ranges from $0$ to $255$. Therefore, the possible colours that can be made are $256 \times 256 \times 256 = 16777216$ [110] [111].

- **HSL** (*Hue*, *Saturation*, and *Lightness*) and **HSV** (*Hue*, *Saturation*, and *Value*) are both cylindrical-coordinate representations of points in an RGB colour model. HSV is a colour model that describes colours (hue or tint expressed from $0$ to $360$ degrees representing hues of red (starts at $0$), yellow (starts at $60$), green (starts at $120$), cyan (starts at $180$), blue (starts at $240$), and magenta (starts at $300$)) in terms of their shade (saturation or amount of gray ($0\%$ to $100\%$) in the colour) and their brightness (value or luminance, or intensity of the colour from $0\%$ to

100%). This model is similar to the way in which humans perceive colour [112]. Both are mathematically cylindrical, but while HSV conceptually represented as an inverted cone of colours (with a black point at the bottom, and fully-saturated colours around a circle at the top) while HSL is represents a double-cone or sphere (with white at the top, black at the bottom, and the fully-saturated colours around the edge of a horizontal cross-section with middle grey at its centre) [113].

- **Lab** colour space is a 3-axis colour system with dimension *L* for lightness and *a* and *b* for the colour dimensions. It includes all of colours in the spectrum, as well as colours outside of human perception [114] [115].

Other features that appear to differentiate arteries from veins are: the arteries are usually thinner, brighter and present more frequently with a central light reflex (i.e. the bright strip commonly seen in the centre of a vessel as shown in Fig. 3.1). Although, the central light reflex often diminishes due to insufficient image quality or increasing age of subjects [33] and it can sometimes be present in veins. In such cases, it becomes difficult to distinguish between types of vessels using this feature.

Global features are not always effective and in many cases considering such features for vessel classification leads to misclassification. For example, in poor image quality especially in the outer region of the image, the central light reflex is not always clearly observable and the vessels themselves can appear very dark due to inhomogeneous lighting [33] (see Figure 3.2(a)). In the outer region of a fundus camera field of view, arteries and veins look very much alike (see Figure 3.2(a)) and vessels lose contrast (see Figure 3.2(b)) which results in misclassification [33]. However, structural features can sometimes be used to discriminate vessel type as, for example, arteries and veins usually alternate near the OD before branching out [33]. Though, Fig. 3.3 shows examples illustrating that the alternating pattern of arteries and veins is not always a valid discriminative feature because of branching.

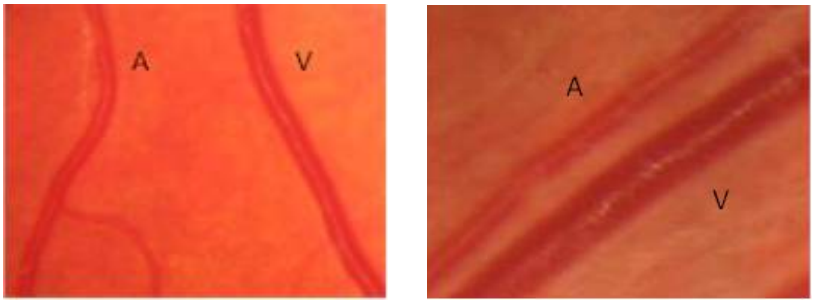


(a) (b)

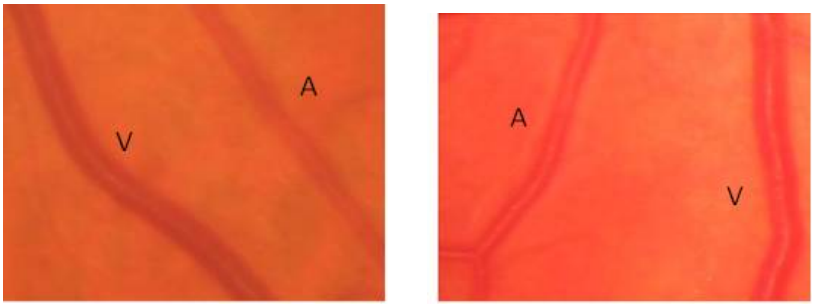


(c) (d)

Figure 3.1: Examples of arteries (A) and veins (V) in fundus images, and with a prominent central light reflex. Vessels appear distinguishable by colour and size as the arteries look thinner and lighter than the veins.

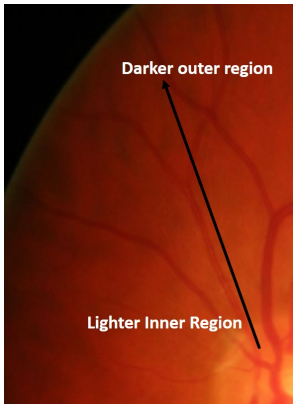


(a)

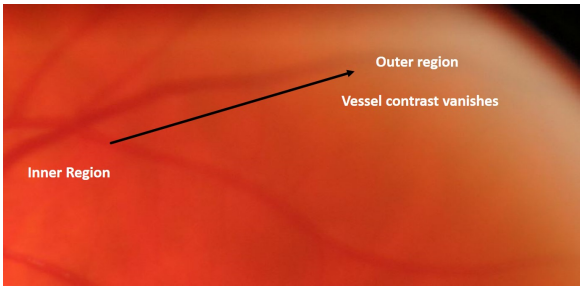


(b)

Figure 3.2: Example sections from fundus camera images showing (a) vessels that are dark and with a central reflex that diminishes and (b) vessels losing contrast as they near the extremities of the FoV.

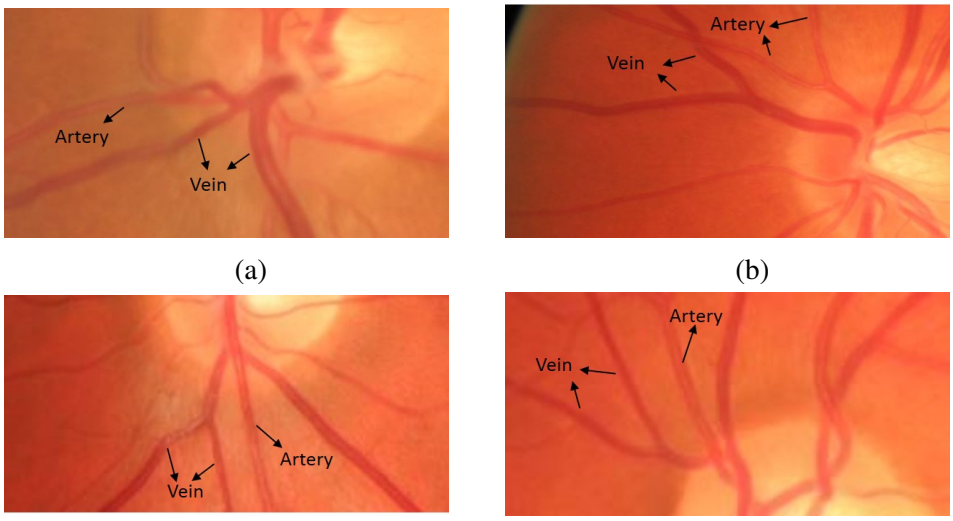


Figure 3.3: Examples sections from fundus camera images demonstrating that an alternating pattern of arteries and veins in the fundus is not always a valid discriminative feature because of instances of branching.

### 3.2.3 A Review

A variety of approaches to retinal vessel classification have been proposed based upon the use of different discriminative features and with various classification algorithms.

1. Unsupervised Clustering

   Grisan et al. proposed an automatic unsupervised method for quadrant-wise vessel classification in a concentric zone around the optic disc using fuzzy C-Mean clustering on $443$ vessels from $35$ images, and reported $87.6\%$ correct classification [70]. Two colour features (mean of Hue and variance of Red from the HSL and RGB colour spaces, respectively) were used in different sectors for vessel classification. This was further improved by incorporating the central light reflex into the classification approach in [116]. In their test images arteries were present with a clear and visible central reflex, and therefore this observation suggested such a discriminating feature should be adopted for vessel classification. A probability of belonging to the vein class was assigned to each vessel based on the average value of the red contrast (i.e. a parameter defined as the ratio between the peak of intensity in the central part of the vessel

profile and the largest value between intensities at two end-points of the profile) along the vessel [116].

In another study Saez et al. defined two types of feature vectors, namely pixel-based and profile-based [117]. Feature vectors were constructed using Red, Green, Hue and Lightness colour components of the RGB and HSL colour spaces and classification was performed using K-Means clustering on $58$ images obtained from hypertensive subject between two concentric circumferences around the OD. Quadrants were rotated in steps of $20^\circ$ to include at least one artery and one vein in each quadrant. The positive and negative likelihood ratios, which confirm the validity of their system, were $(7.2386, 4.2218)$ and $(0.2445, 0.1528)$ for arteries and veins, respectively. They also reported $87\%$ and $90.08\%$ correct classification before and after applying their proposed tracking method in [118]. Their quadrant-wise classification imposes a condition to have at least one artery and one vein per quadrant. Also, basic K-Means clustering is sensitive to the initial centres and gets stuck easily at local optimal values which contribute significantly to misclassification [119] [120]. In another approach Joshi et al. applied fuzzy C-Mean clustering to $15$ colour fundus images [121]. In order to classify vessels, the separation of vessel trees into a structurally mapped vessel network was carried out. The classification was performed by creating the feature vector from Green (of RGB) and Hue (of HSI) channels. The authors excluded centreline pixels which have similar affinity for both the clusters from the successive classification process, treating them as noisy pixels. The proposed method resulted in a classification accuracy of $88.28\%$.

2. Supervised Classification

   While supervised methods need a training set (which can require substantial volumes of manual annotations), the classification rates are generally higher than unsupervised techniques [108] [109]. Several authors have reported supervised vessel classification algorithms [6] [33] [34] [35] [51] [122] [123] [124]. Niemeijer et al. extracted a set of $24$ features from each centreline pixel from $20$ colour fundus images in the publically available DRIVE database

which were further used for training and testing [34]. Feature selection using a wrapper based method and sequential forward floating selection was employed to find the best features for differentiating between arteries and veins. The authors tested several different classifiers - Linear Discriminant Analysis (LDA), Quadratic Discriminant Analysis (QDA), Support Vector Machine (SVM) and k-Nearest Neighbour (kNN) classifier - on the training data and found that the kNN classifier provided the best overall performance (area under the ROC curve: $0.88$). The same authors used the INSPIRE-AVR data set to classify vessels in zone B with $27$ features, and the best result was achieved with LDA (area under ROC: $0.84$) [122].

Narasimha-Iyer et al. performed vessel classification using four different classifiers namely: Nearest Neighbour, $5$ Nearest Neighbour, Fisher Linear discriminant (FLD) and a SVM classifier; the latter gave the best result [35]. They computed structural and functional features for each vessel segment - vessel central reflex as the structural feature and the ratio of the vessel optical densities from images at oxygen-sensitive and oxygen-insensitive wavelengths as a functional indicator. They extracted the parameters of the intensity profile of a vessel in order to use the information from the central reflex as structural feature. In order to capture the functionality of the vessel the optical densities were obtained at two wavelengths *(570 and 600 nm)* and their ratio is formed to find the $OD_{ratio}$ (ODR). ODR that is inversely proportional to the saturation in the blood [125] is usually, low in arteries and larger in veins [35]. These structural and functional features were combined into a classifier to identify the vessel type. Their proposed algorithm achieved true positive rates of $97\%$ for the arterioles and $90\%$ for the venules when applied to a set of $251$ vessel segments obtained from $25$ dual wave-length images. They suggested that their method is independent of the location of the retina being imaged and can work on vessels from any retinal regions.

Zamperini et al. experimented with different linear and nonlinear classifiers (Linear and Quadratic Normal Bayes, Parzen Classifier, Linear and radial basis SVM) to classify a total of $656$ points ($326$ labelled as arterioles and $330$

as venules) from 42 images in zone B [123]. The system was based on finding optimal features for vessel classification and testing different supervised labelling approaches in order to assign correct labels to pixels belonging to the vascular centreline by using colour features as well as positional information. They performed a greedy backward feature selection on a set of 86 features and found the best result using a reduced set of 16 features. They used small (radius equal to half the vessel width) and large (radius equal to twice the vessel width) ROI′s to extract colour features. Colour features on large ROI′s were computed to investigate the effect of vessel contrast with respect to (w.r.t.) the retinal background. They performed classification using a leave-one-image-out procedure with different linear and non-linear supervised classifiers. The best classification accuracy of 93.1% was obtained with the Linear Bayes normal classifier.

In another study on vessel classification using supervised classification, Muramatsu et al. analysed 160 vessels from 40 DRIVE images in zone B using a LDA classifier and leave-one-out method with 6 features [124]. This resulted in 92.8% classification accuracy. Kondermann et al. investigated two methods for feature extraction (ROI and profile based) and two for classification (Neural Network (NN) and SVM). Multiclass Principal Component Analysis (PCA) was used by the authors in their experiments to reduce the dimensionality of the feature vector for subsequent use in the classifier [33]. They showed that performance of both NN and SVMs was extremely good on hand-segmented data, but the results deteriorate by about 10% on automatically segmented images. Also, after including the meta-knowledge about vessel segments between crossings , i.e. a vessel does not change its class between two crossings, they were are able to classify 95.32% of the vessel centre lines correctly by combining the ROI feature vector composition method with a NN classifier.

Mirsharif et al. used forward feature selection to find the most discriminant features for training several classifier (Kmeans, fuzzy clustering, SVM and LDA) [6]. They evaluated the performance of their proposed method on two different datasets viz. DRIVE (40 retinal images) and their own dataset (13

retinal images). Their proposed method resulted in $90.2\%$ and $88.2\%$ accuracy for DRIVE and their own datasets, respectively.

Recently, a combination of graph-based approach and vessel intensity information was proposed by Dashtbozorg et al. for vessel classification using LDA, QDA and kNN [51]. The authors used sequential forward floating selection method for feature selection. Their proposed approach resulted in an accuracy rate of $88.3\%$ for INSPIRE-AVR ($40$ images) dataset when classification was performed on all vessels pixels in entire images whereas accuracy of $87.4\%$ was obtained when classification was performed on the main vessels (vessels with calibre higher than $3$ pixels) for DRIVE images. The $89.8\%$ classification rate was obtained on VICAVR ($58$ images) database.

Table 3.1 summarises the related work in the field of artery/vein classification. Among the unsupervised approaches of Grisan et al. [70], M. Saez et al.[117] and V. S. Joshi et al. [121], classification accuracy was highest for the framework designed by M. Saez et al. i.e. $90.08\%$ [118]. They tested their method on $58$ images obtained from hypertensive subjects. Grisan et al. does not provide any information regarding the source of their tested images [70]. Whereas, V. S. Joshi et al. tested the proposed approach on $15$ diabetic subjects. It is, therefore, difficult to comment on which approach is the best as the classification accuracy is highly dependent on the images used and the classification framework. It should also be noted that the same classifier yields different classification accuracies with different set of features on the same set of images. This observation applies equally to supervised approaches of classification. However, it is sensible to compare the results obtained from the same image sets and in the same region or zone. Among the classification framework of Muramatsu et al. [124] and Mirsharif et al. [6], who tested their approaches on DRIVE images and in zone B, the classification rate was higher for the former. Whereas for the classification frameworks of M. Niemeijer et al. [34] and Dashtbozorg et al. [51], who tested their respective methods on whole vasculature visible in DRIVE images, yielded similar classification rates.

As discussed, numerous methods have been developed to identify vessel type using various colour features with different classification algorithms [33] [70] [116] [117] [121]. Using the most relevant features for vessel classification is extremely important in order to attain a high classification rate. It is not easy to achieve vessel classification by predefining the set of features for all images because the absolute colour of the blood column varies between images and across subjects [122] [123]. Moreover, image resolution and image quality are not constant and is often dependent upon the type of diagnosis being made [11]. This further contributes to misclassification with a predefined feature set.

| Author[Reference] | Method | Feature Used | Dataset/Zone/No. of Images(Im) or vessels (ves.) | Result |
|---|---|---|---|---|
| *Grisan et al. [70]* | Quadrant-wise approach, fuzzy C-Mean. | Mean of Hue and var. of red. | own/zone B/443 ves. from 35 Im. | 87.6% |
| *M. Saez et al.[117]* | Quadrants were rotated in steps of 20 degrees, K-Means | Pixel & profile based features from red, green, hue and lightness colour components. | own /zone B / 58 Im | 87% and 90.08% (before and after applying proposed tracking method [118] ) |
| *V. S. Joshi et al. [121]* | fuzzy C-Mean | Green (of RGB) and Hue (of HSI) channels. | own/-/15 diabetic subjects. | 88.28% |
| *M. Niemeijer et al. [34]* | Feature selection using a wrapper based & sequential forward floating method, Different Classifiers: LDA, QDA, SVM, kNN.) | 24 features from centreline pixel. | DRIVE/ whole Im / 20 Im | Best result: kNN ROC: 0.88 |
| *M. Niemeijer et al. [122]* | Feature selection using a wrapper based & sequential forward floating, Different Classifiers: LDA, QDA, SVM, kNN. | 27 features from centreline pixel. | INSPIRE-AVR/zone B/ 20 Im | Best result:LDA ROC: 0.84 |
| *Narasimha-Iyer et al. [35]* | Nearest Neighbor, 5 Nearest Neighbor, FLD & SVM. | Structural & functional features. | own/ -/251 ves. from 25 dual wave-length images. | Best result:SVM, True positive rates: arterioles:97%& venules:90% |
| *Zamperini et al. [123]* | Linear & Quadratic Normal Bayes, Parzen Classifier, Linear and radial basis SVM with leave-1-image-out method Feature selection: greedy backward method. | colour and positional features: 86 features from large and small ROIs. | own/zone B/ 656 points from 42 Im | 93.1% with the Linear Bayes normal classifier. |
| *Muramatsu et al. [124]* | LDA classifier & leave-1-out method. | 6 features from R,G & B | DRIVE/zone B/160 ves. | 92.8% |
| *Kondermann et al. [33]* | NN & SVM classifier with PCA | ROI & profile based features | own/within 3 OD diameters/ 4 Im. | 95.32% with NN |
| *Mirsharif et al. [6]* | Kmeans, fuzzy clustering, SVM and LDA with forward feature selection for training the classifier. | ROI and profile based features from HSL and LAB color spaces. | DRIVE, own/zone B/ 40 Im and 13 Im respt. | 90.2% and 88.2% for DRIVE and own dataset respt. |
| *Dashtbozorg et al. [51]* | Using LDA, QDA & kNN classifier, feature selection: sequential forward floating selection. | Structural information with 30 features from RGB and HSL colour space. | INSPIRE-AVR, DRIVE and VICAVR /whole image/ 40, 20 and 58 Im respt. | Best result: LDA, 88.3%, 87.4% and 89.8% for INSPIRE-AVR, DRIVE and VICAVR respt. |

Table 3.1: Summary of literature review of a|v classification

## 3.3 The Arteriolar to Venular Width Ratio

AVR is defined as CRAE / CRVE, where CRAE is the Central Retinal Artery Equivalent and CRVE is the Central Retinal Vein Equivalent. In general, AVR is known as the ratio of arteriole width to venular width. Automatic artery/vein classification enables the efficient extraction of vascular biomarkers such as arteriolar-to-venular diameter ratio (AVR) [122]. Conventionally, AVR (and other measurements of retinal vascular parameters) are acquired from zone B - an annulus $0.5$ to $1$ optic disc (OD) diameter from the OD boundary [1] [14] [50].

### 3.3.1 Parr-Hubbard

CRAE was first derived by Parr et al. which is estimated from arteriolar widths found in zone B [24]. This choice was based on data which showed that arteriolar widths appear to decrease significantly after this distance from the optic disk in patients with hypertension [2]. They proposed the arterial parent-daughter branch relationship applies only to normal vessels of young subjects in the form of a second power polynomial relationship. CRAE is given by [39] [78],

$$W_a = (0.87w_1^2 + 1.01w_2^2 - 0.22w_1w_2 - 10.76)^{1/2} \tag{3.1}$$

where $w_1$, $w_2$, and $W_a$ are the widths of the smaller branch, the larger branch, and the parent trunk in an arteriolar branching. Hubbard et al. in 1999 proposed a similar relationship for retinal venous branch points, (i.e. CRVE) [39],

$$W_v = (0.72w_1^2 + 0.91w_2^2 + 450.05)^{1/2} \tag{3.2}$$

where $w_1$, $w_2$, and $W_v$ are the widths of the smaller branch, the larger branch,

and the parent trunk in a venular branching. Parr and Hubbard derived formulas for the CRAE and CRVE, respectively, by examining a prospective group of retinal images with branching points, calculating the relationship between individual trunk vessels and their respective branch vessels and using a root mean square deviation (RMSD) model that best fit the observed data. The resultant AVR formula was used successfully in large number of epidemiology studies [126].

### 3.3.2 Knudtson

In 2003, Knudtson et al. pointed some spurious variability in the equations proposed by Parr-Hubbard formulas [127]. Firstly, in the Parr-Hubbard equation, the overall estimate of vessel calibre was contributed by a variable number of vessel diameters for each eye. Secondly, the formulae include constant terms making the result dependent upon the measurement units (e.g. microns or pixels) [17]. Knudtson et al. developed new formulas for calculating the AVR, based on the concept of a branching coefficient (BC; quotient of the area of the branch and trunk vessels) [127]:

$$BC = \frac{(w_1^2 + w_2^2)}{W^2} \tag{3.3}$$

where $w_1$, $w_2$ and $W$ are, respectively, the widths of the narrower branch, the wider branch, and the parent trunk.

Knudtson et al. estimated the BC for arterioles and venules separately using data from $44$ young normotensive adults that Hubbard et al. used to develop their venular formula. Knudtson et al. inserted their estimates of the BC into equation 3.3 and solved for *W* to yield the calibre of arterioles and venules,

$$W_a = 0.88(w_1^2 + w_2^2)^{1/2} \tag{3.4}$$

$$W_v = 0.95(w_1^2 + w_2^2)^{1/2} \tag{3.5}$$

where $W_a$ and $W_v$ are the measured arteriole and venule vessel widths, respectively. Also, $w_1$ and $w_2$ are the widths of the narrow and wider branches, respectively. A mean BC of $1.28$ was found for arterioles in a young, normotensive population and this compares well with a theoretical BC of $1.26$ derived from Murray's law [127] [128]. The revised formulas were shown to be superior to the prior Parr-Hubbard formulas. Note, the theoretical BC $(1.26)$ only applies for symmetrical dichotomous vessel branching (where width of branch $1$ = width of branch $2$).

The formulas proposed by Knudtson et al. showed a high correlation with the Parr-Hubbard method (Pearson correlation coefficients ranging from $0.94$ to $0.98$) [127]. The revised formula were also not affected by the number of measured vessels. Thus it offered an added advantage of being more robust against variability in the number of vessels observed and it was easier to implement [127]. This is because Knudtson et al. chose to limit the calculation to the six widest arterioles and six widest venules. Although a fewer number of measurements can be used in case not enough vessels are visible or present in an image. Knudtson recursively paired the vessels (i.e. largest with smallest, next largest with next smallest and so on) in order to calculate CRAE and CRVE [127]. Algorithm 1 shows implementation procedure of Knudtson et al. iterative process for matching up vessels in order to calculate CRAE and CRVE [122].

**Algorithm 1:** AVR using the Knudtson method

**Data**: Create vector A and vector V containing the widths of the found arteries and veins of length |A| and |V| in zone B

**Result**: To calculate AVR: Sort A and V in decreasing order and set the length of both vectors to N=min(|A|, |V |, 6).

Initialisation;
**while** $|A| > 1$ **do**
    Select and remove the first element F and last element L from vector A.
    Calculate $(0.88 * (F^2 + L^2)^{1/2})$ and store in another vector Ca;
    **if** $|A| \leq 1$ **then**
        A = A $\cup$ Ca;
        Sort A in decreasing order;
    **end**
**end**
**while** $|V| > 1$ **do**
    Select and remove the first element F and last element L from vector V.
    Calculate $(0.95 * (F^2 + L^2)^{1/2})$ and store in another vector Cv;
    **if** $|V| \leq 1$ **then**
        V = V $\cup$ Cv;
        Sort V in decreasing order;
    **end**
**end**
$AVR = \frac{A}{V}$

### 3.3.3 Goatman

In cases where the number of vessels is not even this leads to at least one vessel being paired fewer times than the other vessels, which will introduce a small bias towards the lesser-paired measurements [129]. Thus instead of recursively applying equations 3.4

and 3.5 to pairs of vessels, Goatman et al. proposed an unbiased analytic estimation of the central retinal artery (CRA) equivalent width, $W_{CRA}$, from *N* vessel measurements [129],

$$W_{CRA} = 0.88^{log_2 N} \sqrt{\sum_{i=1}^{N} (W_a^2(i))} \tag{3.6}$$

where $W_a(i)$ is the $i_{th}$ arteriole width measurement. Similarly, central retinal vein (CRV) equivalent width $W_{CRV}$ can be derived. Combining $W_{CRA}$ with $W_{CRV}$ gives the arteriole/venule (A/V) ratio

$$A/V = (\frac{0.881}{0.95})^{log_2 N} \sqrt{\frac{\sum_{i=1}^{N} (W_a^2(i))}{\sum_{i=1}^{N} (W_v^2(i))}} \tag{3.7}$$

where $W_v(i)$ is the $i_{th}$ venule width measurement. Equation 3.7 is a weighted ratio of the root mean square arteriole diameter and the root mean square venule diameter.

The Goatman approach, which is not iterative process is detailed in Algorithm 2.

**Algorithm 2:** AVR using the Goatman method

**Data**: Create vector Ag and vector Vg containing the widths of the found arteries and veins of length |Ag| and |Vg| in zone B

**Result**: To calculate AVR: Sort Ag and Vg in decreasing order and set the length of both vectors to N=min(|Ag|, |Vg|, 6).

1 Initialise and calculate the constant terms: Ca=0.88, Cv=0.95, factor=$log_2(N)$

2 Calculate: $W_{CRA}$= $Ca^{factor}$ $\sqrt{\sum_{i=1}^{N} (Ag^2(i))}$ and $W_{CRV}$= $Cv^{factor}$ $\sqrt{\sum_{i=1}^{N} (Vg^2(i))}$

3 $AVR = \frac{W_{CRA}}{W_{CRV}}$

### 3.3.4 Patton

Patton et al. also describe a revised formula for the estimation of retinal trunk arteriole widths from their respective arteriolar branch widths that further improved the summarising of retinal arteriolar diameters [126]. The relationship between the BC and the asymmetry index (AI) of the vessel branches was explored and the result was used to formulate a new BC. In order to determine whether variation in the ratio between the widths of the two vessel branches can also explain some of the variation in the BC, Patton et al. performed a study to ascertain the relationship between the degree of asymmetry at retinal vascular junctions (asymmetry index [AI] = branch 1/branch 2) and the BC. A revised formula was devised for the arteriolar BC using a linear regression model that incorporates its relationship to the AI,

$$Wp_{CRA} = \sqrt{\frac{1}{BCA}(w_1^2 + w_2^2)} \tag{3.8}$$

$$Wp_{CRV} = \sqrt{\frac{1}{BCV}(w_1^2 + w_2^2)} \tag{3.9}$$

where $w_1$ and $w_2$ are the widths of the smaller branch and the larger branch. $BCA = 0.78 + 0.63 * AI$, where $AI = w1/w2$ and $BCV = 1.22$. Patton et al. also used an iterative procedure for matching up vessels to calculate CRAE and CRVE, which is described in Algorithm 3.

**Algorithm 3:** AVR using the Patton method

**Data**: Create vector Ap and vector Vp containing the widths of the found arteries and veins of length |Ap| and |Vp| in zone B

**Result**: To calculate AVR: Sort Ap and Vp in decreasing order and set the length of both vectors to N=min(|Ap|, |Vp|, 6).

**while** |*Ap*| > 1 **do**
    Select and remove the first element F and last element L from vector Ap.
    Initialise and calculate the constant terms: AI=$L/F$, BCA=$0.78$ + $0.63$ * AI, fa=$\sqrt{(1/BCA)}$;
    Calculate fa* $\sqrt{(F^2 + L^2)}$ and store in another vector Ca;
    **if** |*Ap*| $\leq 1$ **then**
        Ap = Ap $\cup$ Ca;
        Sort Ap in decreasing order;
    **end**
**end**
**while** |*Vp*| > 1 **do**
    Select and remove the first element F and last element L from vector Vp.
    Initialise and calculate the constant terms: BCV=$1.22$, fv=$\sqrt{(1/BCV)}$;
    Calculate fv* $\sqrt{(F^2 + L^2)}$ and store in another vector Cv;
    **if** |*Vp*| $\leq 1$ **then**
        Vp = Vp $\cup$ Cv;
        Sort Vp in decreasing order;
    **end**
**end**
$AVR = \frac{Ap}{Vp}$;

A study by Hemminski et al. compared different AVR calculation methods on both left and right eye [130]. They used following formulae for comparison :

1. Central retinal arteriolar equivalent (CRAE)/ Central retinal venular equivalent

(CRVE);

2. Mean arteriole width/ Mean venule width;
3. Sum of widths of arterioles/ Sum of widths of venules;
4. Sum of squares of widths of arterioles/ Sum of squares of widths of venule

They investigated that the AVR calculated using the sum of squares of widths of arterioles and venules correlated best with CRAE/CRVE ($R^2$ $0.92$) and AVR calculated using the mean arteriole and venule widths or the sum of widths of arterioles and venules resulted in clearly lower associations ( $R^2$ $0.38 - 0.40$ and $R^2$ $0.41 - 0.48$, respectively). According to their study AVR calculated by CRAE/CRVE has the best repeatability and there is no significant difference between CRAE/CRVE measurements taken from left eye and right eye of eighty-seven men [40] [130]. High repeatability of AVR formula (CRAE/CRVE) shows the suitability of the formula for the evaluation of retinal vascular changes in systemic diseases. They also showed that it is sufficient to examine only one eye if fundus vascular alterations associated with systemic hypertension needs to be evaluated [130]. In another paper, Wong et al. investigated that there was substantial correlation between right and left eyes for retinal arteriolar diameters (Pearson correlation coefficient, $\rho = 0.71$) and venular diameters ( $\rho = 0.74$) and moderate for the AVR ($\rho = 0.49$) [25]. They also found that the inverse association of higher blood pressure and smaller retinal arteriolar diameters was similar using data from either one eye or two eyes; arteriolar diameters decreased by $4.1\mu m$ (right eyes), $4.0\mu m$ (left eyes), and $4.0\mu m$ (mean of both eyes) with each 10-mmHg increase in mean arterial blood pressure. Leung et al. investigated that retinal arteriolar and venular diameters narrow with increasing age, and these parameters are inversely related to blood pressure (BP), independent of age, gender, and smoking [50].

Recent studies shows that retinal microvascular abnormalities are associated with stroke [15] [46] for example retinal vessel widths predict future risk of stroke [14] [81] [131] and may be associated with a previous cerebral infarction [132] [133]. Double et al. showed that retinal venules are wider and arteriovenous ratios are smaller in patients with lacunar strokes compared with those in patients with cortical strokes [93].

### 3.3.5 Further Remarks

Measurements from outside zone B might also lead to candidate biomarkers of disease. For instance, Cheung et al. studied the association of blood pressure with retinal vascular calibre measured over the standard zone and an extended zone of the fundus images [134]. They found that reliability of retinal vascular calibre measurement was high for the extended zone. Moreover, cardiovascular risk factors explained to a greater degree the variation in retinal vascular calibre in the extended zone. Therefore, application of automatic vessel classification outside of zone B is warranted to fuel further development of AVR.

## 3.4 Fractal Analysis

Fractal dimension (FD) is a geometrical measure that quantifies the degree of branching complexity of a structure such as the retinal vasculature and how it fills space [44]. A high FD represents a complex structure with lots of branching and vessels, i.e. a denser vascular network, while a lower FD signifies a sparser or less optimal vascular network [44]. As the pattern of blood vessels in the human retina displays fractal properties [27] [28] [135] [136] , therefore measuring FD of the retinal vasculature through fractal analysis may aid early detection of vascular changes indicative of retinopathy and systemic diseases.

### 3.4.1 Monofractal

As many pathological conditions affect the retinal vasculature, measuring the FD can be used as a property to distinguish images [28] [135] [136]. Recent work reported that an increase in FD is correlated with the diabetic retinopathy signs in type 1 diabetes [29] and a decrease in FD with age and blood pressure [137]. These studies were based on the box-counting method (BCM) of fractal analysis to estimate FD [138]

[139] [140]. Avakian et al. performed quantitative region-based fractal analysis using the BCM to evaluate vascular patterns in images acquired from normal people and those with non-proliferative diabetic retinopathy (NPDR) [135]. They demonstrated that the vessel density in the normal macular region appeared greater than the vessel density in the NPDR macular region and in the normal paramacular region. They located $5$ paramacular sub-regions or zones in superior, superotemporal, temporal, inferotemporal and inferior to the macula. They suggested that the alterations in retinal vasculature during early-stage diabetic retinopathy (i.e., by NPDR) measured by FD may have resulted from several disease mechanisms and/or imaging artefacts. They also suggested that the decreased vessel density in the NPDR macula may have resulted from non-perfusion, drop-out and/or narrowing of vessels. Measurements of decreased vessel density in the NPDR macula could have resulted from opacity of the cornea or lens, which might be expected to obscure vessels in NPDR [135]. However, they recommended the requirement of more complete studies to confirm the measurements of macular change in NPDR.

Various studies using BCM have shown that the appearance of the vasculature in retinal images has a strong relation with high blood pressure and cardiovascular disease [13] [30] [137] [141]. Kurniawan et al. showed that the higher blood pressure in children is associated with smaller box-counting FD [13]. However, Kruk et al. presented that hypertensive subjects have higher mean FD calculated from BCM as compared to normal subject [141]. Liew et al. demonstrated that box-counting FD was inversely correlated with age and systolic blood pressure [137]. They showed that after adjustment for age and sex, mean box-counting FD was significantly lower in participants with than without hypertension. Liew et al. investigated that BCM is a novel means of quantifying microvascular branching that independently predicted $14$-year coronary heart disease (CHD) mortality [30]. These suggested that microvascular branching may play a role in development of clinical cardiovascular disease.

### 3.4.2 Multifractal

Stosic et al. and Ward et al. demonstrated that the retinal vasculature exhibits multifractal behaviour [28] [142] . That is, the vascular structure can be characterised by a hierarchy of exponents rather than a single fractal dimension. A number of retinal images from the STARE database [143] corresponding to ten 'normal' and ten 'pathological' retinas were analysed using multifractal analysis (MFA) and it was shown that the pathological images have lower dimensions as well as a shifted range in the spectrum of exponents in comparison to the normal cases.

Macgillivray et al. showed that a hypertensive sub-group ($n$=20) exhibited lower FD or a sparser vascular network than a non-hypertensive sub-group ($n$=20), using both monofractal analysis (i.e. BCM) and MFA, where $n$ is the number of test images [92]. They determined that monofractal analysis may be more sensitive to skeletons rather than the segmented images, whereas the opposite of this was the case for MFA. Analysing the skeletons showed that only 13 from the non-hypertensive sub-group and 14 from the hypertensive sub-group displayed multifractal properties. Though the number of images is too low to draw many certainties. Furthermore, the MFA procedure performed in [28] [92] and [142] appears very time consuming - the authors did not report any specific details; this observation was based on an implementation of the algorithm (i.e. 40 minutes per image).

Doubal et al. the authors investigated the associations between fractal properties of the retinal vessels in patients with clinical and magnetic resonance imaging (MRI) features of lacunar stroke and white matter disease [75] to test the hypothesis that patients with lacunar stroke (as a distinct marker of cerebral small vessel disease) will have altered fractal properties of their retinal vessels compared with a cortical stroke control group (as a distinct marker of large artery atherothromboembolic disease) [144] [145]. A sparser network (with both BCM and MFA) was found to be associated with lacunar stroke and increasing age after correcting for other vascular risk factors and white matter hyperintensities (WMH) [75]. This was demonstrated despite the control

group being on average $4$ years older than the lacunar stroke patients, which would usually tend to mask any associations.

In another study Aliahmad et al. investigated to find the association of FD with future episode of stroke event using the Blue Mountain Eye Study (BMES) database [146]. They measure the FD using Higuchi fractal (HF) method, spectrum fractal method [147] [148] and BCM in three concentric zones around OD. They showed that there was a significant association between FD calculated in zone B using Higuchi fractal (HF) method with future episode of stroke while this difference was not significant when other methods were employed.

### 3.4.3 Fourier Fractal Dimension

In recent years, the Fourier fractal dimension (FFD) has been used for retinal image analysis [149] [136] due to certain advantages associated with FFD. Both BCM and MFA needs the segmented image - either manual or computerised, to calculate the FD but measuring FFD eliminates the need for image segmentation [150] and is relatively insensitive to noise [150] [151]. Changes in angle between the camera and the optical axis cause variations in the brightness of an image which significantly impacts when the image is binarised to produce a vessel map. Some vessels that are observed in the segmented image from one angle may be missed from another angle. Azemin et al. showed the significant correlation between the known and computed FFD calculated from noisy images confirmed the robustness of FFD against noise [152]. It was also shown that FFD is less sensitive to the angle between the camera and the optical axis of the eye compared with the box-counting method as FFD does not require segmentation of the image. Hence, FFD could in some ways be considered to be more reliable. In one of the study a significant decrease in the FFD with ageing was reported on analysing $748$ retinal images taken from persons aged $49 - 89$ years [136].

## 3.5 Summary

This chapter introduced some key concepts in computational analysis of fundus photography, namely classification of vessels into arteries and veins, the measurement of AVR and fractal analysis. Important work in the field of vessel classification, using both supervised and unsupervised approaches, was presented and discussed. Such analysis of vessel class forms the preceding step to the measurement of AVR. Four approaches for calculating AVR were summarised and discussed in this chapter. Finally, fractal analysis as a means of quantifying the vascular pattern in fundus camera images and detecting changes associated with disease and systemic conditions was also presented, with key studies in this field were also highlighted.

# Chapter 4

# Artery-Vein Classification

## 4.1 Introduction

In this chapter, automatic retinal vessel classification into arterioles and venules using supervised and unsupervised approaches and colour features is presented. Mathematical background for the various techniques is detailed in section 4.2. Section 4.3 discusses the materials and methodology for developing the vessel classification algorithms. During the computerised process of categorisation some of the vessels can remain unclassified, so section 4.4 introduces an approach to reduce such instances. Classifying retinal vessels into arterioles and venules is a precursor to measuring AVR. Section 4.5 explains the implementation and testing of AVR measurements. Finally, conclusions are summarised in section 4.6.

## 4.2 Mathematical Background

Broadly speaking, computerised vessel classification splits into two categories: (i) unsupervised methods, which do not need any training (i.e. access to previously categorised or labelled data), and (ii) supervised approaches, which do need training

data in order to assign labels to unseen data. When high dimensional data are available (for instance, a large number of colour-based features with which classifier attempt retinal vessel classification), it is often advisable to reduce dimensionality before classification in order to discard uninformative features and to overcome the challenges of 'curse of dimensionality' (for a given sample size, there is a maximum number of features above which the classifier performance will degrade) in order to improve performance [106] [153]. This section introduces the mathematical background for techniques employed in this thesis which includes unsupervised and supervised approaches as well as methods for reducing dimensionality.

### 4.2.1 Unsupervised Vessel Classification

1. **Gaussian Mixture Model with Expectation-Maximisation (GMM-EM)**

   In practice, each cluster in the data is assumed to be mathematically represented by a parametric distribution like a Gaussian, and the entire dataset is therefore modelled by a mixture of these distributions [154]. Considering data as a mixture of Gaussian distributions is a widely used means to cluster the data [154]. A Gaussian Mixture Model (GMM) is a parametric probability density function represented as a weighted sum of Gaussian component densities, and each Gaussian component has its own mean and covariance [155]. A GMM is a collection of $K$ Gaussian distributions where each distribution is called a mode of the GMM and represents a cluster of data points. A GMM consists of the means, covariances, and a probabilistic assignment of every data point to the Gaussians [120].

   The commonly used approach for determining the GMM parameters (i.e. mean, covariance, mixture coefficient) from a given dataset is to use the maximum likelihood estimation. The Expectation-Maximisation (EM) algorithm is a general, iterative technique for computing the maximum likelihood estimate of the parameters of an underlying distribution from data which is incomplete or has missing values [120] [156].

The EM algorithm is a local optimisation method, and hence it is sensitive to the initialisation of the model. Therefore, the simplest way to initiate parameters is to use a *K-means* approach [120]. Thus, before explaining GMM-EM, it is worth introducing *K-means*. *K-means* clustering results in a linear separation of clusters and is not suitable for separation of non-linearly separable data, therefore its application is limited in practice [157]. In this approach to clustering, the first *K* number of 'mean' $\mu_k$ for each of the classes is initialised. For example, for binary clustering *K*=2 (i.e. 2 classes), mean $\mu_1$ and $\mu_2$ are initialised. The algorithm splits into two phases [119] [120] [158],

I. Assign each point of the data to the closest mean $\mu_k$

II. Update means of the new cluster.

After the updating phase (i.e. phase II) again assign each data point to the closest mean (i.e. repeat phase I), and this procedure continues until means do not change any more - i.e. the two phases of re-assigning data points to clusters and re-computing the cluster means are repeated in turn until there is no further change in the assignments (or until some maximum number of iterations is exceeded). In *K-means*, a point must belong to one of the classes and so this approach does not explain points that lie in between groups.

GMM is a simple linear superposition of Gaussian components, which provides a richer class of density models than the single Gaussian [120]. Mathematically, a Gaussian can be defined as [120],

$$p(X) = \mathcal{N}(X|\mu, \Sigma)) \tag{4.1}$$

where $\mu$ is the mean, $\Sigma$ is the variance and $\mathcal{N}$ signifies the normally distributed Gaussian. Similarly the mixture of Gaussian is defined as [120],

$$p(X) = \sum_{k=1}^{K} \pi_k \mathcal{N}(X|\mu_k, \Sigma_k). \tag{4.2}$$

where $\pi_k$ is the mixture coefficient of $k^{th}$ Gaussian. In *K-means* clustering one

can have only a 'mean' parameter to fit but in GMM one can have mean $\mu_k$ , covariance $\Sigma_k$ and mixture coefficient $\pi_k$ to fit. Given a GMM, the main aim is to maximise the likelihood function w.r.t. the parameters ($\mu_k$, $\Sigma_k$ and $\pi_k$ ) [120]. Finding maximum likelihood solutions for models with latent variables is called the expectation-maximisation algorithm, or EM algorithm. EM for Gaussian mixtures algorithm [120] is explained as,

I. **Initialise Gaussian parameters**: Initialise $\mu_k$ , $\Sigma_k$ and $\pi_k$ for each Gaussian *k*.

II. **E Step**: Assign each point $X_n$ an assignment score $\gamma(Z_{nk})$ for each Gaussian *k*,

$$\gamma(Z_{nk}) = \frac{\pi_k \mathcal{N}(x_n|\mu_k, \Sigma_k)}{\sum_{j=1}^{K} \pi_j \mathcal{N}(x_n|\mu_j, \Sigma_j)}. \tag{4.3}$$

III. **M Step**: Given scores, adjust $\mu_k$ , $\Sigma_k$ and $\pi_k$ for each cluster *k* i.e. for each Gaussian *k*, update parameters using new $\gamma(Z_{nk})$. Mean of Gaussian *k* is given by,

$$\mu_k^{new} = \frac{1}{N_k} \sum_{n=1}^{N} \gamma(Z_{nk}) x_n \tag{4.4}$$

where *N* is total number of data points and $N_k$ is defined as the effective number of points assigned to cluster *k* and given by,

$$N_k = \sum_{n=1}^{N} \gamma(Z_{nk}). \tag{4.5}$$

Find the means that fits the assignment score best. Covariance matrix of Gaussian *k* is given by,

$$\Sigma_k^{new} = \frac{1}{N_k} \sum_{n=1}^{N} \gamma(Z_{nk})(x_n - \mu_k^{new})(x_n - \mu_k^{new})^T. \tag{4.6}$$

Mixing coefficient for Gaussian *k* is given by,

$$\pi_k^{new} = \frac{N_k}{N}. \tag{4.7}$$

IV. **Evaluate log Likelihood**: Calculate log likelihood,

$$ln\ p(X|\mu, \Sigma, \pi) = \sum_{n=1}^{N} ln \sum_{k=1}^{K} \pi_k N(x_n|\mu_k, \Sigma_k) \tag{4.8}$$

and check for convergence of either the parameters or the log likelihood. If likelihood or parameters converge then stop. Else go to step II. (E step)

In the present framework, the uniform distribution to the mixture is added to pick up background noise or data points which were not associated to either an arteriolar or a venular cluster. The classifier was run for 10 different initial cluster centres and the parameters corresponding to the best fit (maximum likelihood) were chosen to compute Gaussian mixtures.

2. **Squared-Loss Mutual Information Clustering (SMIC)**

SMIC is an unsupervised method in which the mutual information between feature vectors and cluster assignments is maximised. It involves only continuous optimisation of model parameters and is therefore easier to solve as compared to discrete optimisation of cluster assignments. Also, this method gives a clustering solution analytically in a computationally efficient way via kernel eigenvalue decomposition [157].

In [157] the authors proposed an approach to information-maximisation clustering based on a squared-loss variant of mutual information. Suppose *d*-dimensional independent identically distributed (i.i.d.) feature vectors of size *n* drawn independently from a distribution with density $p^*(x)$,

$$\{x_i|x_i \in \mathcal{R}^d\}_{i=1}^{n}. \tag{4.9}$$

The main aim of the method is to give cluster assignments $y_i$ to feature vectors $\{x_i\}_{i=1}^{n}$, such that,

$$\{y_i|y_i \in \{1, ..., c\}\}_{i=1}^{n} \tag{4.10}$$

where *c* denotes the number of classes and it was assumed that *c* is known. The information-maximisation approach explained in [159] [160] was used to solve a

clustering (i.e. unsupervised classification) problem by the authors of [157]. To do this the class-posterior probability $p^*(y|x)$, was learned so that 'information' between feature vector *x* and class label *y* was maximised.

In order to solve the clustering problem, information-maximisation approach was used which involves continuous optimisation w.r.t the parameter $\alpha$ included in a class-posterior model $p^*(y|x;\alpha)$. The continuous optimisation of $\alpha$ is considerably easier to solve than discrete optimisation of $\{y_i\}_{i=1}^n$.

Squared-loss mutual information (SMI) is adopted as an information measure in which SMI between feature vector *x* and class label *y* is defined by,

$$SMI = \frac{1}{2}\int \sum_{y=1}^{c} p^*(x)p^*(y)(\frac{p^*(x,y)}{p^*(x)p^*(y)} - 1)^2 dx \tag{4.11}$$

where $p^*(x,y)$ denotes the joint density of *x* and *y*, and $p^*(y)$ is the marginal probability of *y*. SMI is the Pearson divergence [161] from $p^*(x,y)$ to $p^*(x)p^*(y)$

### 4.2.2 Supervised Vessel Classification

In supervised classification, the classifier assigns labels to new unseen data with the help of training data (represented by vectors of features and pre-determined labels). In this thesis, a supervised LS-SVM classifier was used to group retinal vessels into arteriole and venule classes. The mathematical background is as follows.

1. **Least Squares Support Vector Machines (LS-SVM)**

   Support Vector Machine (SVM) is a class of supervised learning algorithms first introduced by Vapnik [162]. It proved to be an effective technique for many classification problems [162] [163] [164] [165]. SVM constructs an optimal separating hyperplane between the positive and negative classes with the maximal margin [166] for binary-class classifications. SVM can be formulated as a quadratic programming problem involving inequality constraints. The Least Squares formulation of SVM, called LS-SVM was recently proposed [167] [168]

and is close to Vapnik's SVM formulation [162]. LS-SVM is least squares version of SVM. Unlike SVM, LS-SVM solves a linear system and involves the equality constraints only. Therefore, the solution is obtained by solving a system of linear equations. LS-SVM preserves support vector machine methodology [162], but simplifies via least squares and equality constraints [168].

The goal of the binary-class classification in SVM or LS-SVM is to learn a model that assigns the correct label to an unseen test sample. Let, there is a set of *n* training samples, denoted by $\{(x_i, y_i)\}_{i=1}^{n}$, where $x_i \in \mathcal{R}^d$ is drawn from a domain $\mathcal{X}$ and each of the label $y_i$ is an integer from $\mathcal{Y} = \{-1, 1\}$. In other words, SVM or LS-SVM learns a function $f : \mathcal{X} \to \mathcal{Y}$ which maps each instance *x* to an element *y* of $\mathcal{Y}$ [166].

Let *S* be the covariance matrix defined by,

$$S = \frac{1}{n}(X - ce^T)(X - ce^T)^T \tag{4.12}$$

where $X = [x_1, x_2, ..., x_n]$ is the data matrix, *c* is the centroid of *X* and *e* is the vector of all ones. The main aim is to define the margin of a linear classifier as the width that the boundary could be increased by before hitting a data point. If the data is separable, the hyperplane of hard margin SVM is defined by [166],

$$f(x) = (x, w) + b = 0, \tag{4.13}$$

which separates the positive and negative classes [163] (see Figure 4.1), where *w* is the normal to the hyperplane, $(x, w) = x^T w$ is the inner product between *x* and *w*, and $|b|/||w||_2$ is the perpendicular distance from the hyperplane to the origin. The hard margin SVM classifier maximise the margin around the separating hyperplane for the linearly separable data. The optimal hyperplane is computed by minimising $||w||_2$ subject to the constraint,

$$y_i((x_i, w) + b) \geq 1, \tag{4.14}$$

for all *i*. See Figure 4.1, data points closest to the hyperplane are called support vectors where margin $\rho$ of the separator is the width of separation between support vectors of classes. A test point $x$ is assigned to the positive class, if $(w, x) + b > 0$, and to the negative class otherwise (see Figure 4.1).

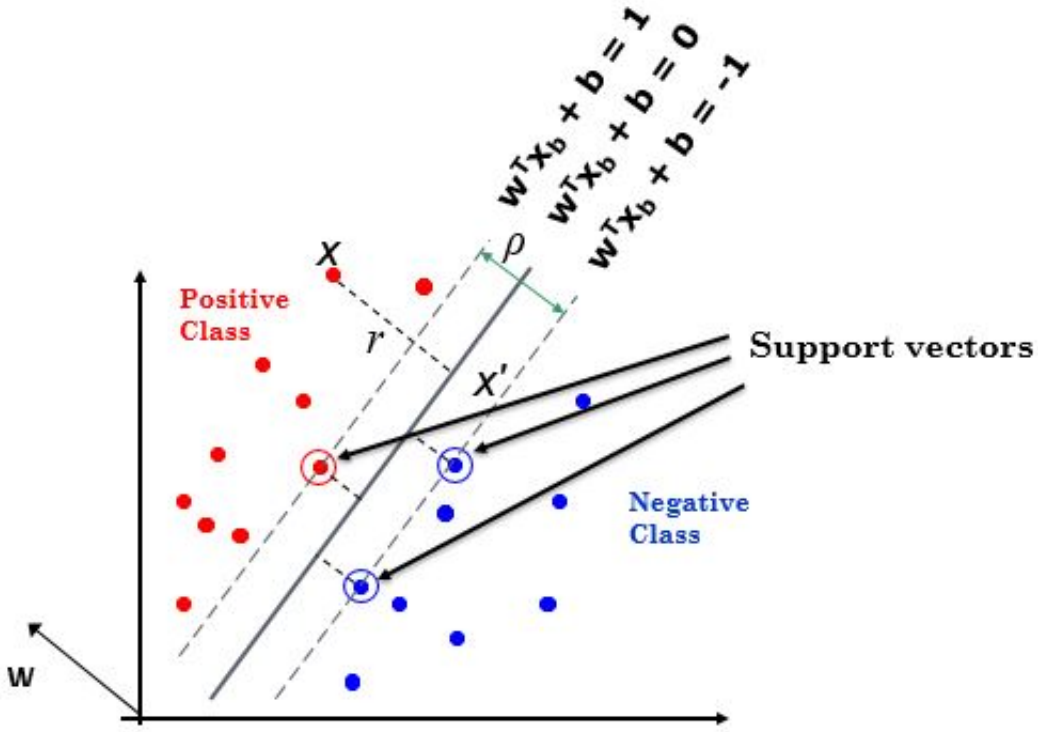


Figure 4.1: Example of defining a unique separating hyperplane illustrated in a two dimensional input space. The margin is the distance between the dashed lines which separates positive (maked in red) and negative (marked in blue) classes. (Image adapted from source: [169])

The above formulation can be extended for a soft margin SVM i.e. dealing non-separable data by introducing the slack variables and a tuning parameter *C* > 0 which is commonly estimated through cross-validation [163].

Least Squares SVM (LS-SVM) applies the linear model [168],

$$f(x) = (x, w) + b \tag{4.15}$$

where $w \in \mathcal{R}^d$ is the weight vector and *b* is the bias of the linear model. *w* and

*b* are estimated by minimising the following objective function,

$$L(w,b) = \sum_{i=1}^{n} ||f(x_i) - y_i||_2^2 + C||w||_2^2, \tag{4.16}$$

where $y$ is the vector of class labels, and C > 0 is the regularisation parameter. The parameters $w$ and $b$ can be estimated by minimisation of $L(w,b)$ and this gives,

$$w = \frac{2n_1n_2}{n^2}(S + \frac{C}{n}I_d)^{-1}(c_1 - c_2), \tag{4.17}$$

$$b = \frac{n_1 - n_2}{n} - c^T w, \tag{4.18}$$

where $c$ is the global centroid of the data, $n_1$ and $n_2$ denote the number of samples from the positive and negative classes, respectively, and $c_1$ and $c_2$ are the centroids of the positive and negative classes, respectively. If no regularisation is applied, i.e., $C = 0$, the optimal solution leads to,

$$w = \frac{2n_1n_2}{n^2}S^+(c1 - c2) \tag{4.19}$$

where $S^+$ denotes the pseudo-inverse of *S* [170]. Similar to SVM, LS-SVM also assigned a test point *x* to the positive class, if $f(x) = (w,x) + b > 0$, and to the negative class otherwise [168].

### 4.2.3 Dimensionality Reduction

Dimensionality reduction is a popular concept in classification for removing irrelevant or redundant features, thus reducing computational time in subsequent processing [171] [172] [173]. Dimensionality reduction aims at representing high dimensional data in lower dimensional spaces [174]. Techniques can be categorised into *feature extraction* and *feature selection*. Feature extraction methods transform the original data space into a new, lower dimensional space, keeping as much information from the

original data as possible [153]. In other words, feature extraction is transformative, i.e. a transformation is applied to the data to project it into a new space with lower dimension. Feature selection methods, instead, reduce the number of features contained in a feature space by removing irrelevant or redundant ones [175] [176] [177], i.e. no transformation is applied. The feature selection approach aims to select a small subset of features from the group of features that have strong discriminatory power between classes.

In order to reduce the computational cost in large datasets with high dimensional feature sets while at the same time maximising classification accuracy, dimensionality reduction techniques can play an important role [175]. Thus with this aim, two feature extraction methods - Principal Component Analysis [107] [178] [179] and Orthogonal Locality Preserving Projections, [180] - and two feature selection methods - Maximal Information Compression Index [181] and Laplacian Score [182] - were considered for retinal vessel classification. An overview of each is now presented.

1. **Principal Component Analysis (PCA)**

   Conventional PCA is one of the most commonly used feature extraction techniques and is based on extracting the axes on which data shows the highest variability [178]. PCA finds a linear projection of high dimensional data into a lower dimensional subspace such that variance retained is maximised and the least square reconstruction error is minimised [107] [179]. PCA steps, using covariance to reduce dimensionality, can be summarised as follows,

   I. Centre or standardise the data by subtracting the sample mean from each observation.

   II. Calculate the covariance matrix.

   III. Calculate the eigenvectors and eigenvalues of the covariance matrix.

   IV. Select the $m$ eigenvectors that correspond to the $m$ maximum eigenvalues. For the analysis presented in this thesis, the three highest eigenvectors were selected to reconstruct a new feature set as this was sufficient to explain $97\%$ (or more) of the total variance describe by the whole feature set.

2. **Orthogonal Locality Preserving Projections (OLPP)**

In the dimensionality reduction problem, the dimension of the features *(F)* is often much larger than the number of features *(NF)*. Thus, the *(F * F)* matrix $XDX^T$ is singular. To make $XDX^T$ nonsingular, the feature set *X* must be preprocessed by PCA. PCA projects the features into a subspace by removing the eigenvectors corresponding to low eigenvalue and the matrix $XDX^T$ becomes non-singular. The transformation matrix of PCA is denoted by $W_{PCA}$. The algorithmic procedure of OLPP is as follows [180] [183] [184],

I. **PCA Projection**: First the feature set $x_i$ is projected into the PCA subspace by throwing away the components corresponding to zero eigenvalue. Thus the extracted features are statistically uncorrelated. The transformation matrix of PCA is denoted by $W_{PCA}$.

II. **Constructing the Adjacency Graph**: OLPP can construct a *K* nearest neighbour graph with good stability in an unsupervised or supervised mode. Let *G* be a *K* nearest neighbour graph with *n* nodes. The *i*-th node corresponds to the feature $x_i$. If $x_i$ and $x_j$ are close, i.e. $x_i$ is among *p* nearest neighbours of $x_j$ or $x_j$ is among *p* nearest neighbours of $x_i$ then an edge is put between nodes *i* and *j*. In unsupervised mode, edges are located between one sample and its *K* nearest neighbours, where *K* is a small integer. Whereas for the supervised model, edges are located between one sample and its *K* nearest neighbours from the same class. Euclidean distance was chosen in order to measure the closeness between two arbitrary data nodes in a *K* nearest neighbour graph. After constructing the Euclidean distance matrix for all nodes, the *K* closest neighbours of one node can be obtained by analysing the distance matrix in unsupervised mode but for the supervised model, the class label should be considered for finding *K* nearest neighbours from the same class. The constructed nearest neighbours graph is an approximation of the local manifold structure.

III. **Choosing the Weights**: If the nodes *i* and *j* are connected, i.e. the nodes *i*

and *j* are at the same edge and so,

$$W_{ij} = e^{-\frac{||x_i - x_j||^2}{2t}} \tag{4.20}$$

where *t* is a constant. Otherwise, $W_{ij}$ = 0. The weight matrix *W* of graph *G* represents the local structure of the feature manifold structure by preserving local structure.

IV. **Computing the Orthogonal Basis Functions**: Define *D* as a diagonal matrix whose entries are column (or row, *W* is symmetric) sum of *W*, $D_{ii} = \sum_j W_{ij}$. Also define $L = D - W$, which is called Laplacian matrix in spectral graph theory [180]. Let $\{\mathbf{a_1}, \mathbf{a_2}, ..., \mathbf{a_k}\}$ be the orthogonal locality preserving projections, and define,

$$A^{(k-1)} = [\mathbf{a_1}, \mathbf{a_2}, ..., \mathbf{a_{(k-1)}}] \tag{4.21}$$

$$B^{(k-1)} = [A^{(k-1)}]^T.(XDX^T)^{-1}.A^{(k-1)} \tag{4.22}$$

The orthogonal locality preserving vectors $\{ \mathbf{a_1}, \mathbf{a_2}, ..., \mathbf{a_k} \}$ can be computed iteratively as follows:

(a) Compute $\mathbf{a_1}$ as the eigenvector of $(XDX^T)^{-1}XLX^T$ associated with the smallest eigenvalue.

(b) Compute $\mathbf{a_k}$ as the eigenvector of

$$\begin{aligned} M^{(k)} = \{I - (XDX^T)^{-1}.A^{(k-1)}[B^{(k-1)}]^{-1}[A^{(k-1)}]^T \\ .(XDX^T)^{-1}.(XLX^T)\} \end{aligned} \tag{4.23}$$

associated with the smallest eigenvalue of $M^{(k)}$.

V. **OLPP Embedding**: Let $W_{OLPI}$ = [$a_1$, $a_2$, . . . , $a_l$], the embedding is as follows,

$$\mathbf{x} \rightarrow \mathbf{y} = W^T\mathbf{x} \tag{4.24}$$

$$W = W_{PCA} W_{OLPI} \tag{4.25}$$

where **y** is a *l*-dimensional representation of the feature **x**. **W** is the transformation matrix.

OLPP has neighbourhood preserving characteristic, it can better capture the intrinsic manifold structure to a larger extent. The locality preserving ability is directly related to the discriminating ability. In contrast, the conventional algorithms such as LDA only model the features in Euclidean space and cannot detect the intrinsic low-dimensionality features.

3. **Maximal Information Compression Index (MICI)**

   MICI is an unsupervised feature selection method suitable for data with large dimensions and is based on measuring similarity between features whereby redundancy therein is removed. The feature selection task involves two main steps partitioning the original feature set into a number of homogeneous subsets (or clusters) and selecting a representative features from each such cluster. Partitioning of the features is based on a *K* nearest neighbour principle using feature similarity measure [181]. In doing so, first the *K* nearest features of each feature are computed. Among them the feature having the most compact subset (as determined by its distance to the farthest neighbour) is selected, and its *K* neighbouring features are discarded. The process is repeated for the remaining features until all of them are either selected or discarded.

4. **Laplacian Score (LS)**

   LS is based on Laplacian Eigenmaps [185] and Locality Preserving Projection [182]. The basic idea of LS is to evaluate the features according to their locality preserving power. LS is proposed in [182] to select features that retain sample locality specified by an affinity matrix *S*.

   For the r-th feature, $f_r = [f_{r1}, f_{r2}, ..., f_{rm}]^T$, define D = diag(S**1**), where $S_{ij} = cosine(x_i, x_j)$ (if nodes *i* and *j* are connected, else equal to zero) and $\mathbf{1} = [1, ..., 1]^T$. Define matrix L (graph Laplacian) as L = D-S.

Given *S*, its corresponding degree matrix *D* and Laplacian matrix *L*, the Laplacian Score of a r-th feature $f_r$ is calculated in the following way,

$$LS(f_r) = \frac{\tilde{f_r}^T L \tilde{f_r}}{\tilde{f_r}^T D \tilde{f_r}} \tag{4.26}$$

where

$$\tilde{f_r} = f_r - \frac{f_r^T D 1}{1^T D 1} 1 \tag{4.27}$$

Since features are evaluated independently in LS, selecting *K* features with LS can be achieved by greedily picking the top *K* features which have the minimal *LS* values.

## 4.3 Materials and Methods

The previous section introduced the mathematical background of the principal techniques by which automatic vessel classification was attempted in this thesis. The algorithms developed for vessel classification were tested and validated on three datasets: ORCADES, INSPIRE-AVR and DRIVE. This section details these datasets and it also discusses the methodology, i.e. the image processing and extraction of different of features, used for automatic vessel classification.

### 4.3.1 Datasets

1. **ORCADES** (Orkney Complex Disease Study)

   This dataset contains fundus camera images with a resolution of $2048 \times 3072$ pixels, captured with Canon CR-DGi non-mydriatic retinal camera and a $45^\circ$ FoV. ORCADES is a genetic epidemiology study based on an isolated population in the north of Scotland [186] [187]. It aims to discover the genes and their variants which influence the risk of common, complex diseases such as diabetes, osteoporosis, stroke, heart disease, myopia, glaucoma, chronic kidney and

lung disease. Finding these genes is the first step in order to develop new ways of diagnosing and treating these diseases. The North Isles of Orkney, the focus of this study, consist of a subgroup of ten inhabited islands with census populations varying from ˜30 to ˜600 people on each island. Although transport links have steadily improved between the North Isles and the rest of Orkney, the geographical position of these islands, coupled with weather and sea conditions, means that even today they are isolated and that they would have been considerably more so in the past. Studies in isolated populations have a number of advantages for identifying genes, including the ability to use information on the inheritance of variants through a family. Data collection was carried out in Orkney between 2005 and 2007. Informed consent and blood samples were provided by 1019 Orcadian volunteers who had at least one grandparent from the North Isles of Orkney. ORCADES is now a platform resource for health research in Scotland.

802 vessels from zone B of 70 ORCADES were extracted (see item 1 of section 4.3.3) and were labelled by two human trained observers to assess classification performance. Observer 1 (DR) is the author of this thesis and observer 2 (TM) is an imaging scientist. Both were involved in retinal imaging and analysis for clinical research. They were individually trained by experienced clinical colleagues in the identification of retinal vessel type. Observer 1 classified all vessels, while 1.5% of 802 vessels were not classified by observer 2 due to an uncertainty in deciding the label.

1,207 vessels from 70 ORCADES images were extracted from the extended zone (see item 2 of section 4.3.3) and were labelled by Observer 1 to generate the ground truth. All vessels were labelled by observer 1.

2. **INSPIRE-AVR** (Iowa Normative Set for Processing Images of the Retina)

   A publically available dataset containing 40 colour fundus camera images and an AVR reference standard [122]. Semi-automated computer software (IVAN) (University of Wisconsin, Madison, USA) was used to set the AVR reference standards. The dataset also contains AVR's calculated via manual annotations

by two different ophthalmologists, Ob1 whose AVR measurements were taken as the ground truth and Ob2 whose AVR measurements were used to determine the variability between human observers. Details pertaining to image acquisition (i.e. camera system, FoV) are not reported in [122].

Vessel classification was performed on $483$ vessels extracted from zone B of $40$ high-resolution color INSPIRE-AVR images of $2392 \times 2048$ pixels (extracted in a similar manner as explained in item 1 of section 4.3.3) to validate the performance of the proposed method. Observer $1$ generated the ground truth by labelling the vessels into *arterioles* or *venules* from which $10$ vessels were not labelled.

3. **DRIVE** (Digital Retinal Images for Vessel Extraction)

   It is a publically available dataset containing $40$ colour fundus camera images [188]. The retinal photographs were obtained from a diabetic retinopathy screening program in the Netherlands and were acquired using a Canon CR5 non-mydriatic 3CCD camera with a $45^\circ$ FoV. Images are $768 \times 584$ pixels and for each image one mask image is provided in the database that delineates the FoV. The set of $40$ images has been divided into a training and a test set, both containing $20$ images each.

   $171$ vessels from $20$ test images and $174$ vessels from $20$ training images in zone B were extracted (see item 1 of section 4.3.3) and labelled by observer $1$ to generate the ground truth and training set respectively. Observer $1$ labelled all vessels in test and training images.

### 4.3.2 Image Pre-processing

The presence of inter- and intra-image contrast, luminosity and colour variability affects vessel classification results [70]. So first, variations in background intensity were compensated for using a correction technique based on median filtering [5]. Background intensity was estimated by filtering with a mask of size $100 \times 100$ pixels. The mask size was chosen in such a way that it was several times bigger

than the expected maximum diameter of the retinal vessels. On testing with $25$ ORCADES images, $10$ DRIVE image and $10$ INSPIRE-AVR image, maximum vessel widths (found using VAMPIRE [12] [96]) were assessed to be $29$, $26$ and $27$ pixels, respectively. Correction coefficients for the background were calculated by dividing the maximum grey level value in the median filtered image by the grey level value of the currently considered pixel in the filtered image. Multiplying the input image with its correction coefficients gave the corrected image.

Figure 4.2 shows the images before and after the correction process. In addition, the hue channel was pre-processed, prior to background correction, to improve the contrast of vessels against background by mapping the original pixel intensity values between $1\%$ of bottom and $20\%$ of top pixel intensity values to values between $0$ and $1$ respectively. Figure 4.3 shows an example of the hue channel of an ORCADES fundus image before and after the contrast adjustment. The background corrected channels were then further processed to facilitate extraction of intensity measures or features from the extracted vessel's centerline pixels as follows.

### 4.3.3 Extracting Centreline Pixels

1. **Zone B**

   In order to extract vessel centreline pixels from zone B (i.e. the region between the blue concentric circles in Figure 4.4(a)) each vessel was tracked between two manually marked points, start (*S*) and end (*E*), see Figure 4.4(c) and 4.4(d). To do this, first, the vector defining the direction from *S* to *E*, $V_{S-E}$ was computed as $V_{S-E}$ = [$V_x$ $V_y$], where: $V_x$ = $d_e$cos($\theta$) and $V_y$ = $d_e$sin($\theta$), with $d_e$ as the Euclidean distance between *S* and *E* and $\theta$ = $tan^{-1}$($d_y$/$d_x$), and $d_x$ and $d_y$ are differences between $x$ and $y$ coordinates of points *E* and *S*. Then coordinates of the new point, $P_{new}$, $5$ pixels ahead of *S* was calculated as

$$P_{new} = S + 5(V_{S-E}). \tag{4.28}$$

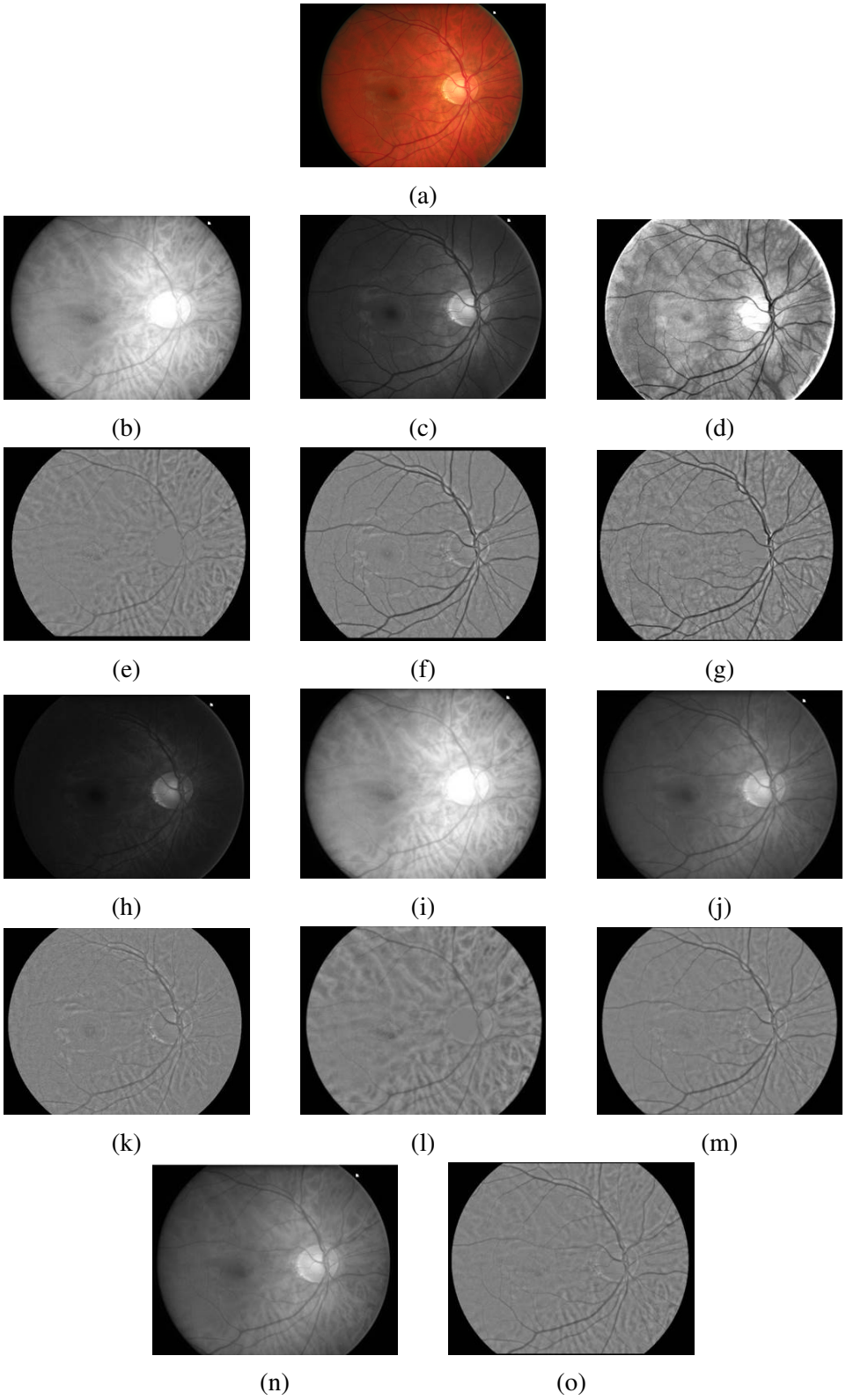


Figure 4.2: (a) Original colour or RGB Image; (b), (c), (d), (h), (i), (j) and (n) are uncorrected Red, Green, contrast adjusted Hue Channel, Blue, Value, Gray and L channels, respectively; and (e), (f), (g), (k) (l), (m) and (o) are illumination corrected Red, Green, Hue Channel, Blue, Value, Gray and L channels, respectively.

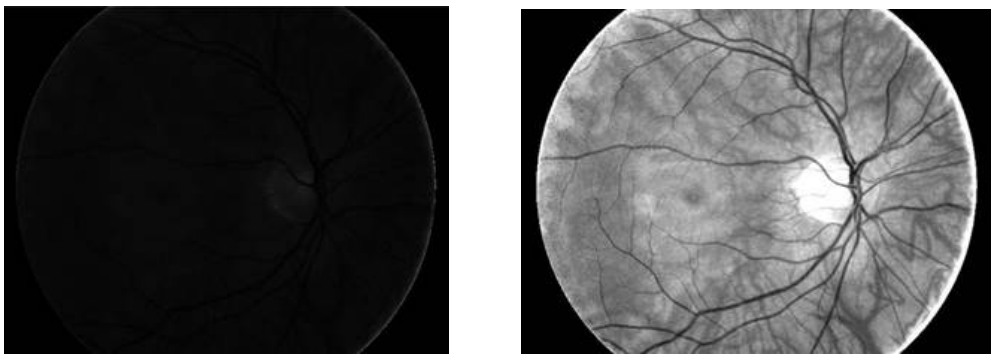

(a) (b)

Figure 4.3: H channel of an image from ORCADES dataset, (a) before and (b) after contrast adjustment. H channels of ORCADES images were very dark therefore contrast was improved before extraction of intensity features to assist subsequent vessel classification.

$P_{new}$ is shown in Figure 4.4(c). At $P_{new}$, the intensity profile across the vessel axis (and which resembles an inverted Gaussian; see Figure 4.4(b) which shows an example) was obtained. Point *C*, marked red on the intensity profile (see Figure 4.4(b), 4.4(c) and 4.4(d)), was then found by locating the 2 local minima on profile, marked as green dots in Figure 4.4(b), and averaging these points in order to give the approximate centre of the vessel. Then, the next $P_{new}$, marked as a yellow point ahead of $P_{new}$ in Figure 4.4(c), was calculated (using eq. 4.28) five pixels ahead of point *C* with vector direction $V_{C-E}$. This procedure continues until end point *E* was reached, i.e. cross-sectional intensity profiles were found at every $5^{th}$ pixel between *S* and *E* (blue lines in Figure 4.4(d)). Next, the Canny edge detector [189] was applied to each of these profiles to locate vessel edges (marked as yellow in Figure 4.4(d)) and finally the centreline pixels (marked as pink in Figure 4.4(d)) were located as the midpoint of a pair of edge points. In this way, the centreline pixels were extracted from vessels in each quadrant (i.e. from quadrant I, II, III and IV; see Figure 4.4(a)) and this provided a set of *n* vessel segments: $S = V_1, V_2,...,V_n$, where $V_i$ is $i^{th}$ vessel and each vessel is represented by a set of *m* centreline pixels: $V_i = p_1, p_2,...,p_m$. For each centreline pixel $p_k$, the *x* and *y* coordinates and the vessel diameter *d* were stored.

2. **Extended Zone**

Vessel classification was also conducted in an extended zone, i.e. outside of the conventional zone B, which was specified by first dividing an image into four quadrants after locating the OD and its approximate diameter *d* [94]. If the OD was on the right side of the fundus image then the zone from OD margin to $1.75d$ was specified in quadrants I and IV (see Figure 4.5). Whereas in quadrants II and III, specified zones were from the OD margin to $1d$ (Figure 4.5). If the OD was on the left side of the fundus image then the zone from the OD margin to $1.75d$ was specified in quadrants II and III, but in quadrants I and IV it was from the OD margin to $1d$. The size of the classification zone was dictated by the fact that vessels tend to lose contrast towards the extremities of the image (see Figure 3.2(b) shows an example) and this leads to problems with segmentation and hence classification.

A binary vessel map was generated using VAMPIRE [12] [52]. After specifying the extended zone, all the detectable vessels inside it were extracted from the segmented vessel map. Finally, only those vessels whose width was at least $55\%$ of maximum width of the vessels in a pair of quadrants and whose length was at least $15$ pixels were considered. These criteria were arrived experimentally i.e. the experiment was also performed by selecting vessels whose width was at least $60\%$ of maximum width of the vessels in a pair of quadrants but the number of vessels selected were lesser then when $55\%$ criterion was used. Moreover using $50\%$ criterion for vessel selection, very tiny vessels were selected. Therefore in order to select large number of vessels with reasonable width $55\%$ criterion was found to be reasonable. During vessel selection, if no vessels satisfied the conditions ($55\%$ criterion with length at least $15$ pixels), i.e. if no vessels were selected in a particular quadrant, then the vessel with maximum width in that particular quadrant was selected.

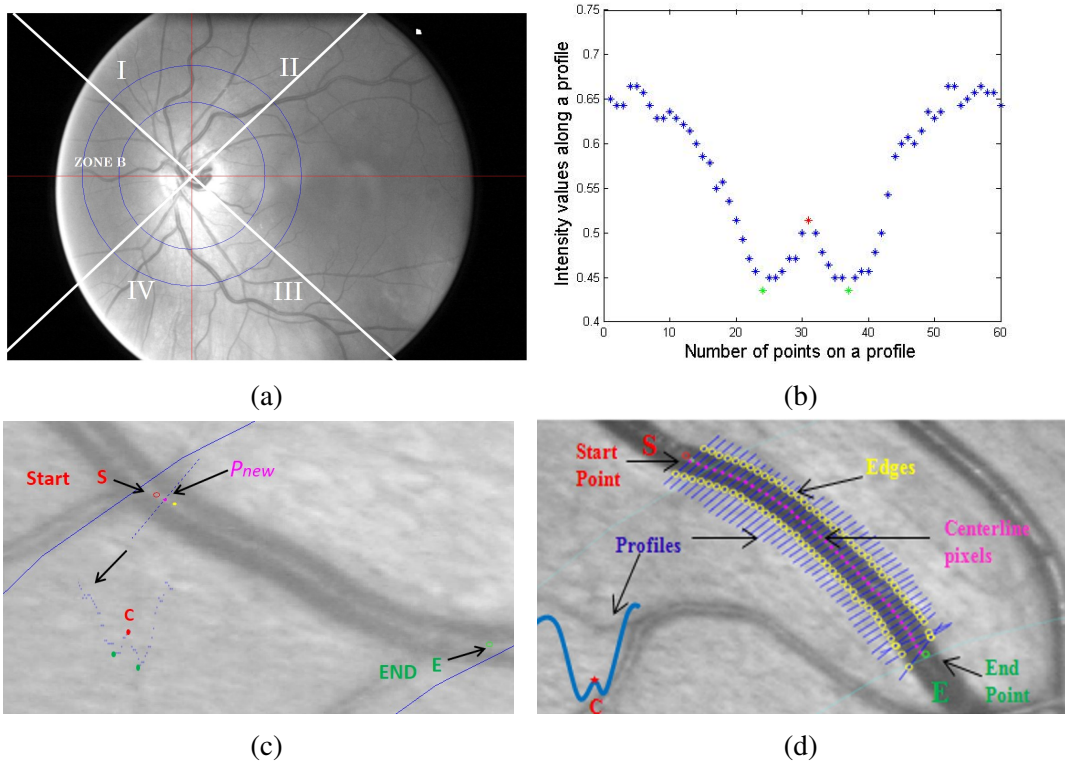


Figure 4.4: (a) Rotated co-ordinate axes of the normal co-ordinates axes (marked as red line in the image) by $45^\circ$ (marked as white line in the image) and measurement zone: zone B (0.5 to 1 disc diameter from the optic disc margin surrounding the OD), (b) Vessel profile, (c) Centreline pixels were extracted between manually placed Start (S) and End (E) points, (d) Vessel edges (marked as yellow) were located (from cross-sectional intensity profiles (marked blue line) using Canny edge detector [189]) and the centreline pixels (marked as pink) were then found as the midpoint of a pair of edge points.

### 4.3.4 Feature Extraction

With both unsupervised (GMM-EM and SMIC) and supervised (LS-SVM) approaches, four fixed ROI-based colour features (i.e. mean of red - *MR*, mean of green - *MG*, mean of hue - *MH* and variance of red - *VR*) were extracted by sampling inside the vessels in the corrected channels using a circular neighbourhood around each centreline pixel, with diameter $60\%$ of the mean vessel diameter. These four fixed colour features were used as they were considered to be the best and effective features for retinal vessel classification [70] [118] [190]. Vessels from ORCADES and DRIVE images were classified using these four features whereas INSPIRE-AVR images were classified using only MR, MG and VR due to poor hue channel quality.

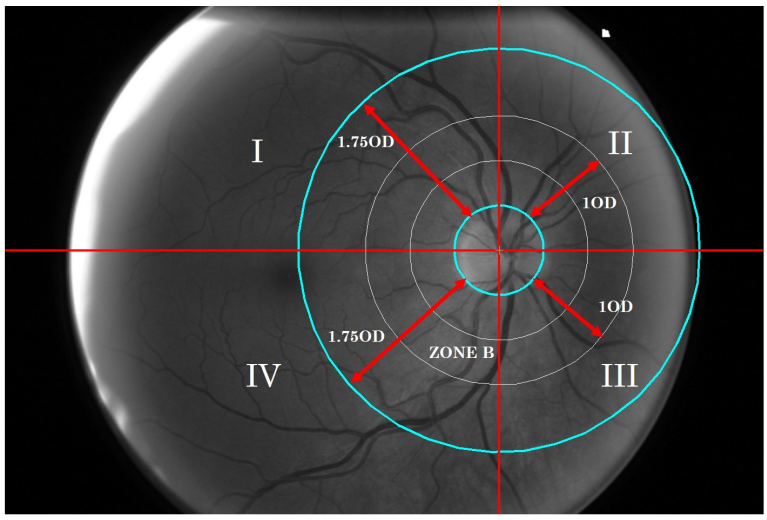


Figure 4.5: Specifying an extended zone for vessel classification around the OD. This image is of a right eye (i.e. the OD is on right) from ORCADES dataset where the extended classification zone is from the OD margin to $1.75$ times the OD diameter in quadrants I and IV.

See Figure 4.6 which shows an example of HSV image and hue channel with lots of saturation making it difficult to distinguish vessels.

The focus of dimensionality reduction was to classify vessels using the most dominant features, *DF*, from the total set of original features, *TF*, with *DF*<*TF*, in each image. ROI-based features, profile-based features and contrast of vessels w.r.t. background were extracted. The details of this is discussed as follows:

1. **ROI-based** - Features were extracted from different background corrected channels using a circular ROI around each centreline pixel, with diameter $60\%$ of the mean vessel diameter, to calculate the intensity level inside the vessel. This included **R**, **G** and **B** from the **RGB**, **H** and **V** from the **HSV**, **L** from **L**ab colour spaces, and Gray **(Gy)** image (converted from RGB image (where $Gy = 0.299 \times \mathbf{R} + 0.587 \times \mathbf{G} + 0.114 \times \mathbf{B}$).

2. **Profile-based** - Features were extracted from the background corrected **R** and **G** channels from the **RG**B colour space after additional contrast adjustment (by mapping the intensity values in input image to new values such that $1\%$ of data is saturated at low and high intensities value of input image) from a profile line

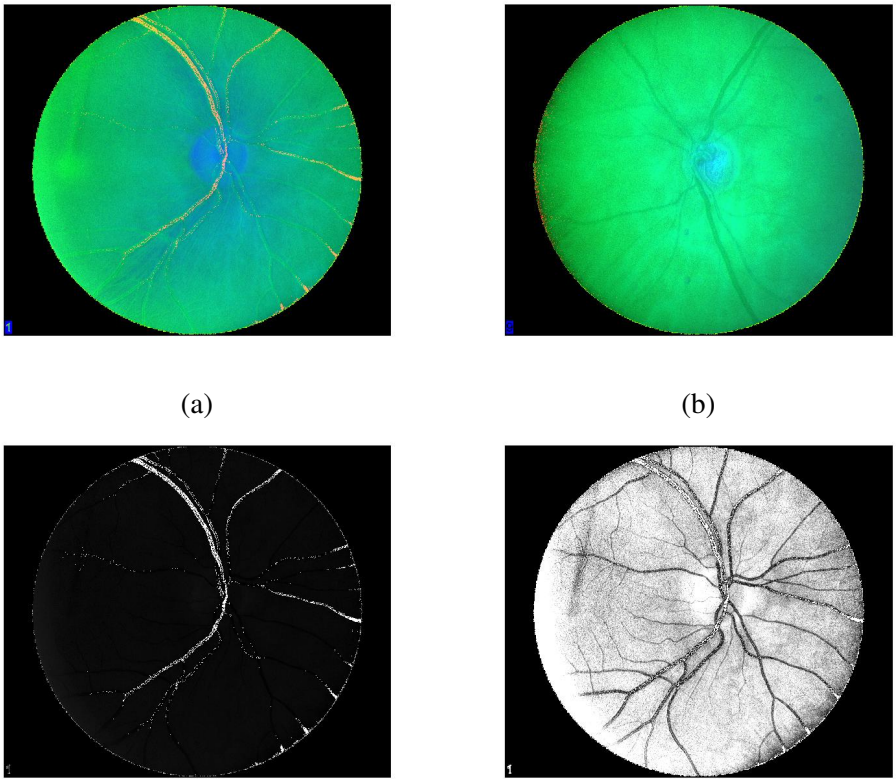

(a) (b)

(c) (d)

Figure 4.6: Images from the INSPIRE-AVR dataset showing examples of (a) a poor quality HSV image with a lot of variation in intensity for vessels, (b) a good HSV image with a more stable vessel intensity, (c) a poor hue channel and (d) contrast adjusted hue channel.

placed perpendicular to vessel centreline axis and of length $60\%$ of the mean vessel diameter.

3. **Contrast** - Contrast of a vessel w.r.t. background from the corrected **R** and **G** channels was extracted after additional contrast adjustment in a similar manner as explained above for profile based feature. For each centreline pixel, a profile of length $2.5$ times the width of the vessel was drawn. On each end of the profile, mean intensity $I_{b1}$ and $I_{b2}$, from two circular ROI's (whose diameters were $60\%$ of the mean vessel diameter, and a centre as the end point of profile) were obtained as shown in Figure 4.7. The average of these two intensities, $I_b$, was calculated and this represented the background intensity. The mean intensity $I$ from a circular neighbourhood around the centreline pixel (with diameter $60\%$ of the mean vessel diameter) was extracted as the vessel intensity. The contrast

feature, *C*, was then calculated using eq. 4.29

$$C = \frac{I - I_b}{I_b} \tag{4.29}$$

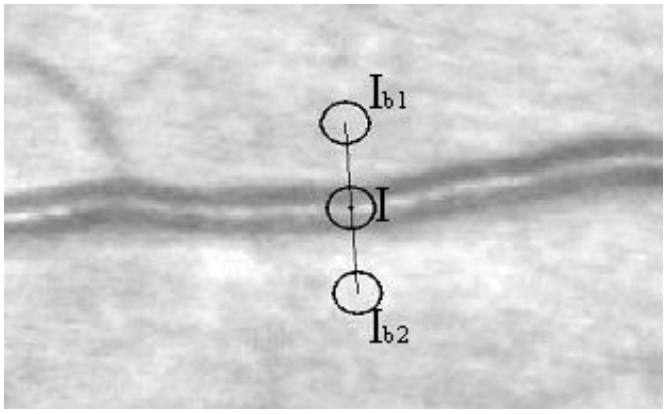


Figure 4.7: Extracting contrast features w.r.t. retinal background. $I$ is the mean intensity extracted from circular ROI inside the vessels while $I_{b1}$ and $I_{b2}$ are the mean intensity extracted from circular ROI from the vessel background on either side of the vessel.

For ROI and profile-based colour features, mean *(M)*, standard deviation *(Std)*, variance *(Var)*, minimum *(Min)* and maximum *(Max)* values from each of the channels were extracted. This along with contrast features, created a set of $47$ features for each image. See Table 4.1 which summarises the feature set.

| Features | No. of Features | Channels | No. of Channels | Total No. of Features |
|---|---|---|---|---|
| **ROI-based:** | 5 | G , R, B, | 7 | 35 |
| M, Std, Var, Min, Max | | H, V, L, Gy | | |
| **Profile-based:** | 5 | G, R | 2 | 10 |
| M, Std, Var, Min, Max | | | | |
| **Contrast** | 1 | G, R | 2 | 2 |

Table 4.1: Total number of features extracted from each image

From the set of $47$ features different subsets consisting of $9$, $12$, $15$, $32$, $37$, $42$ and $47$ features were formed to investigate the influence of different features and feature set dimensions on the classification output in conjunction with the dimensionality

reduction techniques. See Table 4.2 for a summary. The feature subsets with lower dimensions (i.e. 9-15 features) were formed using ROI based colour features, which are commonly reported as discriminant features [6] [122] [124] to classify retinal vessel type - i.e. those extracted from R, G, B, H and V colour space channels. In contrast, the feature sets with higher dimensions (32-47) were formed with ROI-based colour, profile-based and contrast based features from R, G, B, H, V, L channels and Gy image.

In an RGB colour fundus image, the green and red channels usually show good contrast discrimination between arterioles and venules, and therefore a feature set with dimension 9 was formed by combining the features extracted from the red and green channels with those extracted from **B**lue, **H**ue and **V**alue colour channels respectively. These feature set are referred as 9**B**, 9**H** and 9**V** henceforth, respectively.

### 4.3.5 Quadrant Pairing and Vessel Voting

As described earlier, each input retinal image was divided into four quadrants by locating the OD and its approximate diameter. Vessel classification was performed by working separately on two quadrants at a time in a clockwise direction, i.e. vessels from quadrant combinations (I, II), (II, III), (III, IV) and (IV, I) (see Figure 4.4(a)).

For unsupervised classification (GMM-EM and SMIC) after four ROI-based colour feature extraction there were four sets of feature vectors $F_q$, $q$=1 ,..., 4, for each pair of quadrant - i.e. for pairs (I, II), (II, III), (III, IV) and (IV, I). Each set is represented by a $N_i \times 4$ matrix, where $N_i$ is the number of pixels in a pair of quadrants and 4 represents the number of fixed features. See section 4.3.4 for details of four features used for classification. Finally, each set of colour features ($F_q$) of pixels (representing sample points describing the vessels from pairs of quadrant) were classified using the unsupervised classifiers.

Quadrant-pairwise vessel classification was performed using unsupervised classifiers (GMM-EM and SMIC) whereas for classification performed on whole

| Total Features | | Features Set |
|---|---|---|
| **9** | **ROI based:** GRB (**9B**) | **ROI based features:** M, Std., Var. from G, R, and B channel |
| | **ROI based:** GRH (**9H**) | **ROI based features:** M, Std., Var. from G, R, and H channel |
| | **ROI based:** GRV (**9V**) | **ROI based features**: M, Std., Var. from G, R, and V channel |
| **12** | **ROI based:** GRBH | **ROI based features:** M, Std., Var. from G, R, B and H channel |
| **15** | **ROI based:** GRBHV | **ROI based features:** M, Std., Var. from G, R, B, H and V channel |
| **32** | **ROI based:** GRBHVL<br>**Contrast:** G and R channel | **ROI based features:** M, Std, Var, Min, Max from G, R, B, H, ,V and L channel **+**<br>**Contrast** from G and R channel |
| **37** | **ROI based:** GRBHVLGy<br>**Contrast:** G and R channel | **ROI based features:** M, Std, Var, Min, Max from G, R, B, H, V, L channel and Gy image **+**<br>**Contrast** from G and R channel |
| **42** | **ROI based:** GRBHVL<br>**Profile based:** G and R channel<br>**Contrast:** G and R channel | **ROI based features:** M, Std, Var, Min, Max from G, R, B, H ,V and L channel **+**<br>**Profile based features:** M, Std, Var, Min, Max from G and R **+**<br>**Contrast** from G and R channel |
| **47** | **ROI based:** GRBHVLGy<br>**Profile based:** G and R channel<br>**Contrast:** G and R channel | **ROI based features:** M, Std, Var, Min, Max from G, R, B, H ,V and L channel and Gy image **+**<br>**Profile based features:** M, Std, Var, Min, Max from G and R **+**<br>**Contrast** from G and R channel |

Table 4.2: Different Feature sets consisting different colour features extracted from R,G,B,H,V, L channels and grey image.

zone the supervised LS-SVM was employed. Figure 4.8 illustrates the flow chart for a/v classification using unsupervised classification. This is essentially the same for supervised vessel classification using LS-SVM except that it was not performed quadrant-pairwise but on the whole zone and there is a training step to note.

The feature vector (in case of vessel classification with LS-SVM) is represented by a $4 \times N_w$ matrix, where $N_w$ is the number of pixels in whole zone and $4$ represents the number of features used for classification. Pixels each with the set of four colour features ($F$) were then classified using LS-SVM. To the best of knowledge, these are the first implementations of GMM-EM, SMIC and LS-SVM for retinal vessel classification.

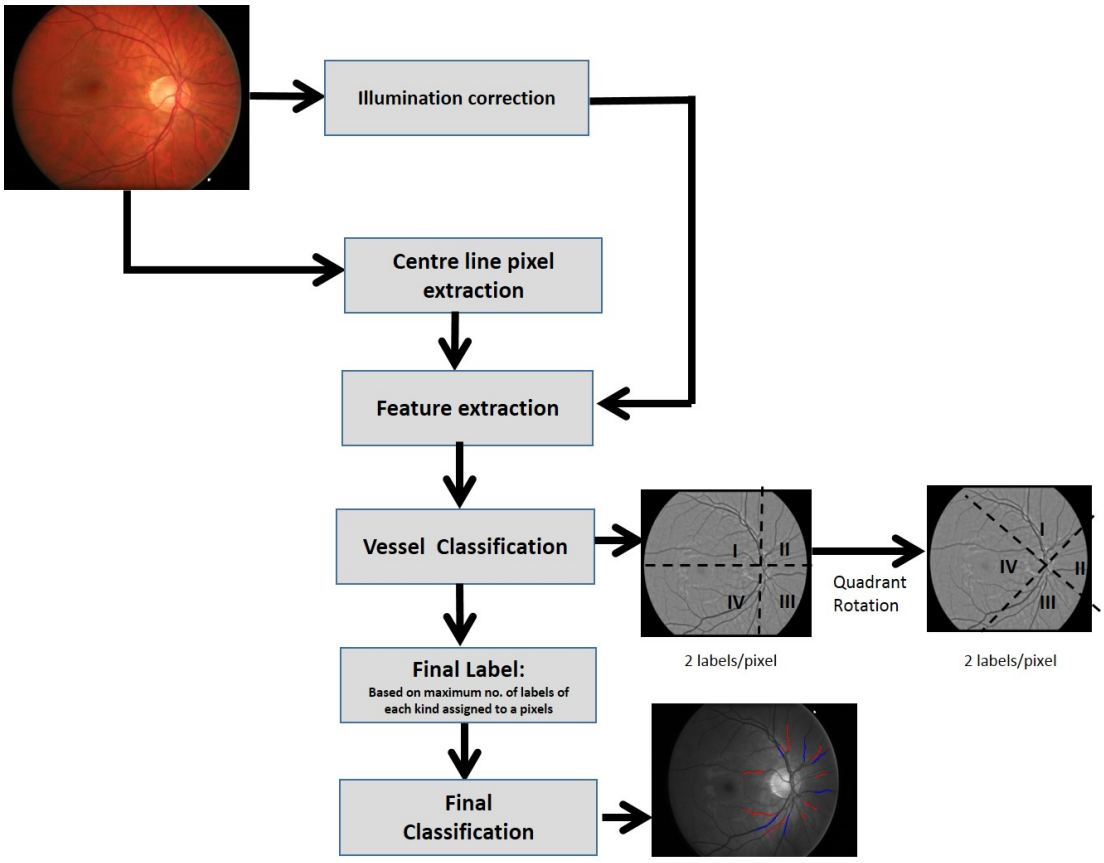


Figure 4.8: A-V classification algorithm using GMM-EM and SMIC

The centroid of each cluster generated by the unsupervised classifiers was associated with a vector of four mean values representing the four colour features. The two mean values of the green channel (as this channel gives the best discrimination

between vessels) intensity representing the centroids (i.e. for two clusters) were compared to determine their class. The cluster with the higher mean green channel intensity was defined as *arteriole* and the lower as *venule* [121]. The third cluster was *not labelled*.

Considering vessel pixels from a pair of quadrants for unsupervised classification, one label was assigned to each pixel. As each quadrant was considered twice in the processing, i.e. for pairs (I, II), (II, III), (III, IV) and (IV, I), each pixel has two labels assigned to it in total. Then the coordinate axes of the quadrant was rotated $45^\circ$ clockwise (white solid lines in Figure 4.4(a)) and the pixels belonging to each of the rotated quadrants were classified again, generating two more labels for each pixel. In this way each pixel had four labels from a group of: *a* (for *arterioles*), *v* (for *venule*) and *n* (for *not labelled*). The coordinate axes of quadrants were rotated so that each vessel was classified several times which improved the chances of achieving correct final classification. Each pixel was then assigned a final status of *A* (for *arteriole*), *V* (for *venule*) and *N* (for *not labelled*) based on the maximum votes (out of $4$). Finally, the vessel was assigned the final status (*arterioles* or *venule*) based on the maximum votes assigned to its centreline pixels of a vessel.

In Table 4.3, the first column shows the pixels belonging to a vessel while the second column shows the four labels assigned to each pixel. The final label of each pixel (column III in Table 4.3) was decided based on following logic:

I. IF number of *a* $>$ number of *v*: then assign *A* - *(e.g. n v a a = A)*

II. IF number of *v* $>$ number of *a*: then assign *V* - *(e.g. n a v v = V)*

III. IF (number of *a* = number of *v*) - *(e.g. a a v v)*

*OR*

*IF* (number of *n* $>$ number of *a or v) - e.g. (n n n a) or (n n n v )*

*OR*

*IF* (number of *n* = number of *a or v) - e.g. (n n a a) or (n n v v)*: then assign *N*

After each pixel has been classified *(A, V or N)* (column III), the maximum votes from the pixels in a vessel decide the vessel's class. Table 4.3 shows an example of a vessel assigned a status of *arteriole* based upon the most *A* labels in column III.

| Pixel number | Labels per pixel | Final label |
|---|---|---|
| 1 | *a a a a* | A |
| 2 | *a a v a* | A |
| 3 | *a a v a* | A |
| 4 | *a a a a* | A |
| 5 | *a v v a* | N |
| 6 | *a n n a* | N |
| 7 | *a n a a* | A |

Table 4.3: Example of assigning a final status of *arteriole* to a vessel based on maximum *A's* in column III

The supervised LS-SVM classifier classifies the pixels in the whole zone, labelling each pixel as either *a* or *v*. Thereafter, labels were counted for all pixels in a vessel, and the maximum vote was assigned to the vessel status (i.e. *arterioles* or *venules*). If the vote was tied the vessel was marked *not labelled*.

For vessel classification utilising the four dimensionality reduction techniques, a set of $47$ features were used (see section 4.3.4). Different subset consisting of $9$, $12$, $15$, $32$, $37$, $42$ and $47$ features from the set of $47$ features were formed (see section section 4.3.4 ) and from each subset the optimal features were determined using dimensionality reduction technique which were then used along with GMM-EM to classify vessels in quadrant-pairwise approach. The best performed dimensionality reduction technique in the above experiment was also used along with SMIC classifier with only lower (9) and higher dimension (32 and 47) to demonstrate the performance with different classifier ( see section 5.2.4 of chapter 5 for results).

### 4.3.6 Quantifying Performance

Using the ground truth detailed in section section 4.3.1, the classification performance was evaluated, separately for arterioles *(*a) and venules (*v*), using the following parameters [117],

$$\text{Sensitivity} = \frac{TP_{a/v}}{(TP_{a/v} + FN_{a/v})} \tag{4.30}$$

$$\text{Specificity} = \frac{TN_{a/v}}{(TN_{a/v} + FP_{a/v})} \tag{4.31}$$

$$\text{Positive Predicted Value} = \frac{TP_{a/v}}{(TP_{a/v} + FP_{a/v})} \tag{4.32}$$

$$\text{Negative Predicted Value} = \frac{TN_{a/v}}{(TN_{a/v} + FN_{a/v})} \tag{4.33}$$

$$\text{Positive Likelihood Ratio} = \frac{Sensitivity}{(1 - specificity)} \tag{4.34}$$

$$\text{Negative Likelihood Ratio} = \frac{(1 - Sensitivity)}{specificity} \tag{4.35}$$

$$\text{Classification Accuracy} = \frac{(TP_{a/v} + TN_{a/v})}{(TP_{a/v} + TN_{a/v} + FP_{a/v} + FN_{a/v})} \tag{4.36}$$

$$\text{Classification Error Rate} = \frac{(FP_{a/v} + FN_{a/v})}{(TP_{a/v} + TN_{a/v} + FP_{a/v} + FN_{a/v})} \tag{4.37}$$

where *TP* is *True Positive*, *FP* is *False Positive*, *TN* is *True Negative* and *FN* is *False Negative*. These are further defined as [117]:

- True Positive$_{\mathbf{a}rtery(\mathbf{v}ein)}$ ($TP_{a/v}$): When both the system and the observer identified a vessel as arteriole (or venule).
- False Positive$_{\mathbf{a}rtery(\mathbf{v}ein)}$ ($FP_{a/v}$): When the system identified a vessel as arteriole (or venule) and the observer identified it as venule (or arteriole).
- True Negative$_{\mathbf{a}rtery(\mathbf{v}ein)}$ ($TN_{a/v}$): When the observer identified a vessel as venule(arteriole) and the system identified it as not arteriole (venule)(i.e. either as venule (arteriole) or not labelled)
- False Negative$_{\mathbf{a}rtery(\mathbf{v}ein)}$ ($FN_{a/v)}$): When the system did not identify a vessel as arteriole (or venule), i.e. either as venule(arteriole) or not labelled, and the observer identified it as arteriole (venule).

### 4.3.7 Classification Experiments

This section summarises all classification experiments and briefly explain the dataset, zone, number of vessels and features used for vessel categorisation. The results obtained using unsupervised, supervised and dimensionality reduction classification experiment are detailed in section 5.2.2, 5.2.3 and 5.2.4 respectively of chapter 5.

1. **Unsupervised vessel classification - GMM-EM and SMIC**

   (a) **ORCADES**

   Unsupervised classifiers were used to automatically classify $802$ retinal vessels in zone B from $70$ ORCADES images using $4$ fixed colour features

(i.e. *MR*, *MG*, *MH* and *VR*) and a quadrant-pairwise approach. An experiment was also conducted in the extended zone on $1,207$ vessels with same $4$ fixed colour features and quadrant-pairwise approach.

(b) **INSPIRE-AVR**

$483$ vessels from $40$ images from INSPIRE-AVR dataset were used for a quadrant-pairwise vessel classification in zone B using only three feature (i.e. MG, MR and VR) as the Hue channel was of poor quality.

(c) **DRIVE**

The approach were also tested on $171$ vessels in zone B of $20$ DRIVE test images using the four colour features (*MR*, *MG*, *MH* and *VR*).

2. **Supervised Vessel Classification**

(a) **ORCADES**

The ORCADES images were used to assess supervised classification. LS-SVM was trained and tested using four colour features (*MR*, *MG*, *MH* and *VR*). LS-SVM was trained using labels generated by observer $1$. Two experiments were performed separately. In the first experiment (Exp$5$), training was performed with a subset of $5$ randomly chosen images while in the second experiment (Exp$10$), $10$ randomly chosen images were used for training. In Exp$5$ the classifier was trained with $59$ vessels in zone B and $72$ vessels in the extended zone. In Exp$10$, $115$ vessels were used for training in zone B and $175$ for the extended zone. The testing set of $60$ images was kept the same for both experiments. LS-SVM was then used to classify $687$ vessels in zone B and $1031$ vessels in the extended zone in both Exp$5$ and Exp$10$.

The same experimental protocol was repeated five more times, choosing training images $5$ for Exp$5$ (Exp$5_5$) and $10$ for Exp$10$ (Exp$10_5$)) randomly each time from the set of $70$ images. A further experiment was also conducted to assess the system performance when the classifier was trained with the vessels (from $5$ and $10$ images) in the extended zone and then

tested on the vessels (from $60$ images) in zone B. Classification rate was calculated w.r.t labels generated by observer $1$

(b) **DRIVE**

The system was also tested on $171$ vessels extracted from zone B of $20$ images using four fixed colour features (*MR*, *MG*, *MH* and *VR*). The classifier was trained with $174$ vessels extracted from zone B of $20$ training images using same four fixed colour features. Classifier was trained and classification rate was evaluated using labels generated by observer $1$.

3. **Unsupervised Vessel Classification with Dimensionality Reduction Techniques**

Vessel classification was performed in zone B using GMM-EM and a quadrant-pairwise approach on ORCADES images using the dominant features as calculated by dimensionality reduction (i.e. PCA, OLPP, MICI and LS). It was observed that the feature selection methods of MICI and LS gave different classification results with different numbers of optimal features. Therefore, experiments were conducted to identify the number of optimal features for which the classification rate is maximised.

MICI and LS rank features from the most to least relevant. When vessel classification was performed using the optimal features selected by LS at lower dimensions (i.e. $9-15$ features, see Table 4.2) on the ORCADES images, it was observed that the classification rate was at a maximum for $3$ features. Repeating at higher dimensions (i.e. $32-47$ features) it was observed that for $32$ and $42$ features, the maximum classification rate was obtained with $3$ optimal features. Whereas for $37$ and $47$ features the classification rate increased by choosing up to $6$ relevant features, and decreased thereafter. Chapter 5 shows classification results after choosing the $3$ most relevant features from $9, 12, 15, 32$ and $42$ features in feature set and $6$ most relevant features predicted by LS from $37$ and $47$ features.

Similarly for MICI, with a lower dimensional feature set (i.e. $9-15$ features), the number of optimal features was found to be $3$. Whereas for $37$ and $47$

features, the classification rate improved by including up to $8$ of the most relevant features, and decreased thereafter. However, for $32$ and $42$ features, the optimal numbers for classification were found to be $9$ and $10$, respectively. Chapter 5 indicates the classification results using MICI for which classification rate obtained was maximised on choosing optimal number of features for a particular dimensionality of the feature set.

In certain data analysis techniques, high-dimensional data can be replaced by its projection onto the most important axes, and these axes are the ones corresponding to the largest Eigen values. Thus the original data is approximated by data with fewer dimensions (by choosing the most dominant Eigen values), which summarises the original data well [191]. PCA and OLPP fall into this class of data analysis techniques, therefore, Eigen vectors corresponding to high Eigen values were extracted for generating a new feature set. With PCA and OLPP, transformed features were then used for vessel classification. In PCA, the three principle components were used in vessel classification as these were found to be sufficient to explain $97\%$ (or more) of the total variance described by the whole feature set.

After experimenting on $10$ images, it was found that at lower dimensions, highest Eigen values of the feature set matrix ranged from $0.9$ - $0.95$ while at higher dimensions they ranged between $0.95 - 0.99$. So to select the most important features (corresponding to high Eigen values) a cut-off of $0.9$ and $0.95$ was used at lower and higher dimensions, respectively. Thus in OLPP, the Eigen vectors corresponding to Eigen values greater than or equal to $0.9$ (at lower dimensions i.e. for the $9, 12$ and $15$ features in the feature set) and $0.95$ (at higher dimensions i.e. for the $32, 37, 42$ and $47$ features in the feature set) were used to transform the original feature set. This exercise was carried out for feature sets in each image and these transformed features were then used for classification.

## 4.4 Reducing Unclassified Vessels

During the unsupervised vessel classification process if the number of votes for a particular vessel class ties then it remained unlabelled or unclassified. In order to reduce the number of unclassified vessels, the colour features of these vessels were compared quadrant-pairwise with that of the classified arterioles and venules.

Let each image have *n* vessels, i.e. S = $V_{1k}$,$V_{2k}$, . . . , $V_{nk}$, where $V_{ik}$ is $i^{th}$ vessel in $k_{th}$ quadrant. Each vessel is represented by a set of $m$ centreline pixels: $V_{ik}$ = $p_{1k}$, $p_{2k}$, . . . , $p_{mk}$. On each centreline pixel in the vessel of unclassified and classified vessels, MR and MG were extracted. Then the average of MR and MG from all centreline pixels of each of the vessel $V_{ik}$ in all four quadrants *(k*=1, . . . , 4*)* were calculated - separately for unlabelled vessels (*u*), arterioles (*a*) and venules (*v*). Then each unlabelled vessels, arterioles and venules were represented by [MGu MRu], [MGa MRa] and [MGv MRv] respectively. From all the arterioles in a pair of quadrants the one which has maximum MG (MGamax) and its corresponding MR (MRac) was selected. This gives a vector [MGamax MRac]. Similarly, from all venules in a pair of quadrants the one which has minimum MG (MGvmin)and its corresponding MR (MRvc) was selected and this was represented as a vector [MGvmin MRvc]. Then, [MGu MRu] was compared with [MGamax MRac] and [MGvmin MRvc] quadrant-pairwise in order to assign a label to the unlabelled vessel. For instance, first [MGu MRu] was compared with [MGamax MRac] and [MGvmin MRvc] in quadrant pairs (I, II). If the absolute difference between [MGu, MRu] and [MGamax MRac], respectively is less than the absolute difference with [MGvmin MRvc], a soft label of *arteriole* was assigned. Alternatively, if the absolute difference between [MGu, MRu] and [MGvmin MRvc], respectively is less than the absolute difference with [MGamax MRac], a soft label of *venule* was assigned. Likewise the colour features of unclassified vessels were compared with that of classified arterioles and venules in remaining quadrant pairs (II, III), (III, IV) and (IV, I) assigning one more soft labels. Finally, each unclassified vessel was assigned a deciding label based on the polling of soft labels. If the vote was tied the vessel remained unclassified.

## 4.5 AVR

Vessel classification is a precursor to the calculation of AVR. Computational measurements of AVR were tested on the INSPIRE-AVR dataset due to availability of the ground truth. AVR was computed by first classifying vessels in zone B using GMM-EM, SMIC classifier and dimensionality reduction with GMM-EM. Classification with GMM-EM and SMIC was performed with quadrant-pairwise approach and only $3$ features - *MG*, *MR* and *VR*. For vessel classification with a framework using OLPP dimensionality reduction method in conjunction with quadrant-pairwise GMM-EM, a total of $15$ features (M, Std, Var, Min and Max features extracted from each of the green, red and value channels) were used. Eigen values $\geq 0.9$ was used for selecting important features. After vessel classification the width of the vessels were evaluated [12] [96]) to calculate AVR using three methods - Knudtson [127], Goatman [129] and Patton method [126] described in algorithm 1, 2 and 3 respectively in section 3.3. In order to evaluate the ability of the thesis AVR system, Bland-Altman analysis and Student's paired t-test was performed. Data analysis was performed on Microsoft Office Excel 2013.

## 4.6 Conclusions

In this chapter automatic methods for retinal vessel classification have been proposed which make use an unsupervised and supervised techniques and colour as the source of distinguishing features. A framework was presented that uses unsupervised classification and a quadrant-pairwise approach, but unlike previously reported methods it does not require the presence of at least one arteriole and one venule per quadrant, and is applicable even if there are no vessels present in a quadrant. Generating training data for supervised classification is time consuming and arduous, however these methods tend to out-perform unsupervised techniques. Hence a supervised method for vessel classification was also presented. Classifying vessels

by predefining features for all images may lead to misclassification. Therefore, a framework was designed in which the optimal features were selected from a bank of features using dimensionality reduction prior to quadrant-pairwise unsupervised classification. This chapter also discussed a method to reduce the number of unclassified vessels. Finally, testing measurements of AVR following vessel classification was also presented.

# Chapter 5

# Assessing Vessel Classification and AVR

## 5.1 Introduction

This chapter presents the results obtained by using unsupervised and supervised vessel classification algorithms, when only four fixed features were used. Furthermore, this chapter also discusses the performance of the classification algorithms when an optimal set of features were selected from a bigger set using dimensionality reduction techniques. The main hypothesis tested here is the effect of using a fixed set of features for the vessel classification. An unsupervised classifier may lead to misclassification with large number of vessels remained unclassified, whereas for the supervised classifier the opposite may be true. In addition, study was also conducted to test if AVR measurement is highly dependent on the classification performance.

As discussed in Chapter 3, effective computerised vessel classification is a precursor to the automatic measurement of AVR, and is desirable for examining large number of images in an efficient manner. This chapter presents an assessment of performance for these two vital components of a retinal image analysis system. In section 5.2, the results achieved using unsupervised methods on images from the

ORCADES, INSPIRE-AVR and DRIVE datasets are given along with those attained using supervised approaches on ORCADES and DRIVE. Section 5.3 presents results obtained utilising the three algorithms introduced in Chapter 3 for calculating the AVR. Finally, a discussion and conclusions to these findings are presented in section 5.4 and 5.5, respectively.

## 5.2 Vessel Classification

### 5.2.1 Manual Annotation

The manual labelling of $802$ vessels in zone B from $70$ ORCADES images by two trained human observers was used to assess the performance of computerised vessel classification.

The performance measures introduced in section 4.3.6 of chapter 4 were computed for observer $1$ (separately for arterioles and venules) w.r.t. the labels of observer $2$ and are given in Table 5.1. This demonstrates the high level of agreement between the two observers. Moreover, it was observed that the discrepancy in labelling vessels by two observers were found for only two vessels (out of the vessels labelled as arterioles or venules by two observers). Thus, the results in the subsequent section are given w.r.t. observer $1$.

| Performance Measure | Arteries | Veins |
|---|---|---|
| *Sensitivity* | 0.9976 | 0.9973 |
| *Specificity* | 0.9973 | 0.9976 |
| *Positive Predicted value* | 0.9976 | 0.9973 |
| *Negative Predicted value* | 0.9973 | 0.9976 |
| *Positive Likelihood Ratio* | 367.13 | 420.85 |
| *Negative Likelihood Ratio* | 0.0024 | 0.0027 |
| *Classification Accuracy* | 0.9975 | 0.9975 |
| *Classification Error rate* | 0.0025 | 0.0025 |

Table 5.1: Table showing the performance of observer $1$ w.r.t. observer $2$ who both manually labelled vessels as arterioles or venules on the ORCADES dataset ($70$ images; $802$ vessels).

### 5.2.2 Unsupervised Classification

The experimental results using unsupervised classification methods, i.e. GMM-EM and SMIC, for vessel categorisation are detailed below. The classification percentage was calculated when unclassified vessels were not considered.

1. **GMM-EM**

   The GMM-EM classifier in conjunction with a quadrant-pairwise approach (see section 4.3.5) was utilised to automatically classify retinal vessels in zone B of the illumination corrected fundus images using only $4$ fixed colour features (*MR*, *MG*, *MH* and *VR*) (described in section 4.3.4). On the ORCADES dataset (i.e. $802$ vessels from $70$ images) a classification accuracy of $90.45\%$ was obtained, whereas $13.8\%$ vessels remained unclassified. See Table 5.2, where *C* is the percentage of correctly classified vessels and *Un* stands for the unclassified vessels, w.r.t. the manual annotation of observer $1$. Table 5.2 also summarises the results obtained by an experiment conducted in an extended zone on $1,207$ vessels (see section 4.3.3)

| Classifier | Zone B | Extended Zone |
|---|---|---|
| | C/Un% | C/Un% |
| *SMIC* | 90.67% / 6.48% | 87.66% / 5.89% |
| *GMM-EM* | 90.45% / 13.8% | 84.74% / 13.44% |

Table 5.2: Unsupervised classification rates as assessed on the ORCADES dataset (70 images) in zone B (802 vessels) and in extended zone ($1,207$ vessels) w.r.t. the manual annotations of observer 1. *C* and *Un* stands for the percentage of correctly classified and unclassified vessels.

The performance measures were computed w.r.t. the labels of observer 1 and are given in Table 5.3 which shows that the sensitivity was $0.8102$ for arteries and $0.7432$ for veins. This implies that the probability of an incorrect classification was $18.98\%$ for arteries and $25.68\%$ for veins.

| Performance Measure | Arteries | Veins |
|---|---|---|
| *Sensitivity* | 0.8102 | 0.7432 |
| *Specificity* | 0.8811 | 0.9491 |
| *Positive Predicted value* | 0.8883 | 0.9259 |
| *Negative Predicted value* | 0.7990 | 0.8119 |
| *Positive Likelihood Ratio* | 6.8129 | 14.594 |
| *Negative Likelihood Ratio* | 0.2154 | 0.2705 |
| *Classification Accuracy* | 0.8429 | 0.8541 |
| *Classification Error rate* | 0.1571 | 0.1459 |

Table 5.3: Classification performance as assessed w.r.t. observer 1 using GMM-EM on the ORCADES dataset (70 images; 802 vessels).

Figure 5.1 shows an example of an image with resulting vessel categorisation using a quadrant-pairwise GMM-EM classification approach with 4 fixed features.

Results obtained through vessel classification using GMM-EM in zone B of the INSPIRE-AVR dataset (483 vessels from 40 images) and the DRIVE dataset

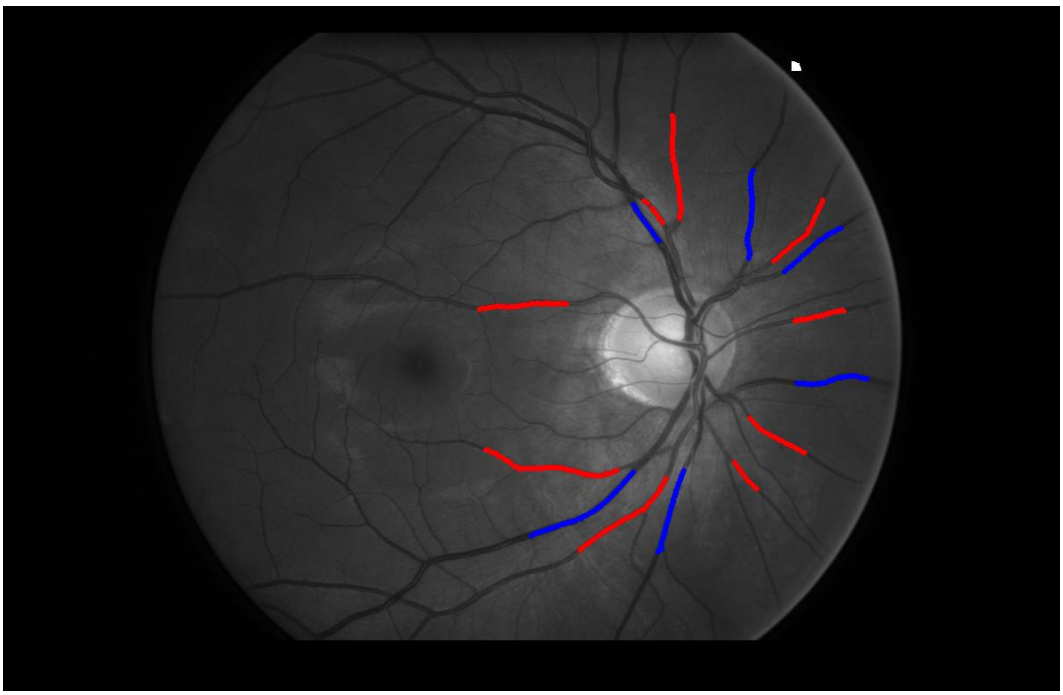

Figure 5.1: ORCADES image showing the classification output using GMM-EM in zone B. Vessels highlighted in red and blue have been classified *arteriole* and *venule*, respectively

(171 vessels from 20 images) are summarised in Table 5.4. With GMM-EM a very high percentage of vessels remained unclassified, especially for the DRIVE images.

| **Classifier** | **INSPIRE-AVR** | **DRIVE** |
|---|---|---|
| | **C/Un%** | **C/Un%** |
| *GMM-EM* | 83.67% / 14 % | 78.1% / 38.6% |
| *SMIC* | 87.6% / 3.83% | 86.2% / 7% |

Table 5.4: Unsupervised classification rates as assessed on the INSPIRE-AVR dataset (40 images; 483 vessels) and the DRIVE test dataset (20 images; 171 vessels) in zone B w.r.t observer 1. *C* and *Un* stands for the percentage of correctly classified and unclassified vessels.

2. **SMIC**

Table 5.2 summarises the results obtained with SMIC on the ORCADES images using only 4 colour features (*MR*, *MG*, *MH* and *VR* ) in zone B (802 vessels)

and in an extended zone ($1,207$ vessels). In zone B the classification accuracy obtained with SMIC and GMM-EM were approximately the same but the percentage of unclassified vessels with GMM-EM was almost double compared to SMIC. In the extended zone the classification accuracy obtained with SMIC was higher and unclassified vessels were lower as compared to GMM-EM.

Results obtained using SMIC in zone B on the INSPIRE-AVR and DRIVE test datasets are summarised in Table 5.4. It can be seen that SMIC outperforms GMM-EM in terms of classification rate and percentage of unclassified vessels. Table 5.5 provides the performance parameters obtained with SMIC w.r.t. the labels of observer $1$ in zone B. Table 5.5 shows that the classification accuracy is higher and classification error rate is lower with SMIC as compared to GMM-EM.

| **Performance Measure** | **Arteries** | **Veins** |
|---|---|---|
| *Sensitivity* | 0.9514 | 0.7270 |
| *Specificity* | 0.8351 | 0.9792 |
| *Positive Predicted value* | 0.8708 | 0.9676 |
| *Negative Predicted value* | 0.9364 | 0.8073 |
| *Positive Likelihood Ratio* | 5.777 | 34.8973 |
| *Negative Likelihood Ratio* | 0.0582 | 0.2788 |
| *Classification Accuracy* | 0.8978 | 0.8628 |
| *Classification Error rate* | 0.1022 | 0.1372 |

Table 5.5: Classification performance as assessed w.r.t. observer $1$ using SMIC on the ORCADES dataset ($70$ images; $802$ vessels.)

Table 5.6 shows the result obtained after attempting to reduce the number of unclassified vessels (see section 4.4 for details). Comparing these results to those in Table 5.2 shows that the percentage of unclassified vessels were indeed reduced.

Figure 5.2 shows an example of classification result obtained after attempting to classify the unclassified vessels. Image in Figure 5.2 shows that there were two

vessels which remain unlabelled in an experiment using SMIC and are marked *Noise* in an image. Vessels marked in red and blue are *arteriole* and *venule* labels respectively assigned to unlabelled *Noise* vessels after applying the technique for classifying unlabeled vessels.

| **Classifier** | **Zone B** | **Extended Zone** |
|---|---|---|
| | **C/Un%** | **C/Un%** |
| *SMIC* | 90.62% / 2.99% | 87.78% / 2.23% |
| *GMM-EM* | 90.8% / 4.98% | 85.95% / 4.47% |

Table 5.6: Classification rate as assessed on the ORCADES dataset after reducing the number of unclassified vessels using the method described in section 4.4. *C* and *Un* stands for the percentage of correctly classified and unclassified vessels.

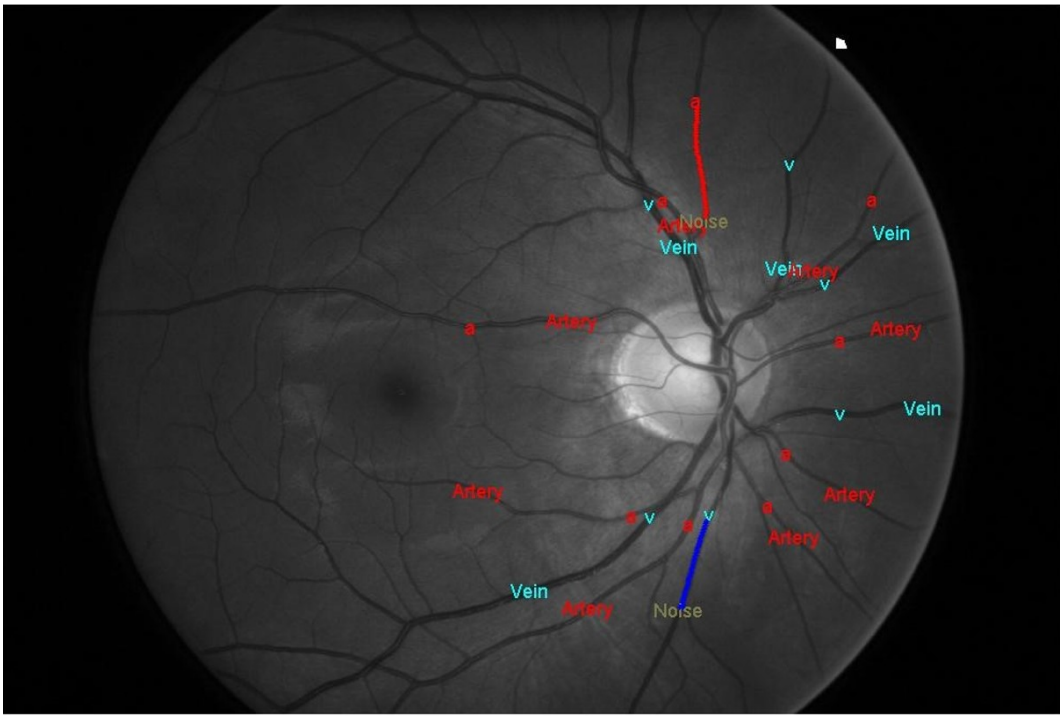


Figure 5.2: Image showing vessel classification result after attempting to classify two unclassified vessels. Vessels marked with *v* and *a* indicates ground truth (generated by observer 1) of *venule* and *arterioles* respectively. Vessels marked with *Vein* and *Artery* are the SMIC classification outcome. *Noise* marked vessels are those that remained unlabelled during classification. Vessels marked *Noise* were assigned label *arteriole* and *venule* highlighted in red and blue respectively after applying technique for classifying unlabelled vessels.

### 5.2.3 Supervised Classification

Table 5.7 summarises the results w.r.t observer $1$ using LS-SVM in zone B and in the extended zone with two experiments, i.e. Exp$5$ and Exp$10$. *C* is the percentage of correctly classified vessels and *Un* stands for the unclassified vessels. The classification accuracies obtained in Exp$10$ and Exp$5$ were very similar for both zone B and the extended zone.

| **Classifier** | **Zone B** | **Extended Zone** |
|---|---|---|
| | **C/Un%** | **C/Un%** |
| *LS-SVM Exp10* | 94.88% /0.58% | 93.96%/ 0.29% |
| *LS-SVM Exp5* | 94.16% / 0.29% | 93.95% /0.48% |

Table 5.7: Classification rate using LS-SVM as assessed on the ORCADES dataset w.r.t. observer $1$. *C* and *Un* stands for the percentage of correctly classified and unclassified vessels.

Increasing the number of training images to 15 or 20 gave very similar results but with longer training times (from just under 3 minutes to over an hour; refer section 5.4 for details regarding computer processing power) as compared to training with 5 or 10 images (less than 5s). Thus, the proposed system performed well and gave very good results, even with a small set of training images and a short training time.

When the experimental protocol for Exp$10$ was repeated five times (Exp$10_5$) (with a random selection of training images each time), a mean classification accuracy (and standard deviation (std.)) of $94.04\%$ $(0.93\%)$ and $94.31\%$ $(0.83\%)$ was achieved in zone B and the extended zone, respectively, (see Table 5.8). Whereas for Exp$5_5$, the mean (std.) classification accuracy from five repeats was $94\%(\sim 1\%)$ and $93.9\%$ $(0.81\%)$ in zone B and the extended zone. See Table 5.8. These mean classification results were very close to those results in Table 5.7.

The performance measures described in section 4.3.6 were calculated for

| Experiment | Zone B | Extended Zone |
|---|---|---|
| | **Mean / Std.** | **Mean / Std.** |
| $Exp10_5$ | 94.04% /0.93% | 94.31% / 0.83% |
| $Exp5_5$ | 94.07% / 1.08% | 93.9% /0.81% |

Table 5.8: Mean (and std.) classification rates when the experiments were repeated five times (with a random choice of training images) using LS-SVM on the ORCADES dataset w.r.t observer $1$.

LS-SVM (w.r.t. observer $1$'s labels) for Exp$10$ and Exp$5$ in the extended zone. See Tables 5.9 and 5.10. For Exp$10$, sensitivity was found to be $0.969$ for arterioles and $0.908$ for venules, which means that the probability of incorrect classification was only $3.1\%$ for arterioles and $9.1\%$ for venules. Similarly, the classification accuracy obtained for Exp$5$ in the extended zone for arterioles and venules was $93.7\%$ and $93.8\%$, respectively, which was very similar to the performance of Exp$10$. Overall, the classification accuracy for both arterioles and venules was very high in all the experiments and confirmed the high reliability of the proposed system.

| Performance Measure | Arteries | Veins |
|---|---|---|
| *Sensitivity* | 0.9689 | 0.9088 |
| *Specificity* | 0.9142 | 0.9689 |
| *Positive Predicted value* | 0.9087 | 0.9708 |
| *Negative Predicted value* | 0.9709 | 0.9035 |
| *Positive Likelihood Ratio* | 11.2975 | 29.2620 |
| *Negative Likelihood Ratio* | 0.0340 | 0.0942 |
| *Classification Accuracy* | 0.9399 | 0.9370 |
| *Classification Error rate* | 0.0601 | 0.0630 |

Table 5.9: Classification performance for Exp$10$ as assessed w.r.t observer $1$ and conducted in the extended zone using the ORCADES dataset ($70$ images; $1,207$ vessels).

| Performance Measure | Arteries | Veins |
|---|---|---|
| *Sensitivity* | 0.9545 | 0.9179 |
| *Specificity* | 0.9215 | 0.9607 |
| *Positive Predicted value* | 0.9147 | 0.9636 |
| *Negative Predicted value* | 0.9583 | 0.9116 |
| *Positive Likelihood Ratio* | 12.1637 | 23.3336 |
| *Negative Likelihood Ratio* | 0.0494 | 0.0855 |
| *Classification Accuracy* | 0.937 | 0.9379 |
| *Classification Error rate* | 0.063 | 0.0621 |

Table 5.10: Classification performance for Exp$5$ as assessed w.r.t observer $1$ and conducted in the extended zone using the ORCADES ($70$ images; $1,207$ vessels).

When the classifier was trained with the vessels in the extended zone and tested on vessels in zone B, a classification accuracy of $93.7\%$ was obtained. This was slightly less than when the system was trained with data obtained from zone B. In another experiment using DRIVE dataset on $171$ vessels extracted from $20$ test images in zone B, the resulting classification rate was $89.4\%$. The LS-SVM classifier was trained with $20$ training DRIVE images.

### 5.2.4 Dimensionality Reduction

The ORCADES dataset ($802$ vessels from zone B) was used to assess the vessel classification performance of dimensionality reduction methods in conjunction with GMM-EM. Table 5.11 presents the rate of correct classification (*C*) and unclassified vessels (*UN*) obtained with GMM-EM using dominant features predicted by each respective method (i.e. PCA, OLPP, MICI and LS). The mean and std. of the classification results (w.r.t. observer $1$) obtained at lower ($9-15$ features) and higher ($32-47$ features) dimensions were also calculated and mentioned in the Table 5.11.

It was observed during the experiments that the classification result obtained with

LS and MICI varies for different number of features chosen. Experiment using LS and MICI (as explained in item 3 of section 4.3.7) was conducted by choosing different number of features each time for vessel classification. Table 5.11 shows classification results using LS and MICI method for which classification rate obtained was maximum when optimal number of features were chosen by dimensionality reduction technique (see item 3 of section 4.3.7). Table also indicates the results obtained with PCA when the three principle components were used for vessel classification. Whereas, results obtained with OLPP are also indicated when Eigen vectors corresponding to Eigen values greater than and equal to $0.9$ (at lower dimensions i.e. for the $9, 12$ and $15$ features in the feature set) and $0.95$ (at higher dimensions i.e. for the $32, 37, 42$ and $47$ features in the feature set) were used (see section 3 of section 4.3.7).

Fig. 5.3 shows a graphical representation of the results in Table 5.11. 9B, 9H and 9V represent the features set with 9 features extracted from **B**lue, **H**ue and **V**alue colour space, respectively along with that extracted from green and red colour space in each set (see Table 4.2). As seen from Table 5.11 and Fig. 5.3, classification performance using MICI and LS deteriorated at higher dimensions. In lower dimensions ($9 - 15$ features) as well as in higher dimension ($32 - 47$ features), the rate of correct classification using both MICI and LS was lower than that of OLPP. The difference in mean classification rate obtained by MICI in lower and higher dimension w.r.t. OLPP was $1.03\%$ and $3.91\%$, respectively. Similarly, the difference in mean classification rate obtained by LS w.r.t. OLPP in lower and higher dimensions was $1.96\%$ and $3.18\%$, respectively.

Moreover, the percentage of unclassified vessels with MICI and LS was higher compared to OLPP. Therefore OLPP yielded a higher rate of correct classification and a lower number of unclassified vessels compared to the other feature selection methods. At the same time, the difference in mean classification rate obtained by MICI in lower and higher dimension w.r.t. PCA was $-0.15\%$ and $2.67\%$, respectively. This demonstrated little difference in mean classification rate at lower dimension between PCA and MICI, whereas in higher dimensions PCA performed better than MICI.

OLPP gave a lower number of unclassified vessels than PCA in both lower and higher feature dimensions. The difference in the mean classification rate between OLPP and PCA was 1.18% in lower dimensions and 0.88% in the higher dimensions. OLPP performed better for retinal vessel classification in both lower and higher dimensional feature sets in terms of classification rate and number of unclassified vessels compared to PCA and the other feature selection methods.

| | Features | OLPP | | PCA | | MICI | | LS | |
|---|---|---|---|---|---|---|---|---|---|
| | | C% | UN% | C% | UN% | C% | UN% | C% | UN% |
| 9 | GRB | 91.1 | 8.73 | 90.2 | 12.1 | 90.63 | 12.2 | 89.6 | 11.1 |
| | GRH | 91.4 | 11 | 89.08 | 12.1 | 89.73 | 12.6 | 89.02 | 9.1 |
| | GRV | 91.4 | 11.59 | 91.49 | 14.96 | 89 | 10.47 | 90.18 | 9.85 |
| 12 | GRBH | 90.67 | 10.72 | 88.5 | 12.8 | 90.8 | 10.47 | 88.1 | 9.98 |
| 15 | GRBHV | 91.13 | 11.5 | 90.56 | 14.1 | 90.4 | 10.47 | 89 | 11.1 |
| | **Mean (9-15 features)** | **91.14** | **10.7** | **89.96** | **13.2** | **90.11** | **11.24** | **89.18** | **10.26** |
| | **Std. (9-15 features)** | **0.26** | **1.16** | **1.27** | **1.27** | **0.66** | **1.07** | **0.69** | **0.86** |
| 32 | GRBHVL Contrast: GR | 90.1 | 9.2 | 89.64 | 9.72 | 83.5 | 13 | 83.28 | 14.2 |
| 37 | GRBHVLGy Contrast: GR | 90.21 | 10.85 | 88.87 | 8.1 | 83.69 | 12.1 | 85.07 | 13.09 |
| 42 | GRBHVL Profile: GR Contrast: GR | 90.4 | 8.98 | 90.1 | 8.97 | 83.74 | 14.1 | 88.73 | 11.47 |
| 47 | GRBHVLGy Profile:GR Contrast:GR | 90.56 | 8.85 | 90.6 | 8.35 | 83.45 | 14.1 | 85.4 | 11.97 |
| | **Mean (9-47 features)** | **90.77** | **10.14** | **89.89** | **11.24** | **87.22** | **12.17** | **87.59** | **11.32** |
| | **Std. (9-47 features)** | **0.49** | **1.22** | **0.96** | **2.54** | **3.5** | **1.46** | **2.39** | **1.61** |

Table 5.11: Classification rates resulting from dimensionality reduction methods (i.e. PCA, OLPP, MICI and LS) using seven feature sets obtained from the ORCADES dataset in conjunction with GMM-EM and w.r.t. observer 1. *C* and *Un* stands for the percentage of correctly classified and unclassified vessels. Mean and standard Deviation (Std.) of *C%* and *Un%* obtained at lower (9-15 features) and higher (32-47 features) dimensions are also mentioned.

From Table 5.11 it can be seen that for $9 - 47$ features in the feature set, OLPP gave the highest mean and lowest std of correct classification rate as compared to all the methods that were tested. Furthermore, OLPP had the lowest mean and lowest std. of percentage of unclassified vessels. Thus, after extensive testing on different features subsets and with different dimensionality reduction techniques, it can be concluded that OLPP gave the best classification rate and with a reduced number of unclassified vessels.

The OLPP (being best dimensionality reduction technique) was also used in conjunction with SMIC classifier with quadrant-pairwise approach with only lower ($9$V) and higher dimension ($32$ and $47$) to classify $802$ vessels from zone B of ORCADES images to further demonstrate the system performance using different classifier. Table 5.12 shows the result obtained and indicates that though the classification rate obtained were similar but number of unclassified vessels reduced to good extent as compared to OLPP technique in conjunction with GMM-EM classifier (see Table 5.11).

| **Features** | **OLPP** | |
|---|---|---|
| | **C%** | **UN%** |
| **9V** | 91.8 | 4.24 |
| **32** | 89.8 | 6.1 |
| **47** | 90.00 | 6.48 |

Table 5.12: Classification rates resulting from OLPP in conjunction with SMIC from the ORCADES image and w.r.t. observer $1$. *C* and *Un* stands for the percentage of correctly classified and unclassified vessels.

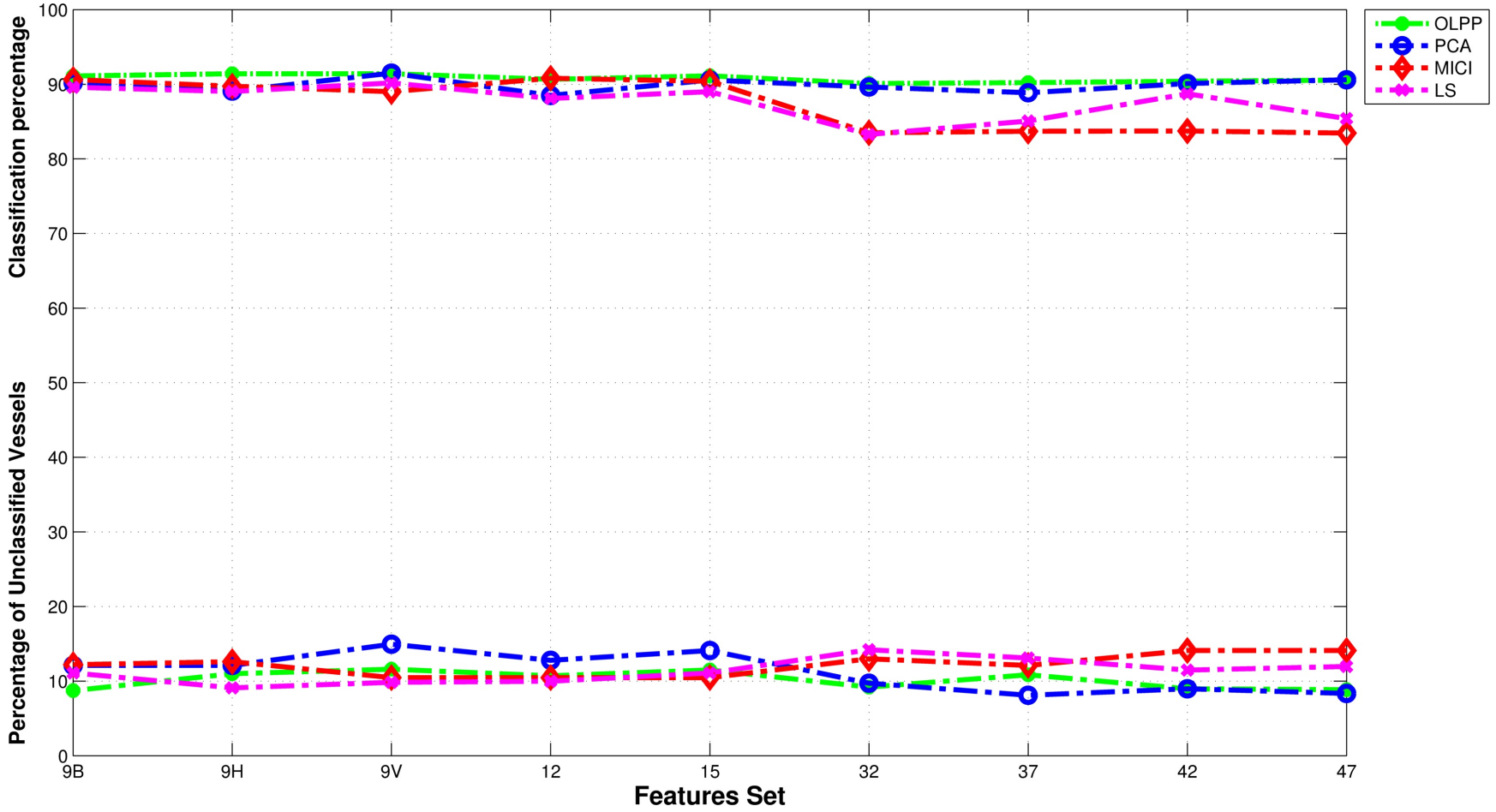


Figure 5.3: Graphical representation of the results in Table 5.11.

## 5.3 AVR Results

Table 5.13 summarises the AVR's measured on the INSPIRE-AVR test dataset as calculated by two observers (Ob1 and Ob2, both of whom were ophthalmologists) and an automatic system (Sys) as reported in [122]. AVR's obtained by Ob1 (author MDA of [122]) were taken as the ground truth while those by Ob2 (AVD of [122]) were used to determine the variability between humans manually repeating AVR measurements. The table also lists the differences (Diff.) between the measurements and has been designed to act as a quick point of reference for results and discussion presented in this thesis. In our analysis we also used Ob1 as ground truth.

After vessel classification, system AVRs were calculated using Knudtson, Goatman and Patton method as explained in the algorithms 1, 2 and 3 respectively, described in section 4.5 and resulting mean, std., min and max of the obtained AVRs is given in APPENDIX A.

Bland-Altman (BA) plot was made between difference and mean of AVR measurements. BA plots indicates the bias which is the mean of the differences between the two measurements (indicated by solid lines in plots). It also indicates the upper and lower limit of agreement (LOA) (indicated by broken lines in plots ) which is the $95\%$ confidence intervals (CI) computed as the (*mean difference* $\pm$ $1.96$**std. of the differences*).

Bland-Altman (BA) plot, shown in Figure 5.4 was made between difference and mean of the manual AVR measurements made by Ob1 and Ob2 of [122] to see the degree of agreement between them. Figure 5.4 indicates that the lower and upper LOA as $(-0.141, 0.154)$ i.e. the width of the LOA is $0.295$ (within $95\%$ CI). In other words, in 95% of the cases mean width of LOA lies in the intervals ($(-0.141, 0.154)$). As seen from BA plot, bias between AVR measurements obtained with Ob1 and Ob2 is $0.0065$ i.e. on average the first method (Ob1) measures $0.0065$ units more than the second one (Ob2). Ideally, LOA should be narrow and mean difference (bias) between

| Images | Ob1 | Sys. | Ob2 | Diff. =Ob1-Ob2 | Diff. =Ob1-sys | Diff. =Ob2-sys |
|---|---|---|---|---|---|---|
| image1 | 0.70 | 0.62 | 0.71 | -0.01 | 0.08 | 0.09 |
| image2 | 0.63 | 0.70 | 0.68 | -0.05 | 0.07 | 0.02 |
| image3 | 0.70 | 0.59 | 0.65 | 0.05 | 0.11 | 0.06 |
| image4 | 0.65 | 0.68 | 0.64 | 0.01 | 0.03 | 0.04 |
| image5 | 0.78 | 0.74 | 0.75 | 0.03 | 0.04 | 0.01 |
| image6 | 0.65 | 0.58 | 0.65 | 0.00 | 0.07 | 0.07 |
| image7 | 0.67 | 0.74 | 0.65 | 0.02 | 0.07 | 0.09 |
| image8 | 0.64 | 0.68 | 0.71 | -0.07 | 0.04 | 0.03 |
| image9 | 0.69 | 0.77 | 0.76 | -0.07 | 0.08 | 0.01 |
| image10 | 0.56 | 0.57 | 0.85 | -0.029 | 0.01 | 0.28 |
| image11 | 0.64 | 0.70 | 0.74 | -0.1 | 0.06 | 0.04 |
| image12 | 0.76 | 0.81 | 0.75 | 0.01 | 0.05 | 0.06 |
| image13 | 0.57 | 0.6 | 0.62 | -0.05 | 0.03 | 0.02 |
| image14 | 0.62 | 0.59 | 0.58 | 0.04 | 0.03 | 0.01 |
| image15 | 0.64 | 0.67 | 0.61 | 0.03 | 0.03 | 0.06 |
| image16 | 0.68 | 0.67 | 0.68 | 0.00 | 0.01 | 0.01 |
| image17 | 0.52 | 0.55 | 0.45 | 0.07 | 0.03 | 0.10 |
| image18 | 0.62 | 0.58 | 0.63 | -0.01 | 0.04 | 0.05 |
| image19 | 0.67 | 0.71 | 0.63 | 0.04 | 0.04 | 0.08 |
| image20 | 0.71 | 0.67 | 0.62 | 0.09 | 0.04 | 0.05 |
| image21 | 0.57 | 0.59 | 0.58 | -0.01 | 0.02 | 0.01 |
| image22 | 0.72 | 0.74 | 0.76 | -0.04 | 0.02 | 0.02 |
| image23 | 0.66 | 0.81 | 0.69 | -0.03 | 0.15 | 0.12 |
| image24 | 0.65 | 0.63 | 0.64 | 0.01 | 0.02 | 0.01 |
| image25 | 0.56 | 0.69 | 0.49 | 0.07 | 0.13 | 0.20 |
| image26 | 0.73 | 0.60 | 0.61 | 0.12 | 0.13 | 0.01 |
| image27 | 0.64 | 0.66 | 0.63 | 0.01 | 0.02 | 0.03 |
| image28 | 0.63 | 0.61 | 0.68 | -0.05 | 0.02 | 0.07 |
| image29 | 0.72 | 0.68 | 0.70 | 0.02 | 0.04 | 0.02 |
| image30 | 0.59 | 0.61 | 0.61 | -0.02 | 0.02 | 0 |
| image31 | 0.75 | 0.76 | 0.75 | 0.00 | 0.01 | 0.01 |
| image32 | 0.53 | 0.59 | 0.61 | -0.08 | 0.06 | 0.02 |
| image33 | 0.61 | 0.71 | 0.59 | 0.02 | 0.10 | 0.12 |
| image34 | 0.65 | 0.68 | 0.61 | 0.04 | 0.03 | 0.07 |
| image35 | 0.74 | 0.59 | 0.64 | 0.10 | 0.15 | 0.05 |
| image36 | 0.69 | 0.64 | 0.62 | 0.07 | 0.05 | 0.02 |
| image37 | 0.82 | 0.72 | 0.79 | 0.03 | 0.10 | 0.07 |
| image38 | 0.93 | 0.80 | 0.76 | 0.17 | 0.13 | 0.04 |
| image39 | 0.61 | 0.70 | 0.64 | -0.03 | 0.09 | 0.06 |
| image40 | 0.74 | 0.81 | 0.62 | 0.12 | 0.07 | 0.19 |
| mean | 0.666 | 0.671 | 0.660 | 0.0065 | 0.058 | 0.058 |
| std | 0.080 | 0.073 | 0.077 | 0.0755 | 0.040 | 0.058 |
| min | 0.52 | 0.55 | 0.45 | -0.29 | 0.01 | 0 |
| max | 0.93 | 0.81 | 0.85 | 0.17 | 0.15 | 0.28 |

Table 5.13: AVR measurements performed on images from the INSPIRE-AVR test dataset [192]. Ob1 denotes the measurements performed by the first observer, and was taken as the ground truth. Ob2 are the measurements from the second observer while Sys. are from the automatic system [122]. Also presented are the differences between the observer readings and the automatic system. Mean, standard deviation (std.), minimum (min) and maximum (max) of AVR values are also mentioned.

measurement should be zero. From Figure 5.4 it was observed that LOA between two observers is narrow and bias is negligibly low therefore the measurement between two observers are essentially equivalent and shows the high degree of agreement between them. The Student's paired t-test showed that there was no significant difference between the Ob1 and Ob2 (p = 0.59). Therefore, based on these observation, in subsequent part of this chapter, results are given w.r.t. Ob1. Moreover, the results obtained w.r.t Ob2 are discussed in APPENDIX A.

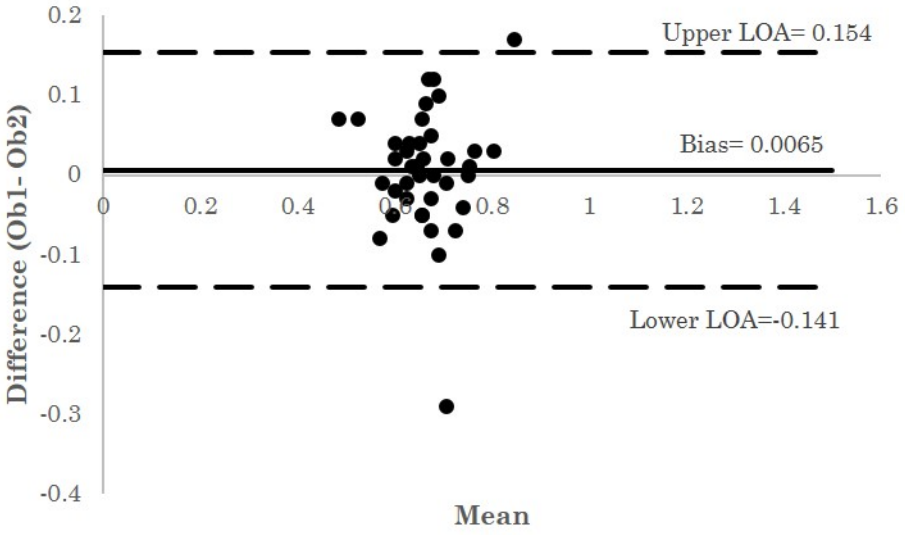


Figure 5.4: Bland-Altman plots between difference and mean of manual measurement of AVR by Ob1 and Ob2 of [122] for INSPIRE-AVR dataset [192]

BA plots (shown in Figures 5.5, 5.6 and 5.7) were also made to examine the difference between two measurements (AVR measurement by Knudtson, Goatman and Patton method w.r.t Ob1) as a function of their average of each sample. Figure 5.5(a) shows LOA as $(-0.128, 0.407)$ i.e. the width of the LOA is $0.535$ for Knudtson AVR measurement w.r.t. Ob1 when vessel classification was obtained with GMM-EM. Whereas, the width of the LOA is $0.532$ for Goatman AVR measurement w.r.t. Ob1 (for GMM-EM). LOA does not vary much when AVR measurement was performed with Knudtson and Goatman methods w.r.t. Ob1 in all the cases (see Figure 5.5, 5.6 and 5.7).

The bias between AVR obtained with Knudtson and Ob1 with GMM-EM is $0.139$ where as that obtained with Goatman is $0.142$. It was observed that bias also

does not vary much with Knudtson and Goatman methods w.r.t. Ob1 in all the cases (see Figure 5.5, 5.6 and 5.7). Figure 5.5(a) shows that the bias obtained by Patton method was less than that obtained with Knudtson and Goatman method for GMM-EM while it is more for SMIC and OLPP method (Figure 5.6 and 5.7).

The Student's paired t-test was performed between the ground truth standard and the system's measurements (when the AVRs were obtained from vessels classified using GMM-EM classifier) and it showed that there was a significant difference ($p < 0.001$) for Knudtson, Goatman and Patton method.

The Student's paired t-test was also performed between the ground truth standard and the AVRs obtained from Knudtson, Goatman and Patton method when vessels were classified using SMIC and OLPP+GMM-EM approach and it also showed the significant difference ($p < 0.001$).

Moreover, Student's t-test was also performed between the ground truth AVR and the AVR calculated from the vessels manually annotated (*arterioles* or *venules*) by observer 1 (author DR). T-test also shows that there was a significant difference between the two ($p < 0.001$).

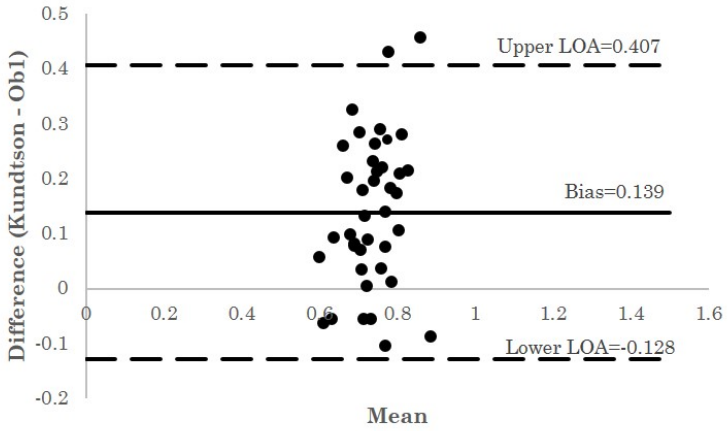


(a)

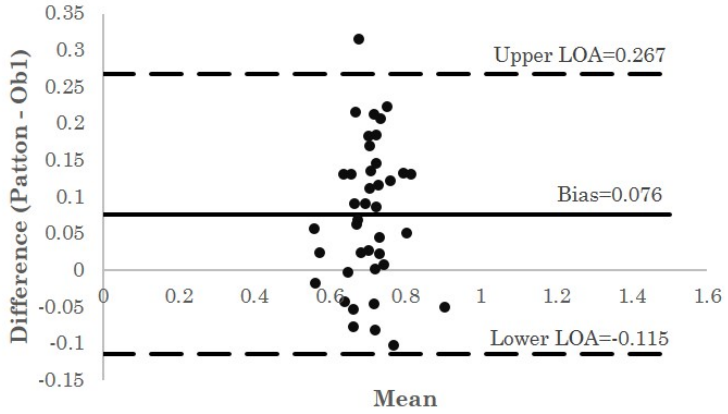


(b)

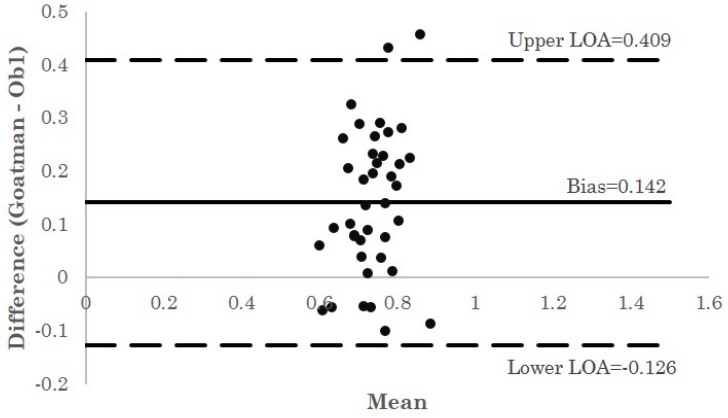


(c)

Figure 5.5: Bland-Altman plots between difference and mean of the AVRs calculated by algorithms of Knudtson, Goatman and Patton method as describe in 1, 2 and 3 respectively in section 4.5 and Ob1. Results were obtained when vessels extracted from INSPIRE-AVR images [192] were classified using GMM-EM classifier.

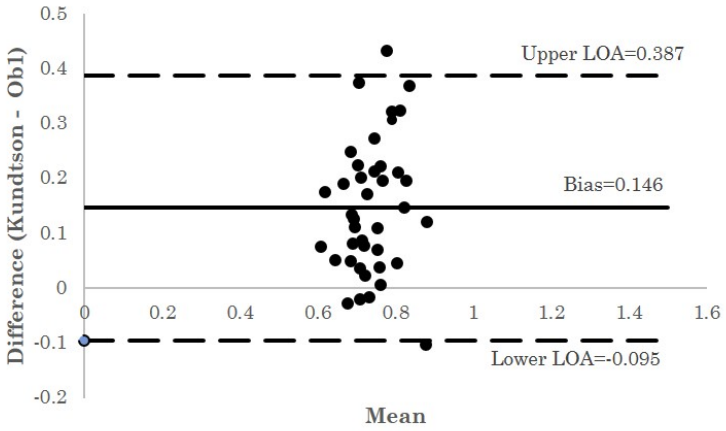


(a)

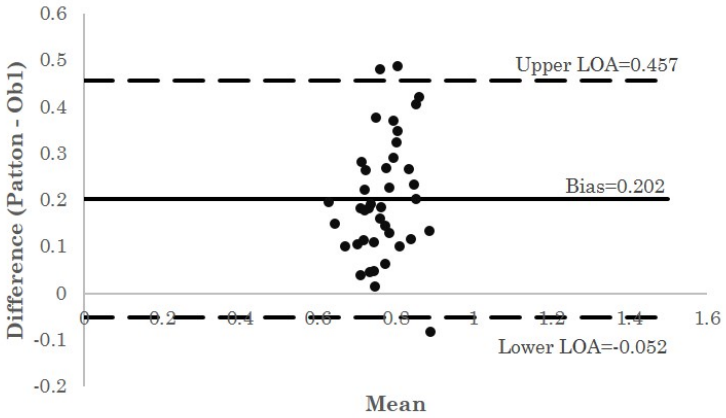


(b)

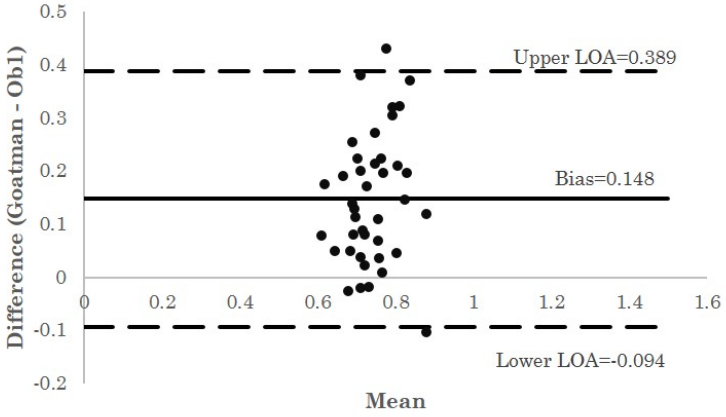


(c)

Figure 5.6: Bland-Altman plots between difference and mean of the AVRs calculated by algorithms of Knudtson, Goatman and Patton method as describe in 1, 2 and 3 respectively in section 4.5 and Ob1. Results were obtained when vessels extracted from INSPIRE-AVR images [192] were classified using SMIC classifier.

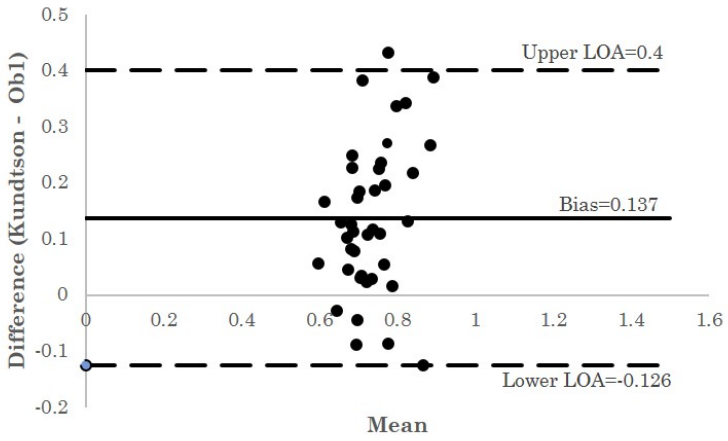


(a)

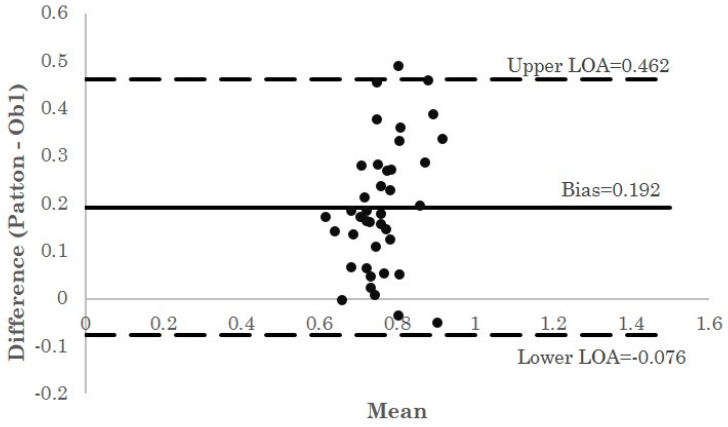


(b)

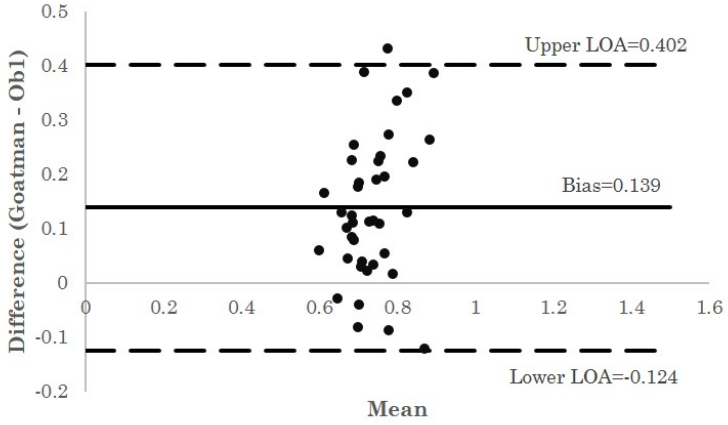


(c)

Figure 5.7: Bland-Altman plots between difference and mean of the AVRs calculated by algorithms of Knudtson, Goatman and Patton method as describe in 1, 2 and 3 respectively in section 4.5 and Ob1. Results were obtained when vessels extracted from INSPIRE-AVR images [192] were classified using OLPP in conjunction with GMM-EM classifier.

## 5.4 Discussion

It is vital to include a computerised classification framework, with high sensitivity and specificity, in any system designed for the (semi-) automatic analysis of large image datasets [12] [52]. The use of GMM-EM, SMIC and LS-SVM to classify retinal vessels into arterioles and venules is reported in this thesis for the first time (to the best of knowledge). In addition, a novel quadrant pair wise approach to retinal vessel classification has also been proposed that does not require the presence of at least one artery and one vein per quadrant and is applicable even when there is no vessel in a quadrant, both limitations of previously reported systems [70].

Testing of unsupervised vessel classification using GMM-EM with $4$ colour features on $70$ images showed a low false positive rate for veins and arteries, i.e. (1-specificity) of $0.05$ and $0.119$ compared to $0.208$ and $0.108$ reported in [117]. The system proposed here resulted in positive likelihood ratio of $(14.59, 6.813)$ and negative likelihood ratio of $(0.2705, 0.2154)$ as compared to positive likelihood ratio of $(4.2218, 7.2386)$ and negative likelihood ratio of $(0.1528, 0.2445)$ for (veins, arteries) reported in [117]. Likelihood ratios were higher, which confirmed the high reliability of the proposed method. The precision (positive predicted value) from the methods presented in this thesis were all higher than 0.8802 (for arteries) and $0.8118$ (for veins) which was reported in [117]. Also, the percentage of correct classification by the proposed system was higher when compared to $87.6\%$, $90.08\%$, and $88.28\%$ reported in [70], [118] and [121], respectively. Results were slightly higher when compared with observer $2$, who was a more experienced imaging scientist.

The results obtained with using SMIC were very promising in both zone B and in the extended zone. The performance of SMIC was better than that of the GMM-EM unsupervised classifier both in terms of classification rate and unclassified vessels. The classification percentage obtained by the proposed system was higher than those reported in [70] [117] [118] [121]. $70$ colour fundus images in the ORCADES dataset were analysed for this thesis compared to $58$, $35$ and $15$ images analysed in [70] [118]

[121], respectively. The performance of the proposed system using SMIC was further established on the INSPIRE-AVR and DRIVE datasets which yielded classification rates of $87.6\%$ and $86.2\%$, respectively, which was higher than that obtained with GMM-EM. The system also resulted in a higher classification rate on INSPIRE-AVR when compared to [122] (ROC curve = 0.84) and close to that reported in [51] ($87.9\%$ when centreline pixels inside ROI with vessel calibre $> 5$ pixels were considered). Results obtained with [51] were higher when centreline pixels of vessels inside ROI having calibre $> 10, 15$ and $20$ pixels were considered. On the DRIVE images the results obtained were close to that of [51] ($87.4\%$) and lower than that of [6] ($90.16\%$). However, it should be noted that the results in [122] [6] [51] were from supervised techniques while the proposed system here was unsupervised.

Extracting large numbers of features can take a significant amount of computational time. For this research, processing was done on a PC with $8$ GB RAM, $64$ bit Windows $7$ operating system and a $2.83$ GHz processor. With this computing facility, the average time take for background illumination correction was approximately $120$ seconds for each colour channel. Thus, correcting $7$ channels to extract $47$ features required approximately $840$ seconds of processing time. In addition, further computational time is necessary for extraction of ROI based, profile-based and contrast features. Therefore, classification with higher dimensional feature sets is computationally very expensive. Hence the reduction of feature dimension for faster processing of large image datasets is desirable.

OLPP with GMM performs exceptionally well both for small ($9$ to $15$) and large ($32$ to $47$) sets of features. The dimensionality of the feature set does not affect vessel classification accuracy. Moreover, in previous studies OLPP showed promising results. In [180], the authors experimented with OLPP and Locality Preserving Indexing (LPI) with different dimensionality ($1$ to $20$) and with different numbers of clusters, ranging from $2$ to $10$. They showed that both LPI and OLPP reach their best performance at very low dimensionality and also that the performance of LPI decreases drastically but the performance of OLPP fluctuates slightly and is always above the performance of the baseline (results obtained when K-mean was considered as baseline in their study).

In a study on face recognition [193], it was demonstrated that OLPP outperforms other tested method (LPP, LDA, PCA, Gabor- LPP, Gabor-LDA and Gabor-PCA) with two different datasets. In another paper [194] based on a speech recognition experiment using a Persian speech database, it was shown that OLPP based feature transformation has the power to preserve local properties of feature vectors in the projected space and has the best performance as compared to some common transformation methods such as LPP, HLDA and LDA.

Generally, extracting large numbers of features for selecting discriminant features and the labelling vessels manually to generate large training datasets for supervised classification are very time consuming tasks. A supervised classification method such as SVM with a high degree of accuracy has been widely used in classification [122] [33] [6] [35] [123] [124] but the major drawback is its higher computational burden for the constrained optimisation programming as the constrained optimisation optimises an objective function w.r.t. some variables in the presence of constraints on those variables. In order to overcome the drawbacks, the use of the least squares support vector machine (LS-SVM), supervised classifier was proposed, which solves linear equations instead of a quadratic programming problem. Also, the solution procedure of LS-SVM is highly efficient [195]. The results obtained were promising even when only four features were used to train a small set of data. The proposed system showed a high classification rate even with $5$ randomly selected training images as compared to the results reported in [122] [34] [124] [6] which uses $20$ training images. The thesis system had high classification accuracy both for veins and arteries. The result obtained by the proposed method in zone B were also higher than that reported in [122] [6] [123] [124] [34] and [51]. Moreover true positive rates for both arteries and veins were comparable with the method proposed in [35] for $251$ vessel segments.

Classification using LS-SVM on the DRIVE dataset performed well and produced a classification rate ($89.4\%$) that compared favourable to $87.4\%$ reported by Dashtbozorg et al. [51], $90.16\%$ by Mirsharif et al. [6] and $0.88$ (on ROC curve) from M. Niemeijer et al. [34]. The performance of LS-SVM was also found to be better (in

general) than that of the unsupervised classifiers GMM-EM and SMIC.

A degree of caution should, however, be exerted in the direct comparisons of results obtained with different datasets. The resolution of the ORCADES images used here was $2048 \times 3072$ pixels which was different to $1300 \times 1000$ pixels, $768 \times 576$ pixels and $800 \times 1000$ pixels in [70] [118] and [121], respectively. Also, the classification result is highly dependent on segmentation results. Moreover, choosing a different retinal zone, classifier and framework would likely impact the classification performance. Additional training would likely be required to handle different ethnicity due to differing retinal appearances.

After vessel classification, AVR was calculated for each of the $40$ INSPIRE-AVR dataset images using the Knudtson, Goatman and Patton methods. It was observed that the results obtained with Knudtson and Goatman methods were similar. Student's paired t-test showed a significant difference between ground truth and system's measurements. It should be pointed out that AVR not only depends on the accuracy with which vessel classification is completed but also on the number, choice and width of the vessels been examined. As the student's t-test between the ground truth AVR and AVR calculated from manually annotated vessels by observer $1$ showed the significant difference between the two, it can be concluded that the system classification output might not be the reason or cause of the difference between the ground truth AVR and system AVR. Moreover, it should be pointed out that authors of [122] selected $6$ largest retinal arterioles and venules for the calculation of AVR as this corresponds to the AVR formulas described in [127] but in the thesis system, the number of arterioles or venules varies for calculating AVR. Furthermore, the choice of vessels and accuracy with which the vessels width was measured might influence the system AVR measurement.

## 5.5 Conclusions

In this chapter, the vessel classification results using unsupervised and supervised were discussed. Among the unsupervised methods, SMIC outperformed the GMM-EM

approach. Whereas, among all the tested methods supervised approach showed a promising results both in zone B and extended zone and outperforms recently reported systems. It can be inferred from the results obtained from the experiments on different datasets that using only four fixed features for vessel classification lead to more misclassification with a large number of vessels remaining unclassified using an unsupervised classification approach as compared to supervised approach. Thus, this observation is in accordance with the hypothesis that classification rate increases with the help of supervised classifier even with the use of four fixed features. The proposed supervised method required a smaller training datasets compared to other recently reported ones yet it produced similar or higher classification rates. The time require to train the classifier with 5 or 10 training images were less then 5s. The experiment was also conducted to classify vessels with optimal features obtained from dimensionality reduction techniques. Among all the tested dimensionality reduction techniques, it was observed that OLPP is best and promising method to use for vessel classification. Thus, in order to relieve from manual annotation of images (for generating training set) for supervised vessel classification, OLPP (for feature dimensionality reduction) in conjunction with robust unsupervised classifier need to be used.

The final classification system to be use is purely based on whether one can annotate the vessels to generate a small training set or not. If it is possible to generate a training set every time for a new unseen dataset then LS-SVM system is a very promising method to use. Further test with LS-SVM is required where training is performed on one dataset and testing will be performed on another dataset. Furthermore, if the manual annotation is the restriction to generate training set then OLPP in conjuction with robust classifier is a promising method as it can perform well for any feature dimension.

As already discussed, classification is a precursor for the measurement of AVR therefore after vessel classification AVR was calculated using Knudtson, Patton and Goatman method. From the three tested algorithms, Knudtson and Goatman algorithm gave similar results. Though Goatman formula is easier to implement but either of these two method can be used for AVR calculation. Patton algorithm shows lower

bias in conjunction with GMM-EM but shows higher bias with SMIC and with OLPP approach. Based on present experimental result Knudtson or Goatman method performed better and similar. From student's paired t-test it was observed that there was a significant difference between ground truth and system's measurements thus there is a room for improvement. This should be noted that the AVR measurement result is based three main things: the classifier, vessel width measurement system and the choice of vessels to calculate AVR. AVR is highly dependent on how well the classifier classifies vessels and how accurately the vessel width are measured. Also, it is sensitive to the choice of the vessels being made. Moreover, when the labels (*arterioles* or *veins*) generated by observer 1 was used to calculate AVR using three methods, the significant difference between ground truth and system's measurements was still observed. Based on this observation it can be concluded that the present discrepancy in AVR measurement was not due to the classifier result but might be due to the accuracy with which the width of the vessels were measured or the choice of vessels. From this observation it can be concluded that the classification performance has no impact on the AVR measurement.

# Chapter 6

# Fractal Analysis

## 6.1 Introduction

The chapter begins with an introduction to the concept of fractals and is followed by an overview of several techniques for the measurement of fractal dimension in section 6.2. To deal with the problem of calculating the fractal dimension (a potential imaging derived retinal bio-marker of disease) efficiently in large datasets featuring retinal imaging, two different approaches are proposed, Multifractal Fractal Analysis (MFA) and Fourier fractal analysis (FFA). Section 6.3 details the datasets which were used to investigate the potential of fractal analysis to quantify differences in the retinal vasculature from fundus camera imaging. Different procedures of dividing a retinal image to investigate regional differences in vessel patterning in response to disease are discussed in section 6.4. Finally, a summary is given in section 6.5.

## 6.2 Background

### 6.2.1 Concept

The concept of a fractal was proposed by Mandelbrot [196] who introduced the term derived from the Latin word "fractus". According to Mandelbrot a fractal is an irregular geometric object with an infinite nesting of structure at all scales. Fractals are self-similar, which means that structures are repeated at different scales or size. Hence, FD provides a quantitative measure of self-similarity and scaling in an object, structure or image [196] [197].

### 6.2.2 Fractal Dimension

To understand fully the notion of FD, we first need to understand; how we can calculate the FD of an object or pattern. In Euclidean geometry, a line has a dimension of one because there is only one way to move on it. Two-dimensional figures like squares or circles have two directions in which to move, while three-dimensional objects like cubes have three directions. One-dimensional (1D) lines, 2D planes (eg. square) and 3D objects (eg. cube) are all self-similar.

For example, a line segment can be divided into *N* self-similar line segments, each with magnification factor *N*. Similarly, a square can be divided into $4$, $9$ or $25$ self-similar sub-squares with the magnification factor of $2$, $3$ and $5$, respectively. In general, a square can be divided into $N^2$ self-similar sub-squares, with a magnification factor of *N* of each square to yield the original figure. Similarly, a cube can be broken into $N^3$ self-similar cubes, each with a magnification factor of *N*. Hence, FD can be defined as the exponent of the number of self-similar objects with magnification factor *N* into which an object may be broken [198]. Euclidean objects have integer dimensions, which may not adequately describe the morphology and behaviour of a complex object. Thus, fractals are used to characterise and model complex objects

in nature and also artificial objects [196] [197]. The fractal theory developed by Mandelbrot is based on the work of mathematicians Hausdorff and Besicovitch [199]. The FD of a self-similar object can be defined as [197],

$$FD = \frac{log(\textit{number of self similar pieces})}{log(\textit{magnification factor})}. \tag{6.1}$$

According to above definition, a straight line has a dimension of exactly one whereas a fractal curve (e.g., a Koch curve or a Sierpinski triangle) may have a dimension between one and two. That is, a fractal curve has FD between that of a straight line and a plane ($1 <$ FD $< 2$), while a fractal surface has FD between that of a plane and three-dimensional space (3D) ($2 <$ FD $< 3$). FD characterises an object with a dimensionality greater that its topographical dimension. Hence, FD is a non-integer in contrast to objects that lie strictly in Euclidean space [197].

### 6.2.3 Measurement

As mentioned above, the FD of an object, structure or pattern appearing in an image can be defined as the exponent of the number of self-similar pieces, $N_s$, with magnification factor *1/r*, into which an object or image may be broken [197],

$$FD = \frac{ln(\textit{number of self similar pieces})}{ln(\textit{magnification factor})} = \frac{ln(N_s)}{ln(1/r)}. \tag{6.2}$$

There are a variety of methods for measuring the FD such as fractional Brownian motion, Hausdorff-Besicovitch dimension [196] [197] [200] [201] [202], and box-counting, which is a popular and straightforward way to measure fractal complexity [141].

In the box-counting approach of image is covered with sets of squares boxes of decreasing size (r = 512, 256, 128,...1, where r denotes a single pixel). Each set is characterised by the size of the square's edge *r*. The number of squares boxes *N(r)*

necessary to cover the object is presented as a function of *r*, while the number of boxes in which the object or pattern appears is counted. In other words, the number of boxes *N(r)* containing at least one white pixel (skeleton) is counted. Then the box counting dimension, $D_B$ is determined by the absolute value of the slope $S_B$ of [135] [141] [203],

$$S_B = \frac{logN(r)}{log(r)}. \tag{6.3}$$

The value of the least squares regression slope of the plot of $logN(r)$ versus $logr$ yields $D_B$. $D_B$ is often used for fractal calculations for binary structures or signals extracted from data such as coastlines and speech-wave graphs. However, it may not be suitable for more complex patterns found in images such as clouds, rugged textural surfaces, and medical scans [197]. Therefore in the section below, two different alternative methods for calculating FD are introduced.

1. **Multifractal Analysis**

   Multifractal behaviour is often associated with a system where the underlying physics is governed by a random multiplicative process (i.e., successive division of a measure and its spatial support based on a given rule) [204]. It implies that a statistically self-similar measure can be represented as a combination of interwoven fractal dimensions with corresponding scaling exponents [28] [204] [205] [206]. Highly inhomogeneous and complex systems may consist of several intertwined fractal sets with a spectrum of fractal dimensions and such system normally do not obey self-similar scaling law with a single exponent. Such systems are said to be multifractal [207]. In contrast to simple or monofractals measures like $D_B$, multifractal are usually characterised by a hierarchy of exponents rather than a single fractal dimension. A method to calculate the multifractal spectrum $f(\alpha)$ is as follows [204] [206].

   Multifractal sets can be characterised on the basis of the generalised dimensions

of the $q^{th}$ moment orders of a distribution, $D_q$, defined as,

$$D_q = \frac{1}{q-1} \lim_{\epsilon \to 0} \frac{log \sum_i p_i(\epsilon)}{log(\epsilon)}. \tag{6.4}$$

The $D_q$ value at $q = 0$, $D_0$, is called the *capacity dimension* or the *box counting dimension*. With the value at $q = 1$, $D_1$, referred to as the *information dimension* and provides information about the degree of heterogeneity in the distribution of the measure. $D_2$, at $q = 2$, known as the *correlation dimension*, is associated with the correlation function and quantifies the average distribution density of the measure [204]. For a distribution, with simple scaling (i.e. monofractal), $D_1$ and $D_2$ are both equal to $D_0$. Such a distribution exhibits perfect self-similarity and is homogeneous in nature when $D_0$ = $D_1$ = $D_2$, whereas for multifractal type scaling $D_0$ > $D_1$ > $D_2$ [28] [204]. The $q^{th}$ order normalised probability measures of a variable (also known as the *partition function*), $\mu(q, \epsilon)$, vary with the scale size, $\epsilon$ such that [204] [206],

$$\mu(q, \epsilon) = \frac{[p_i(\epsilon)]^q}{\sum_i [p_i(\epsilon)]^q} \propto (\epsilon / L)^{\tau(q)} \tag{6.5}$$

where $p_i(\epsilon)$ is the probability of a measure in the $i^{th}$ segment of size $\epsilon$ units, calculated by dividing the value of the variable in the segment by the whole support length of $L$ units. $p_i(\epsilon)$ measures the concentration of a variable of interest in a given segment relative to the whole support length. The $\tau(q)$ function in eq.6.5 is 'the mass exponent' term as it relates the probability of mass distribution in a given segment to the size of the segment (scale). The multifractal spectrum, $f(q)$, which is the fractal dimension of the subsets of segments of size $\epsilon$ units with a coarse Hölder exponent of $\alpha$ if calculated to the limit as $\epsilon \to 0$, can be expressed as [204] [206],

$$f(q) = \lim_{\epsilon \to 0} [log(\frac{\epsilon}{L})]^{-1} \sum_i \mu_i(q, \epsilon) log \mu_i(q, \epsilon) \tag{6.6}$$

and the local scaling indices, $\alpha$, are given by [204] [206],

$$\alpha = \lim_{\epsilon \to 0} [log(\frac{\epsilon}{L})]^{-1} \sum_i \mu_i(q, \epsilon) log p_i(q, \epsilon). \tag{6.7}$$

$f(\alpha)$ can also be determined through the Legendre transform of the $\tau(q)$ curve [204] [206],

$$f(\alpha(q)) = q\alpha(q) - \tau(q). \tag{6.8}$$

where,

$$\alpha(q) = \frac{d\tau(q)}{dq}. \tag{6.9}$$

and also,

$$\tau(q) = (q-1)D_q. \tag{6.10}$$

$f(\alpha)$ is usually a single humped function with a maximum at $df(\alpha(q))/d\alpha(q) = 0$ where *q* is the moment order of a distribution. Thus, when $q = 0$, $f_{max}$ is equal to the box-counting dimension or $D_0$.

The steps for multifractal analysis are as follows [204]:

1. Calculate the probability measure, *p*, from a linear distance for a transect or area.
   (a) For each *n* = $2, 4, 8, 16, ...$ until the unit is not dividable. To calculate *p*, sum up the values of all the points in the segment, and divide by the total of all segments, ($p_i(\epsilon) = \frac{m(\epsilon,i)}{M}$), where *i* is the index for $i^{th}$ segment, when the whole transect is divided into *n* segments with a unit length =$\epsilon$(*i*=1, . . . ,*n*); *m*($\epsilon$,*i*) is the sum of measurements at all points in the $i^{th}$ segment of length $\epsilon$; *M* is the total of all points along the transect.
   (b) For different *q* values or statistical moments (e.g., -20 to 20), compute $\mu_i(q, \epsilon)$ using Eq. 6.5.

(i) Calculate:

$$F\alpha(q,\epsilon) = \sum_i \mu_i(q,\epsilon) log p_i(\epsilon) \tag{6.11}$$

(ii) Calculate:

$$FD_q(q,\epsilon) = \frac{1}{q-1} \lim_{\epsilon \to 0} \frac{log \sum_i p_i(\epsilon)}{log(\epsilon)} \tag{6.12}$$

For *q*=1, $D_1$ is calculated at (1+$\epsilon$) where $\epsilon$ is very small value equal to 0.001

2. Calculate $\alpha$*(q)* as the intercept of linear regression of *F*$\alpha$*(q,*$\epsilon$*)* vs. log($\epsilon$).
3. Calculate $D_q$ as the intercept of the linear regression of $FD_q$*(q,*$\epsilon$*)* vs. log($\epsilon$).
4. Calculate *f*($\alpha$*)* spectrum using the Legendre transform as in eq. 6.8, 6.9 and 6.10. Where $D_q$ in eq. 6.10 is calculated from eq. 6.4 except for *q=1* where $D_q$ is calculated for *q*+*eps* where *eps*=0.001. The derivatives are calculated as $\frac{d\tau(q)}{dq} \approx$ *(*$\tau(q+eps) - \tau(q)$*)/eps* where $\tau(q+eps)$ = $(q_{eps} - 1) \times D_{q_{eps}}$ , with $q_{eps} \rightarrow$ *q*+*eps* and $D_{q_{eps}}$ is calculated from eq. 6.4 for *q* $\rightarrow$ *q*+*eps*

For an object, the value of $D_q$ at small *q* shows the fractal property of a coarse structure while at large *q* it exhibits the fractal property of a fine structure. For $q \geq 0$, the largest $D_q$ is $D_0$ and $D_q$ decreases with increasing *q*. In other words, largest value is the capacity dimension that is obtained at *q* = 0. The generalised dimensions, $D_q$ as a function of any real *q* and the multifractal spectrum $f(\alpha)$ versus the singularity strength $\alpha$ are shown in Figure 6.1 [208]. The multifractal spectrum has three main properties: the maximum value of $f(\alpha)$ is $D_0$, $f(D_1)$ = $D_1$, and the line joining the origin to the point on the $f(\alpha)$ curve where $\alpha = D_1$ is tangent to the curve [208] [209].

The width of the multifractal spectrum ($\alpha_{max}$-$\alpha_{min}$) is used to examine the heterogeneity in the local scaling indices. The wider the spectrum, the higher the heterogeneity in the distribution of the measure [204].

2. **Fourier Fractal Analysis**

In general, according to [210] the fractal dimension *D* of a set *S* can be expressed

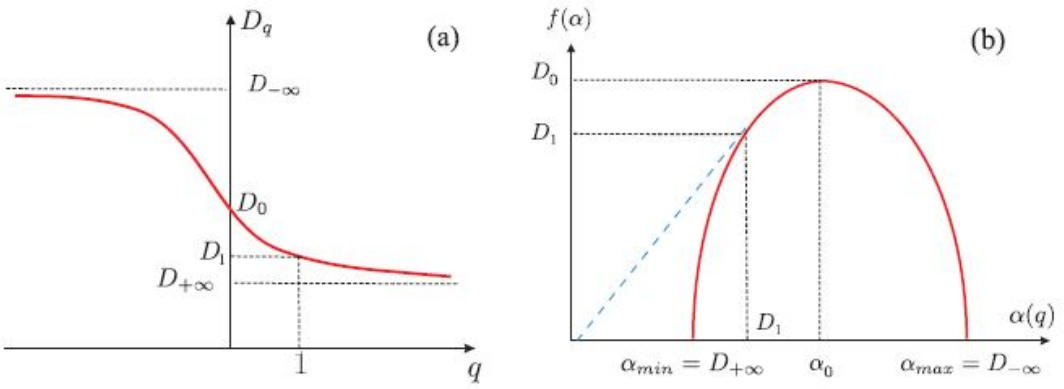


Figure 6.1: (a) The generalised dimensions $D_q$ as a function of any real $q$, $-\infty < q < \infty$, and (b) the singularity multifractal spectrum $f(\alpha)$ versus the singularity strength $\alpha$. Source of this figure: [208]

as,

$$D = \lim_{\delta \to 0} \frac{logM_\delta(S)}{log\delta} \tag{6.13}$$

where *M* is a set measure based on the specifically chosen fractal dimension approach and $\delta$ is the scaling parameter. In the case of an image, the FFD can be calculated from an exponent relation between the power spectrum *P* of the Fourier transform of an image and the frequency variable, *f* [150] [210]. Thus, the measure *M* in eq.6.13 corresponds to the power spectrum *P* and frequency *f* is an analogy of $\delta$. The power law between the power spectrum and frequency is expressed as:

$$P \propto f^{-\alpha} \tag{6.14}$$

where $\alpha$ is the exponentiation parameter related to the *Hurst coefficient* [150]. The fractal dimension is then related to $\alpha$ as,

$$D = \frac{\alpha + 6}{2} \tag{6.15}$$

where $\alpha$ is the slope of the straight line fitting the curve $log(P) \times log(f)$. The main steps involved in the calculation so FFD are described below.

(i) Calculate the Fourier transform of the enhanced image. The Fourier transform of the image function $f(x, y)$ (with $x =$ denoting row index and

$y =$ the column index) of size $N \times N$ pixels can be defined as,

$$F(i,k) = \frac{1}{N^2} \sum_{i=0}^{N-1} \sum_{k=0}^{N-1} f(x,y) e^{-j2\pi \frac{(ix+ky)}{N}}. \tag{6.16}$$

(ii) Calculate the magnitude of the Fourier spectrum of the image as [152],

$$P(i,k) = log(|F(i,k)|^2 + 10^{-6}). \tag{6.17}$$

(iii) Calculate the slope $\alpha$ of $P$ vs. $f$ curve for obtaining the FFD with 6.15.

### 6.2.4 Stroke subtypes: Lacunar vs. Cortical stroke

Stroke is defined as cell death caused by poor blood flow to the brain [211]. There are two main types of stroke: ischaemic and hemorrhagic stroke. Former is caused by interruption of the blood supply to the brain where as later occurs due to bleeding caused by rupture of a blood vessel or an abnormal vascular structure [211].

Strokes can damage brain tissue in the outer structure (the cortex) or deeper part (underneath the cortex) of the brain. Lacunar stroke occur in deep structures of the brain which receive their blood flow through a unique set of arteries. It occurs due to occlusion of one of the penetrating arteries that provides blood to the deep structures of the brain [212]. Whereas, a cortical stroke occurs due to reduced or blocked blood supply to the outer part (cortex) of the brain [213] which results in brain damage.

There are some studies in the past suggesting an associations between retinal changes and lacunar stroke but there is little evidence showing the difference in the retinal vasculature change in ischaemic stroke subtypes [93]. Regional wise fractal analysis was performed on the Edinburgh Mild Stroke dataset (see section 6.3) to find if there is any significant difference between region(s) which can distinguish two stroke subtype: Lacunar stroke and cortical stroke.

### 6.2.5 Stability

It has been shown in earlier studies that FFD found to be relatively insensitive to noise [150] [151] [152]. Thus, in order to test the stability and reliability of fractal analysis, an experiment was conducted in the presence of degrading segmentation quality and noise. MFA was performed by removing junction points and small vessel segments from binary image where as MFA and FFA was performed by introducing noise in an image.

### 6.2.6 Regional Variations

In order to investigate whether changes to the retinal vasculature relating to disease manifest in particular regions of the fundus rather than presenting as a global change an experiment was conducted to divide the fundus image into different sub-regions and conducting fractal analysis in different regions. Different procedures to divide an image into sub-region are discussed in next section.

## 6.3 Material

The image datasets used to test and validate fractal analysis are as follows:

1. **STARE** (STructured Analysis of the REtina)

   This database contains a set of twenty retinal images. From these twenty images, ten had been classified in the database as normal and other ten as pathological. The dataset contain images of patients with different pathological conditions such as diabetic retinopathy, hypertensive retinopathy, central retinal artery and vein occlusion [143]. This particular dataset was chosen because it already contained manual segmentations of the vasculature by two observers (referred to by their initials AH and VK as in [143]), and furthermore the images had

already been classified into two subgroups - *pathological* and *normal*. The images segmented by observers AH and VK differ in level of detail (the images segmented by observer VK demonstrate a substantially higher level of detail) and the resulting set of forty segmented retinal images were used for fractal analysis experiments. These forty segmented images are available for download from the STARE project [143] in ppm file format. This dataset enabled the hypothesis that pathological images will display different fractal properties to the normal ones to be tested. Image resolution of all STARE images is $700 \times 605$ pixels. The images were acquired using a Canon CR5 non-mydriatic 3CCD camera with a $45^\circ$ FoV.

2. **The Edinburgh Mild Stroke Study**

   A bio-resource featuring data from $280$ patients presenting with clinical lacunar or minor cortical stroke who were also recruited for retinal imaging [75]. Out of the $280$ participants, $17$ images had to be excluded due to poor photographic quality. In addition, images from $97$ patients were also excluded due to the following reasons: uncertainty about the diagnosis of stroke, brain imaging showing another non-ischaemic stroke pathology, the stroke was too severe, or the patient declined. This leaves $166$ participants who were grouped into two sets, each consisting of $83$ images for lacunar and cortical sub-types. The analysis was performed on quarter size image with resolution $585 \times 876$ pixels. These images were captured with Canon CR-DGi nonmydriatic retinal camera with $45^\circ$ FoV.

## 6.4 Methodology

Algorithms for fractal analysis were implemented in Matlab (r2013a The Mathworks Inc., USA). To test for a significant difference in fractal properties between the normal and pathological cases as well as between two stroke subtypes, *Student's t-test* was performed and *p-values* were calculated by a two-tailed, heteroscedastic student's t-test

(unpaired, two sample unequal variance t-test). Statistical analysis was performed in MS-Excel.

1. **Pre-processing:** The input image was cropped to the minimum bounding box around the FoV for both MFA and FFA for both datasets. This step avoids analysis of unnecessary portions of the image which contain no pertinent information, increasing computational efficiency and preventing any undue biasing of fractal analysis. This boundary (around the input image) cropping was performed on binary STARE images as the analysis was performed on whole image whereas for Edinburgh mild stroke images the boundary was cropped from green channel as OD information was needed for region wise analysis which was not possible to get directly from the binary image. Once the boundary of green channel of stroke images was cropped the same cropping box dimensions were used to crop the corresponding binary stroke images. The OD was located [94] and OD centre was obtained from cropped green channel of stroke images and this information was used for region based analysis. Figure 6.2 shows an example of stroke image before and after removing the boundary around the segmented retinal image. For the MFA the segmented images were skeletonised using *bwmorph* function in MATLAB, which is based on iterative deletion of pixels [214].

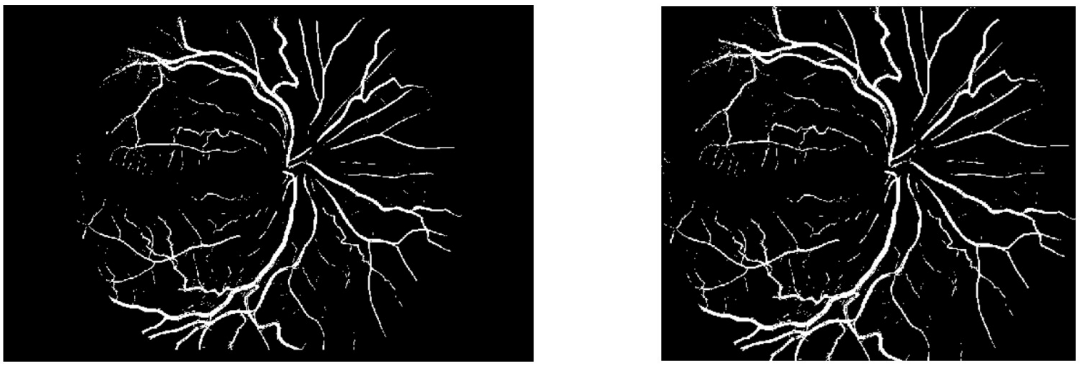

(a) (b)

Figure 6.2: Image from stroke dataset with (a) Full Image and (b) after removing boundary

2. **STARE**

(a) For MFA, the sets of twenty hand segmented images contained in the database were analysed. To investigate the stability of MFA due to variations in the segmentations (which occurs due to the application of different softwares or manual grading by different graders), MFA was performed after removing junction points and small vessel segments (an example of which is shown in Figure 6.3). To remove junctions, an image was first skeletonised using the *bwmorph* function in MATLAB, which is based on iterative deletion of pixels [214]. All junction points in an image were then found [215]. If the OD was on the left of the image (i.e. an image of a left eye) then the junction points to the right of the centre of the image were removed (see Figure 6.3(b) and 6.3(c), and if OD was on the right (i.e. an image of a right eye) then the junction points to the left of the centre of the image were removed. In order to delete vessels segments from a segmented image, first all the junctions to the left (if OD was on right) or right (if OD is in left) of the centre of the image were removed and then the properties for each vessel segments were measured using Matlab's *regionprops* function. The ten largest vessel segments (as defined using the *MajorAxisLength* property) were then removed from the image (see Figure 6.3(d)). MFA was also preformed on skeletonised binary image to test whether fractal analysis may be more sensitive to changes in the vascular patterns in the skeletonised versions. One of the main advantages of performing analysis on skeletonised image is that it contains far lesser number of pixels, hence offers greater advantage in terms of overall computational cost [28].

(b) For FFA the grayscale version and the green channel ($G$) of the colour fundus image were both processed. The conversion of RGB to grayscale ($Gy$) was achieved via $Gy = 0.2989 \times R + 0.5870 \times G + 0.1140 \times B$. The variations in image brightness and contrast can significantly affect the measurement of retinal vascular fractals [216], therefore image contrast was improved using the *imadjust* function in MATLAB before processing

by mapping the intensity values in an image to new values in new image such that 1% of data is saturated at low and high intensities of an image.

(c) MFA and FFA were also performed after artificially introducing noise into an image (using the *imnoise* function in MATLAB) to further examine the stability of FD measurements. This was *salt and pepper* noise in the segmented images for MFA, and *Gaussian*, *salt and pepper* and *Poission* noise added to Gy and green channel images prior to FFA.

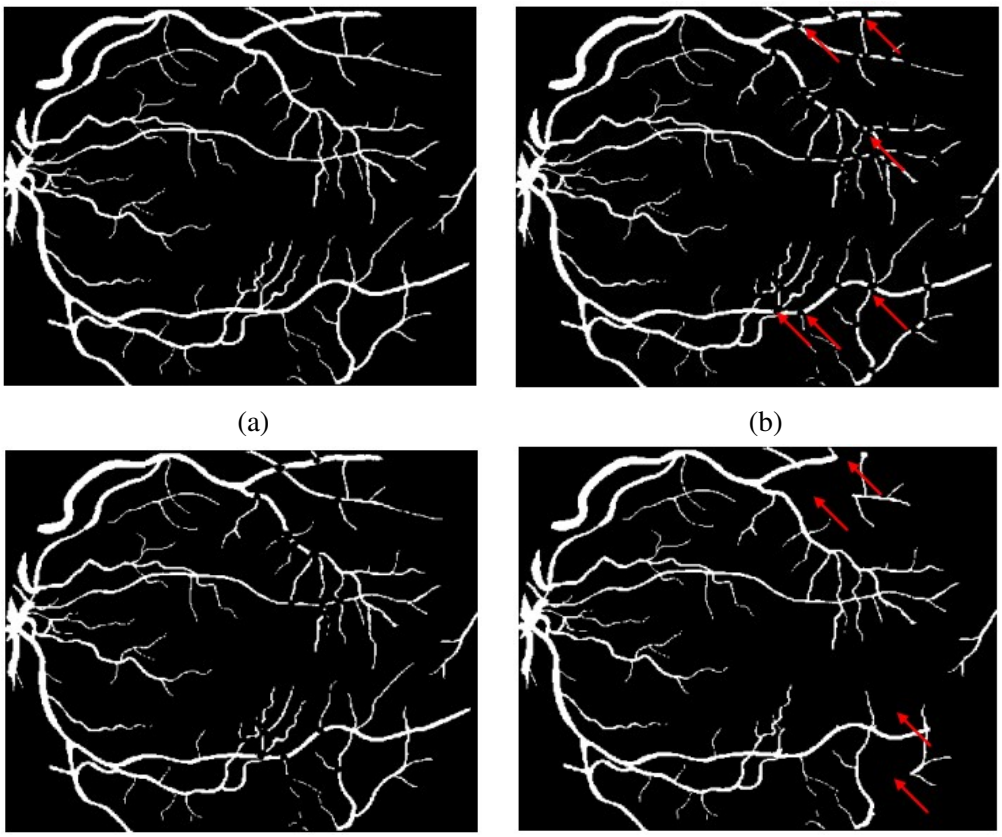


Figure 6.3: (a) Manually segmented image (im0001.ah) from the STARE database, (b) segmented image but with no junctions to right of centre of the image (indicated by red arrows), (c) segmented image with half of the junctions removed to right of centre of the image, (d) segmented image with vessels segments removed (indicated by red arrows).

3. **Edinburgh Mild Stroke Study**

FFA and MFA were performed on whole segmented vasculature as well as on different regions of an image. MFA was performed on both segmented

and skeletonised images. The images were divided into different regions to investigate whether changes to the retinal vasculature relating to stroke sub-type and disease (and which might constitute a biomarker) manifest in particular regions of the fundus. The different region-based procedures are presented below.

(i) **PROCEDURE # 1 - Whole Image**: MFA was performed on the whole vasculature in an input image, i.e. segmented image and in skeletonised version.

(ii) **PROCEDURE # 2 - Quadrant Wise**: The input image was divided into four quadrants around the OD. If the image was from a right eye, quadrant I was upper right with quadrant II through to IV labelled in an anti-clockwise direction (see Figure 6.4). If the image was of a left eye then quadrant I was upper left with quadrant II to through IV labelled in a clockwise direction (see Figure 6.5)

(iii) **PROCEDURE # 3 - Rotated Quadrant Wise**: The quadrants coordinates were rotated by $45^\circ$ and analysis was performed on rotated quadrants. See Figure 6.6 and Figure 6.7. For a right eye image, the quadrant labelling was chosen anti-clockwise with quadrant I just above the OD (see Figure 6.6). Whereas, for a left eye image, the quadrant labelling ran clockwise with quadrant I just above the OD (see Figure 6.7).

(iv) **PROCEDURE # 4 - Horizontal 3 Step Division around the macula**: An input image was divided horizontally into three equal parts. To do this, first the OD centre is located and then the region of the image on the left (if the image was of a left eye ) or right (if a right eye), i.e. region containing macula, was divided into three equal parts - S1, S2 and S3 (See Figure 6.8 and Figure 6.9).

(v) **PROCEDURE # 5 - Horizontal 3 Step Division on Whole Image**: An input image was divided horizontally into three equal parts- S1w, S2w and S3w (See Figure 6.10).

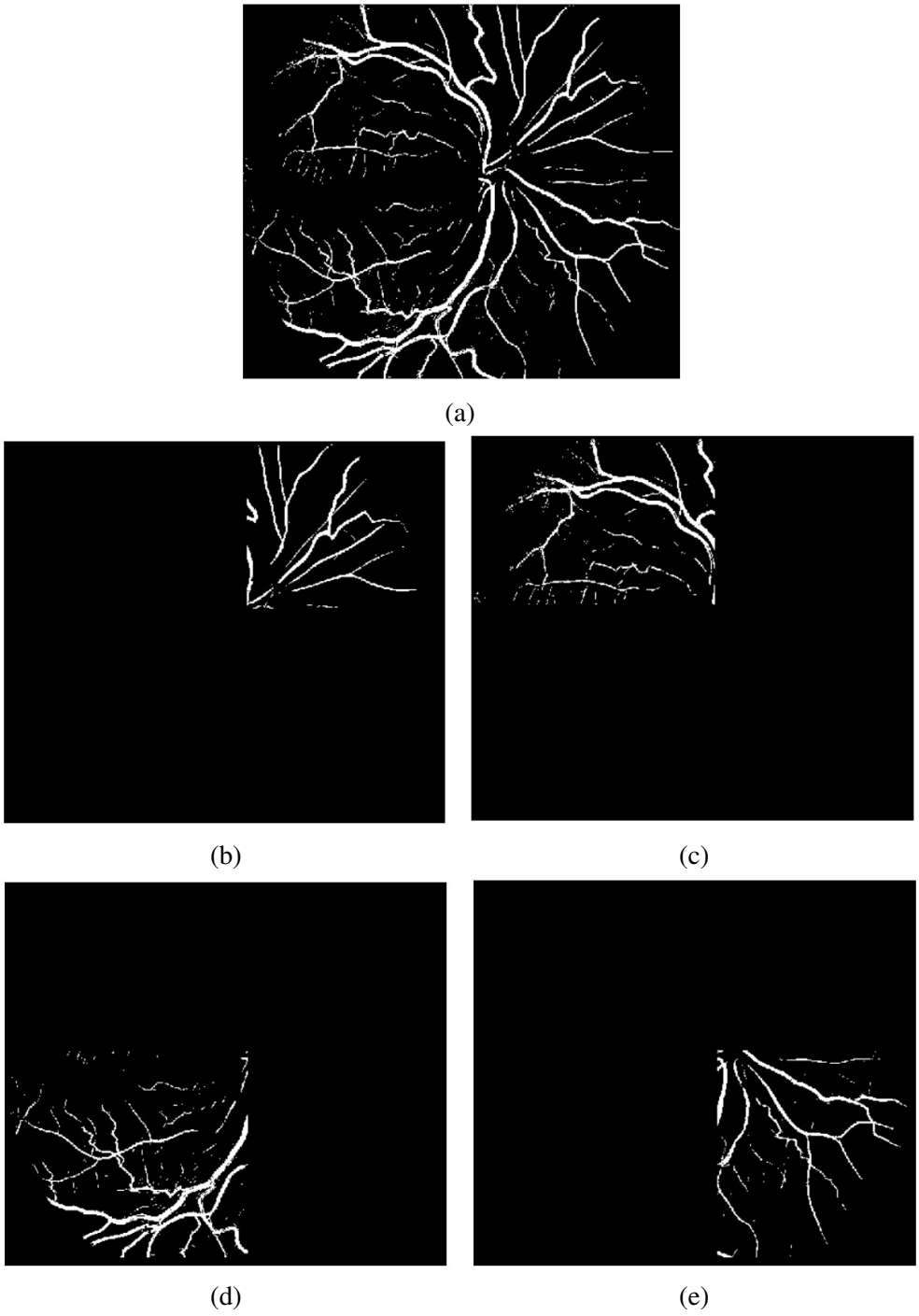

Figure 6.4: (a) Segmented image as the input divided into four quadrants (PROCEDURE # 2) when OD is on right (i.e. right eye) - (b) Quadrant I, (c) Quadrant II, (d) Quadrant III and (e) Quadrant IV.

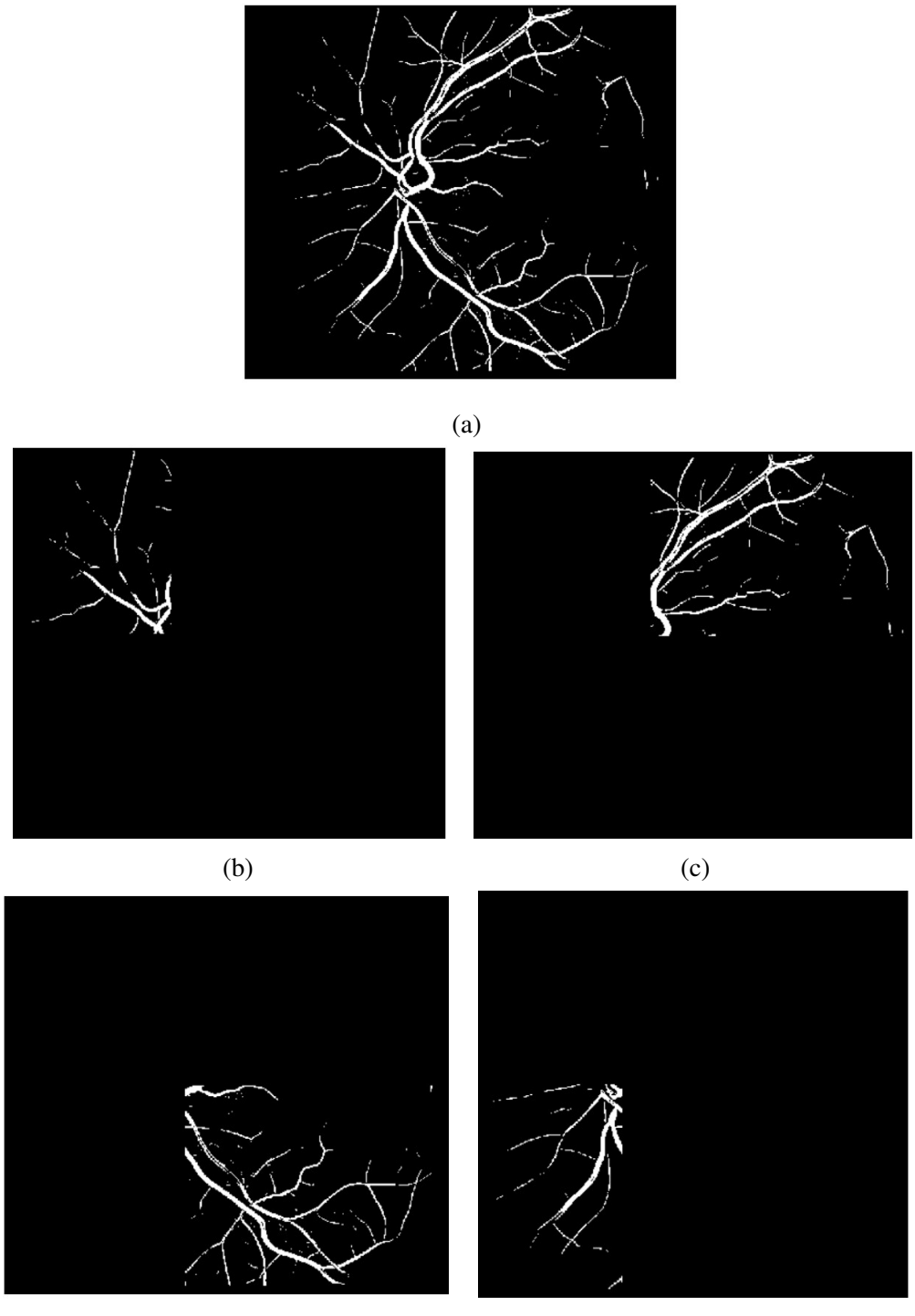

Figure 6.5: (a) Segmented image as the input divided into four quadrants (PROCEDURE # 2) when OD is on left (i.e. left eye) - (b) Quadrant I, (c) Quadrant II, (d) Quadrant III and (e) Quadrant IV.

(vi) **PROCEDURE # 6 - Horizontal 2 Step Division on Left or Right of OD**: Each input image on left (if OD is in right) or right (if OD is in left)

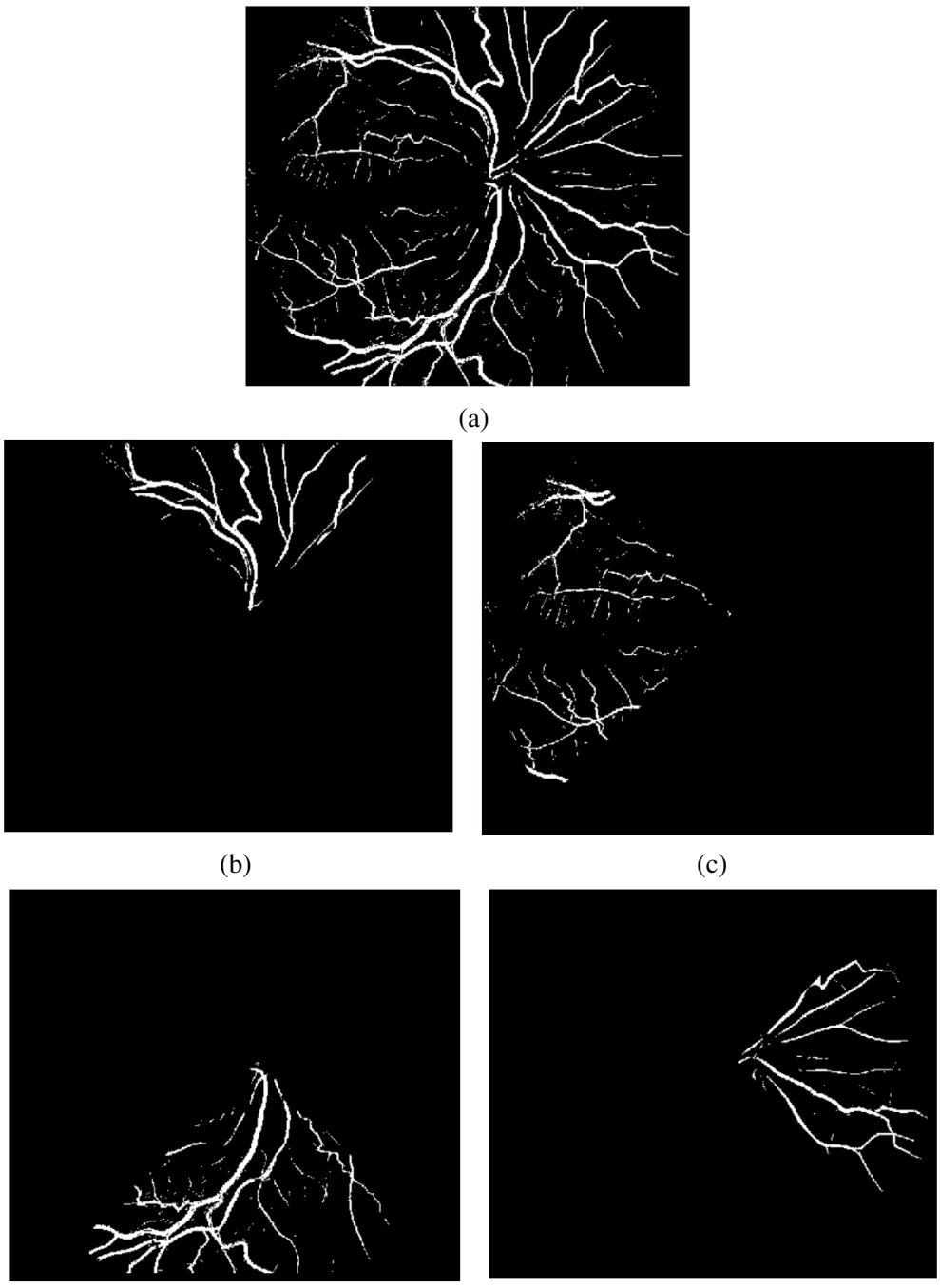

(a)

(b) (c)

(d) (e)

Figure 6.6: (a) Segmented right eye image as the input divided into four rotated quadrants (PROCEDURE # 3) - (b) Rotated Quadrant I, (c) Rotated Quadrant II, (d) Rotated Quadrant III and (e) Rotated Quadrant IV.

was divided horizontally into two equal parts: upper part (B) and lower part (D) (See Figure 6.11 and Figure 6.12).

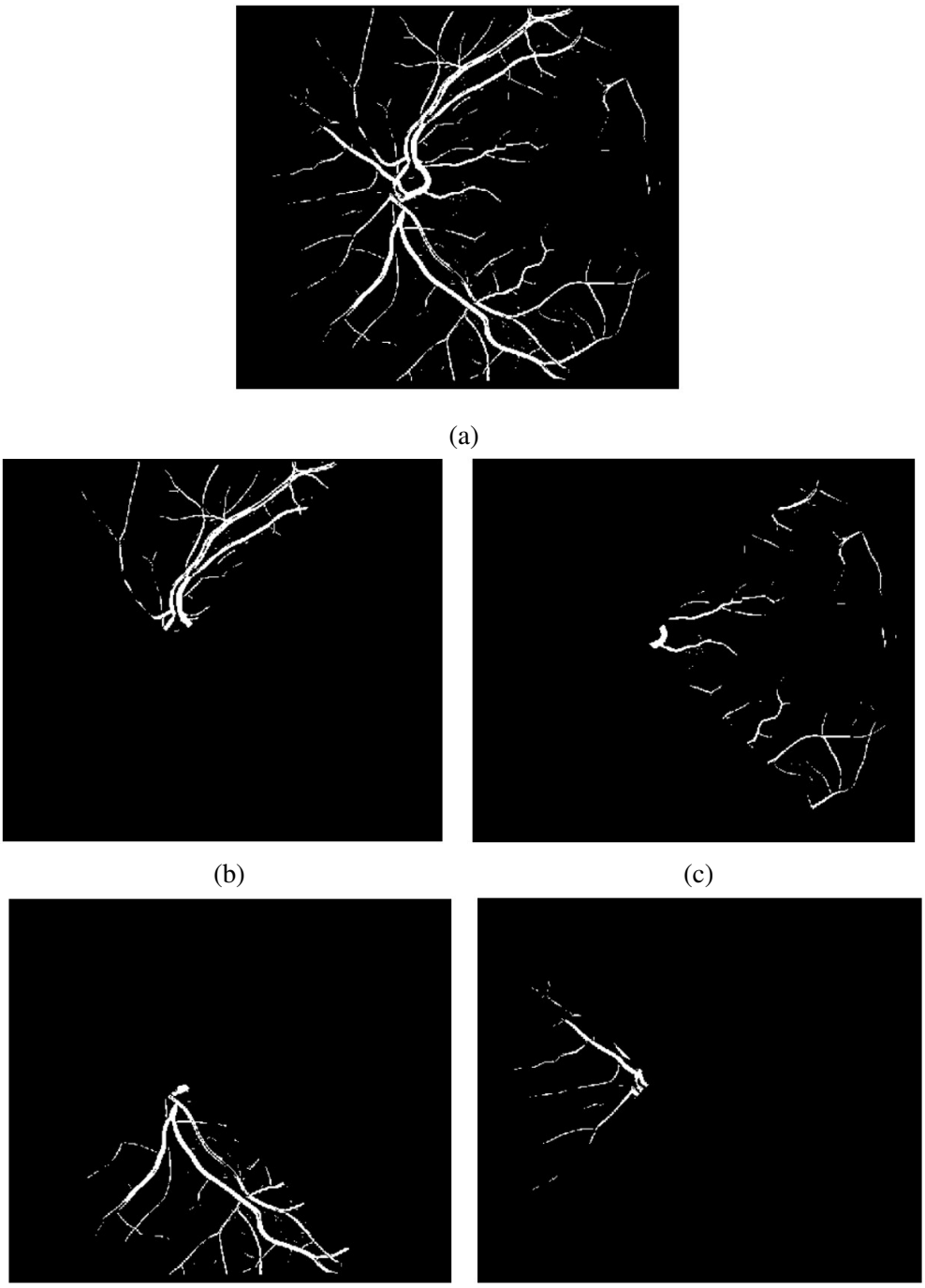


Figure 6.7: (a) Segmented left eye image as the input divided into four rotated quadrants (PROCEDURE # 3) - (b) Rotated Quadrant I, (c) Rotated Quadrant II, (d) Rotated Quadrant III and (e) Quadrant IV.

(vii) **PROCEDURE # 7 - Macular and Paramacular Region**: An input image was divided into 6 zones around the macula. See Figure 6.13 and Figure 6.14 where the portion of the image on left (if a right eye) or right (if a left

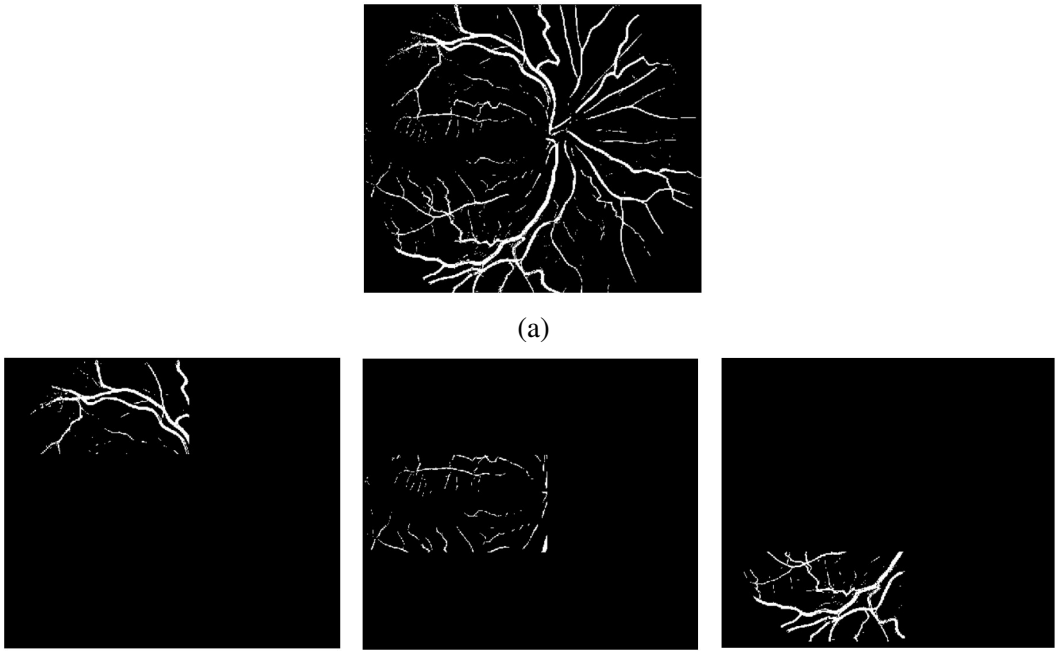

(a)

(b) (c) (d)

Figure 6.8: (a) Segmented right eye image as the input. Binary Image divided into three parts (PROCEDURE # 4) - (b) S1, (c) S2, (d) S3.

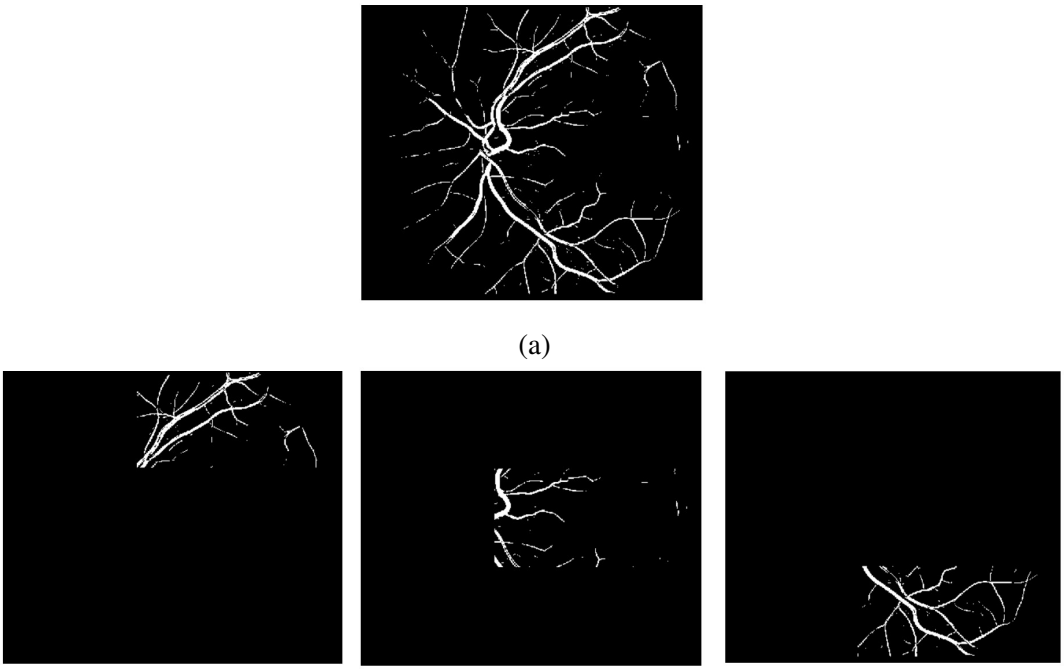

(a)

(b) (c) (d)

Figure 6.9: (a) Segmented left eye image as the input. Binary Image divided into three parts (PROCEDURE # 4) - (b) S1, (c) S2, (d) S3.

eye) of the OD was divided into 6 equal parts around the macula region. Regions just above the macula are labelled *a* and *b* and regions below are *e*

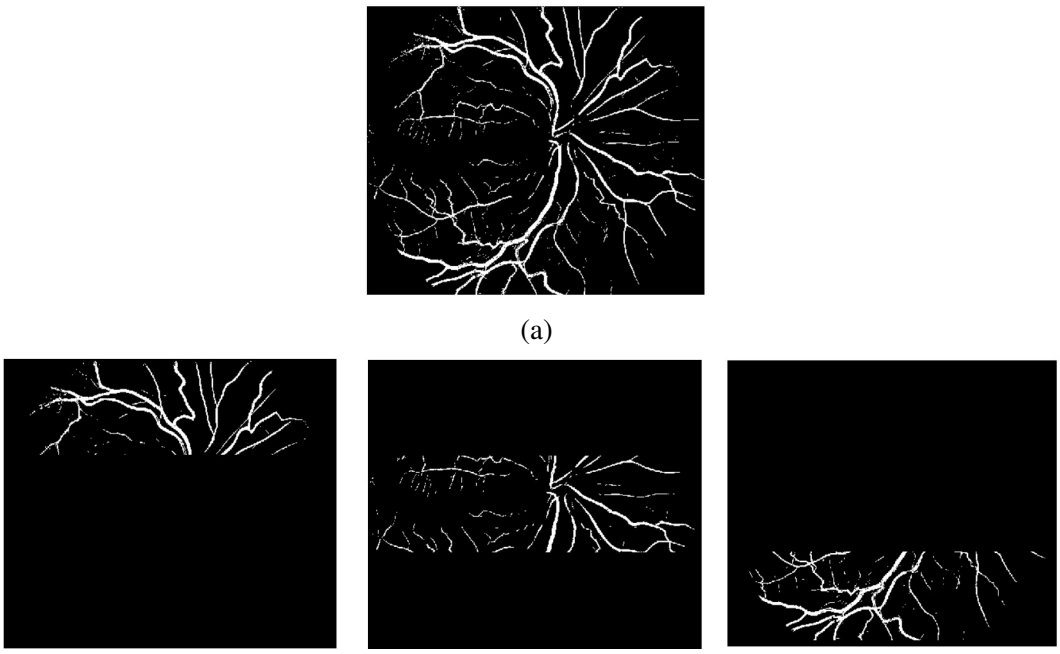

(a)

(b) (c) (d)

Figure 6.10: Segmented image as the input. Binary Image divided into three parts (PROCEDURE # 5):(b)S1w, (c) S2w, (d) S3w

and *f*. The two central regions are *c* and *d* (See Figure 6.13 and 6.14).

Henceforth regions *a*, *b*, *d*, *e* and *f* will denote the paramacular region whereas *c* will denote macular region.

(viii) **PROCEDURE # 8 - Circular Regions : Zone B, Zone C**: Zone B is an annulus 0.5 to 1 OD diameter and zone C is an annulus 0.5 to 2 OD diameter, both from the OD boundary (see Figure 6.15 and Figure 6.16).

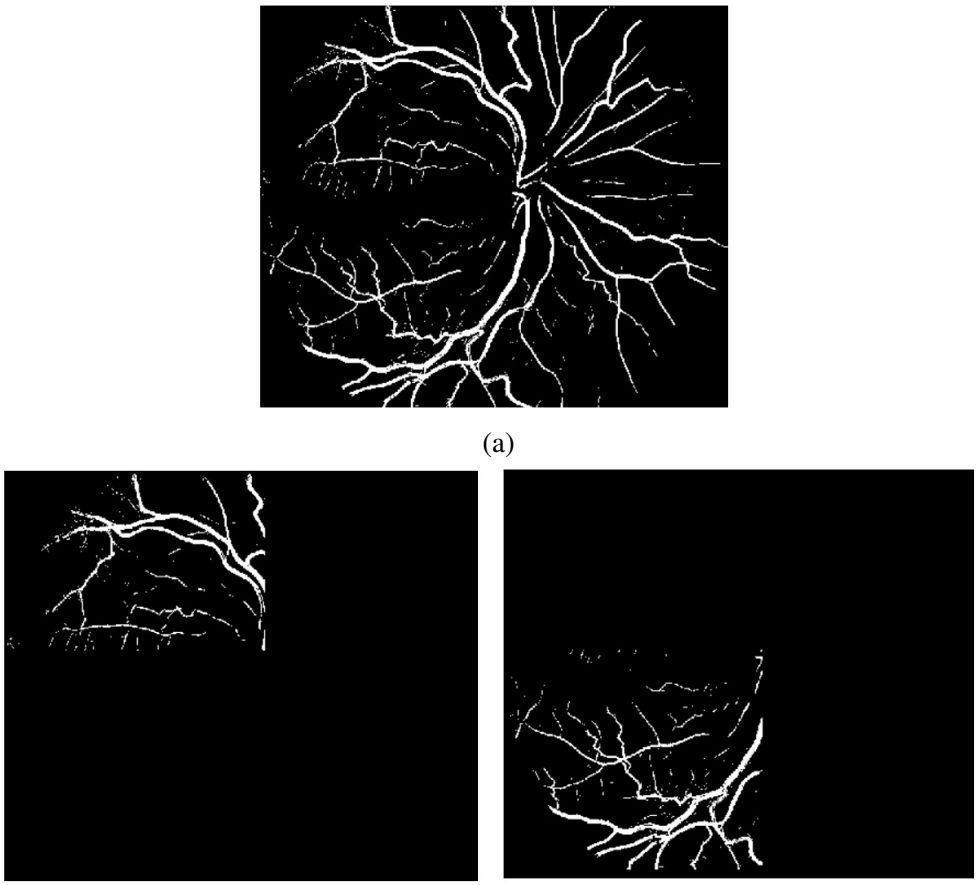

(a)

(b) (c)

Figure 6.11: (a) Segmented right eye image as the input. Binary Image divided into two equal parts (PROCEDURE # 6) - (b) Upper half (B) , (c) Lower half (D)

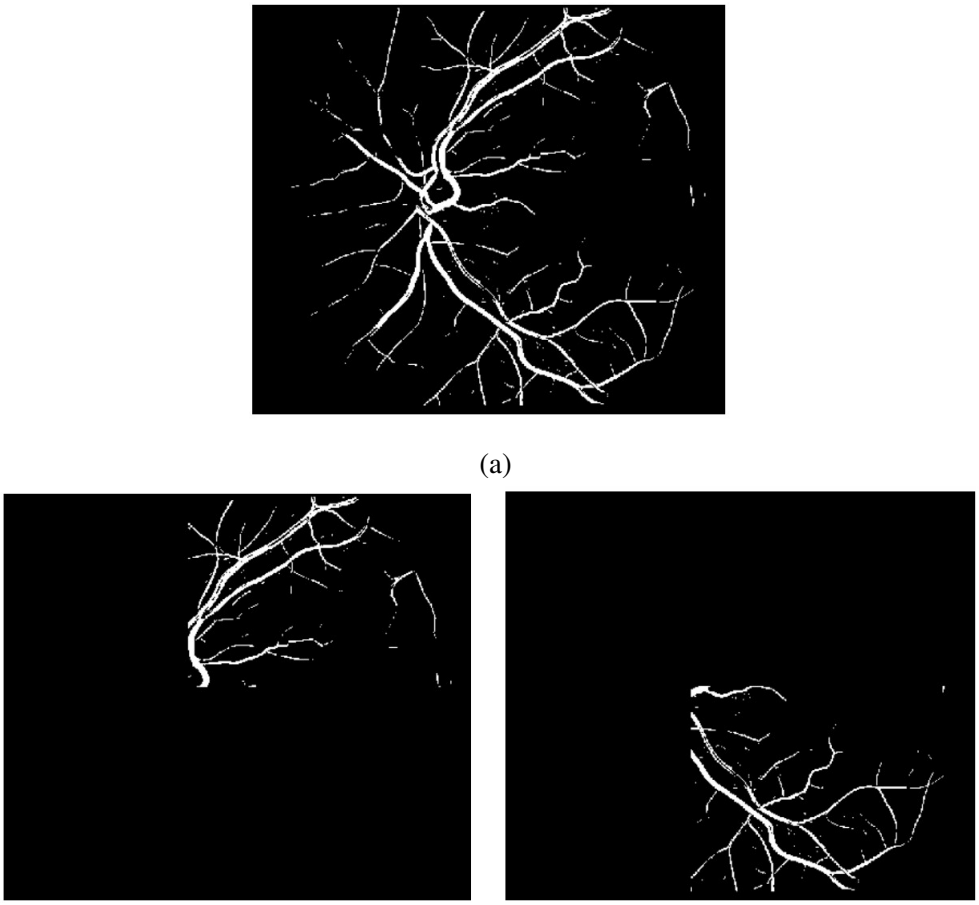

(a)

(b) (c)

Figure 6.12: (a) Segmented left eye image as the input. Binary Image divided into two equal parts (PROCEDURE # 6) when OD is on left: (b) Upper half (B) , (c) Lower half (D)

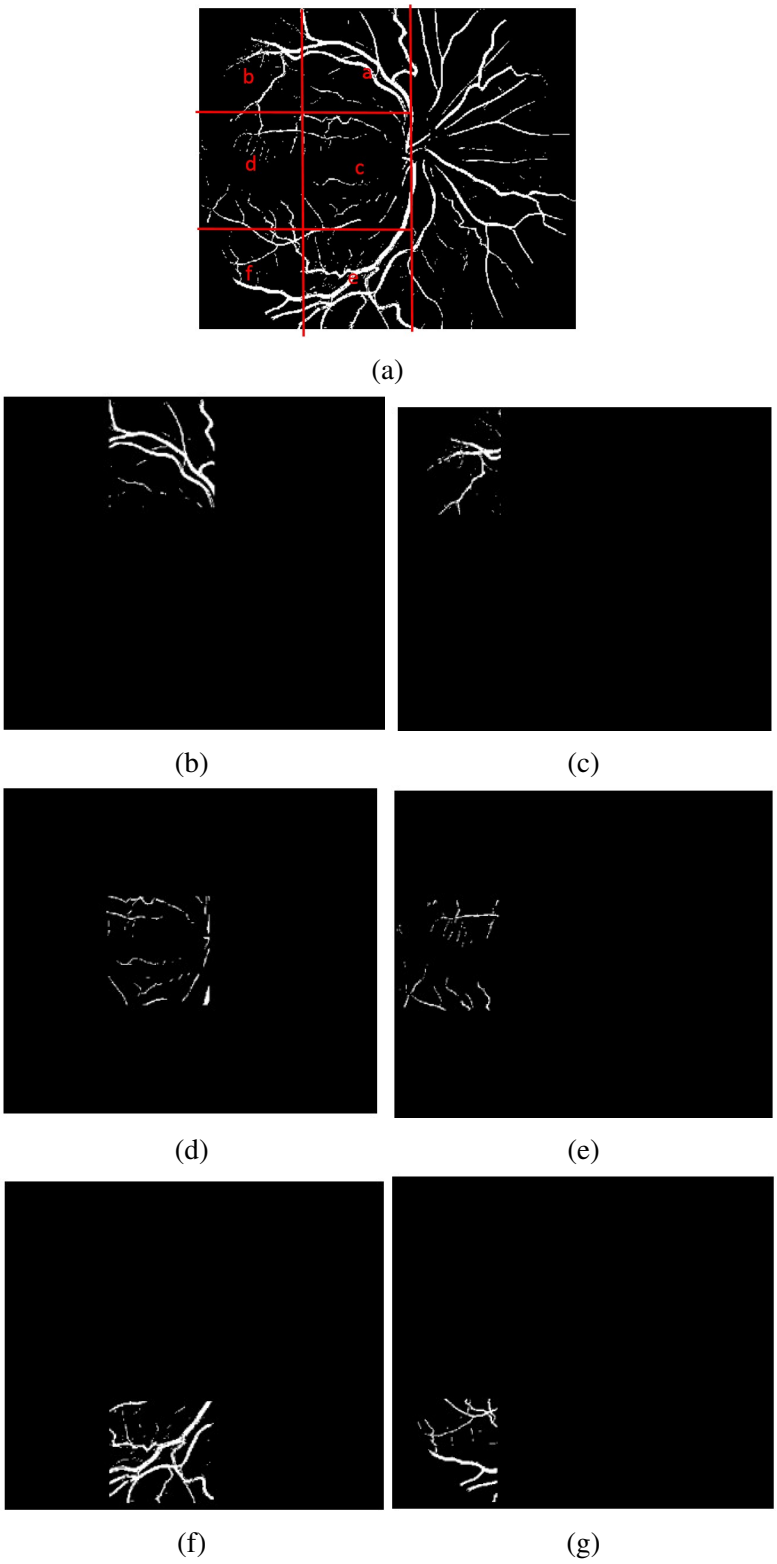


Figure 6.13: (a) Segmented right eye image as the input. Binary Image divided into 6 zones around macula (PROCEDURE # 7) - macular region (d), Paramacular region (b), (c), (e), (f) and (g).

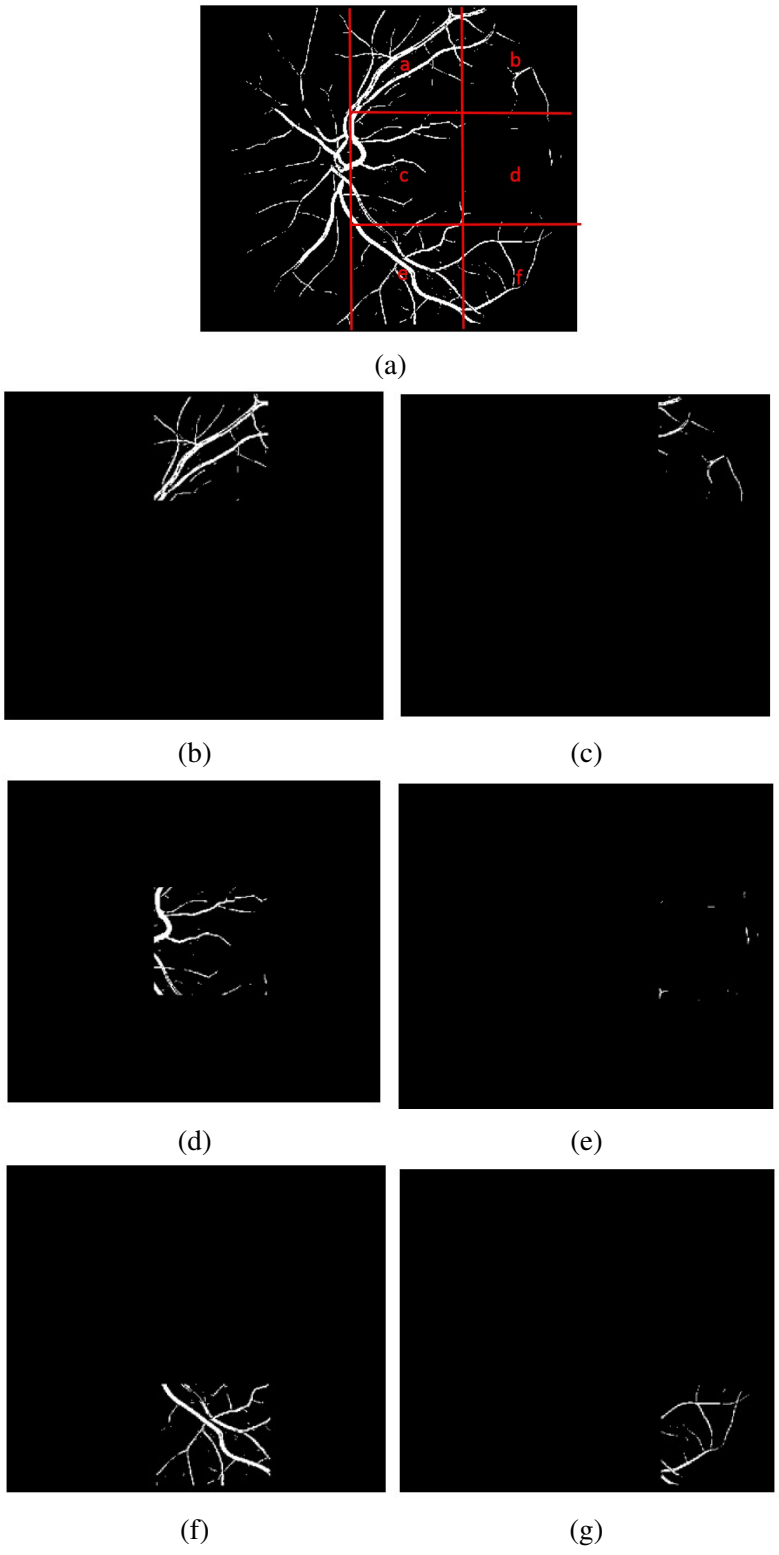


Figure 6.14: (a) Segmented left eye image as the input. Binary Image divided into 6 zones around macula (PROCEDURE # 7) - macular region (d), Paramacular region (b), (c), (e), (f) and (g).

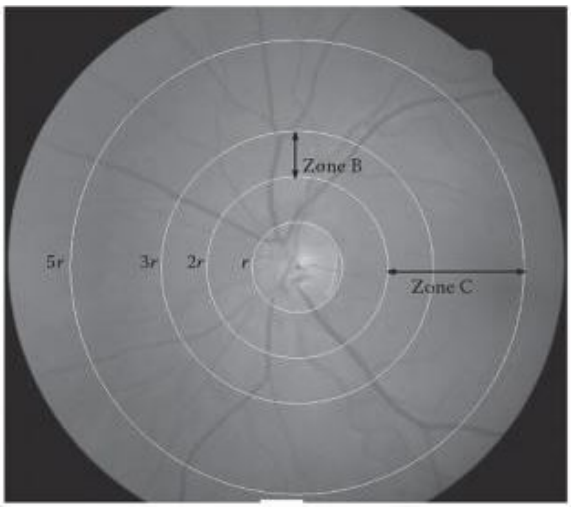


Figure 6.15: Retinal Image showing Zone B and Zone C (source:[217])

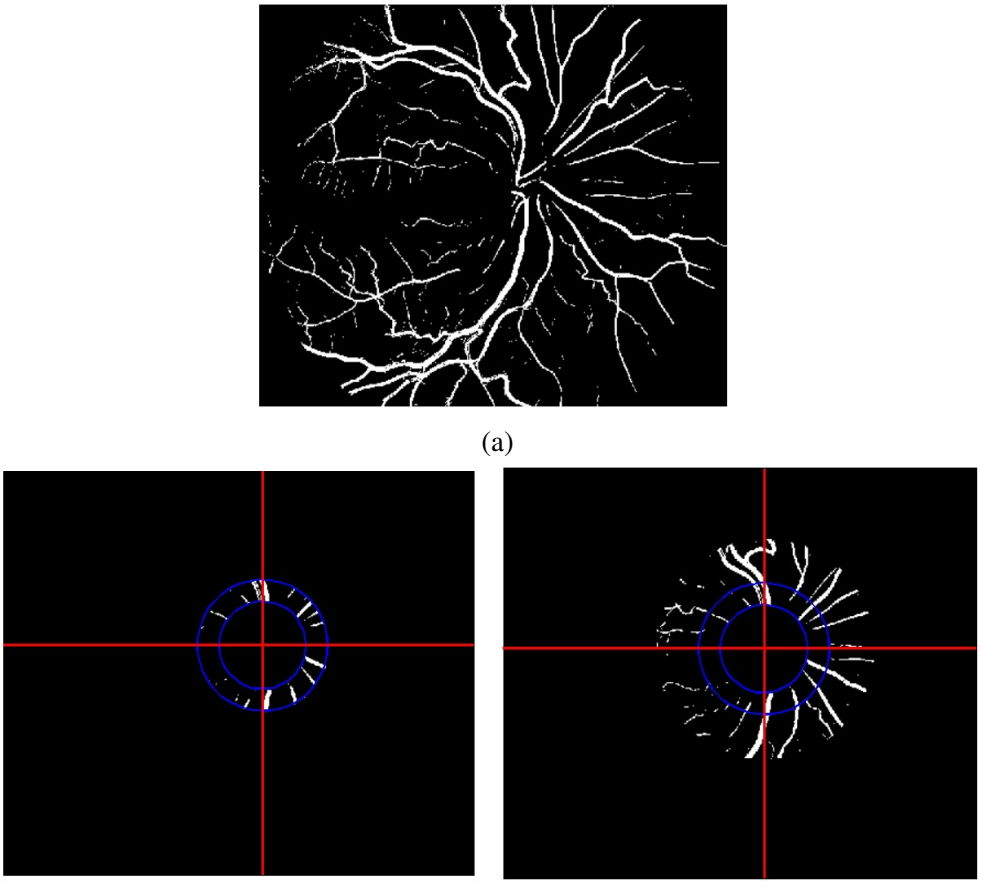

(a)

(b) (c)

Figure 6.16: (a) Segmented image as the input. Binary Image divided into zones (PROCEDURE # 8): (b) Zone B and (c) Zone C

## 6.5 Summary

This chapter described the concept of a fractal and the measurement of fractal dimension. In particular, two techniques to calculate FD were described, MFA and FFA. Stability of fractal analysis technique were tested through artificially introducing noise as well as by removing junctions and vessel segments to mimic the varying segmentation. In the last section different procedures to divide a retinal image into regions were proposed in order to enable an investigation into whether regional variations of vascular patterning might reveal hitherto undiscovered markers of change and disease.

# Chapter 7

# Results of Fractal Analysis

## 7.1 Introduction

In this chapter the feasibility of using fractal dimension (calculated from the retinal vasculature) as a potential bio-marker for differentiating normal and pathological images is investigated. The hypothesis tested here is that the degrading segmentation quality and the presence of noise will affect the effectiveness of fractal dimension to distinguish between the normal and pathological images. To test this hypothesis STARE dataset was used.

Furthermore, experiments were also conducted to verify whether fractal dimension can also be used as a possible potential biomarker to distinguish between the lacunar stroke (a distinct marker of cerebral small vessel disease) and cortical stroke (a distinct marker of large artery atherothromboembolic disease). To test this hypothesis, experiments were conducted using the Edinburgh mild stroke dataset. In these experiments fractal dimension was calculated using FFA and MFA techniques on the whole vasculature as well as in different regions of retinal vasculature.

In chapter 6 fractal analysis was introduced as a means of differentiating between normal and abnormal vascular patterns in fundus images. This chapter now

presents the results of experimental investigation into the capabilities of this fractal concept through the application of two methods of quantifying branching complexity, namely multifractal and Fourier fractal analysis. Section 7.2 gives the results for fractal analysis performed on two different datasets featuring images acquired from individuals with anticipated differences in their retinal vasculature. Outcome of the analysis is discussed in section 7.3. Finally, a summary is given in section 7.4.

## 7.2 Fractal Findings

Fractal analysis was performed on images from the STARE [143] and the Edinburgh Mild Stroke Study (MSS) [75] datasets. The performance of a faster approach for calculating multifractal dimension was investigated using two datasets. The multifractal and Fourier fractal analysis was performed on STARE dataset to differentiate between normal and pathological retinal images whereas, the Edinburgh MSS dataset was used to establish whether quantifiable differences might exist between two stroke subtypes (lacunar and cortical stroke). For all images in both datasets, the multifractal dimension $D_q$ was calculated for different values of $q$ (where $-20 < q < 20$). A region-based approach was implemented for further investigation into potential differences between the retinal vasculature for the two stroke subtypes in specific parts of the fundus. (see Section 7.2.2).

### 7.2.1 STARE

1. **Multifractal Fractal Analysis**

   Figure 7.1 shows an example of the generalised dimension spectrum $D_q$ w.r.t. $q$ calculated using the approach described in item 1 of section 6.2.3. It can be seen that the function $D_q$ is a decreasing function of $q$ with $D_0 > D_1 > D_2$. This is in accordance with the observations from [28] [92] and implies that the vessel structure was geometrically multifractal.

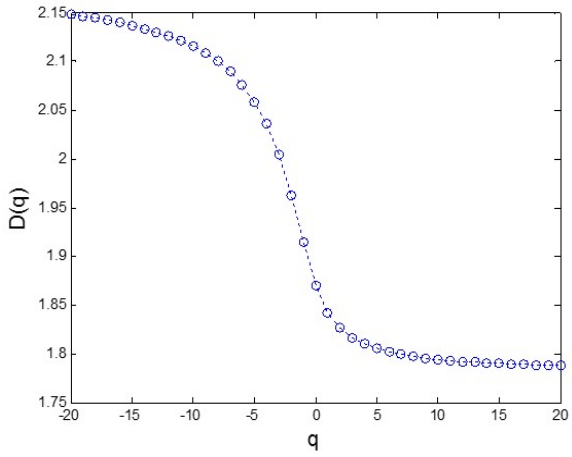


Figure 7.1: Generalised dimension spectrum, $D_q$ versus $q$, for a typical retinal image in the STARE dataset (image file im0001.ah.ppm [143])

Figure 7.2 illustrates the difference in $f(\alpha)$ spectrum for the two subgroups of STARE images which have been classified in the dataset as *normal* and *pathological*. The $f(\alpha)$ spectrum was averaged separately for the normal and pathological images for all four sets (segmented and skeletonised binary images from observers *AH* and *VK*). It can be seen that the skeletonised images exhibited a narrower $f(\alpha)$ spectrum as compared to the segmented vessel maps for both observers. The pathological cases displayed lower maximum value and the spectrum shifted to the left compared to the normal.

Table 7.1 presents the results for the capacity dimension ($D_0$) obtained by MFA. Comparing the fractal dimensions of the normal and pathological subgroups using a students t-test, p values were found to be 0.001 and $< 0.001$ for segmented and skeletonised versions respectively from images manually segmented by observer AH. Also, p values were found to be 0.001 for both segmented and skeletonised versions of the images manually segmented by observer VK. The p-values were found to be $< 0.01$ in all the cases, which implied a significant difference between the two subgroups. From Table 7.1, it can be concluded that the process of skeletonisation reduces the fractal dimension. In addition, it can be observed that the mean fractal dimension was found to be lower for the pathological images compared to the normal ones, which makes sense as pathological condition reduces the complexity of

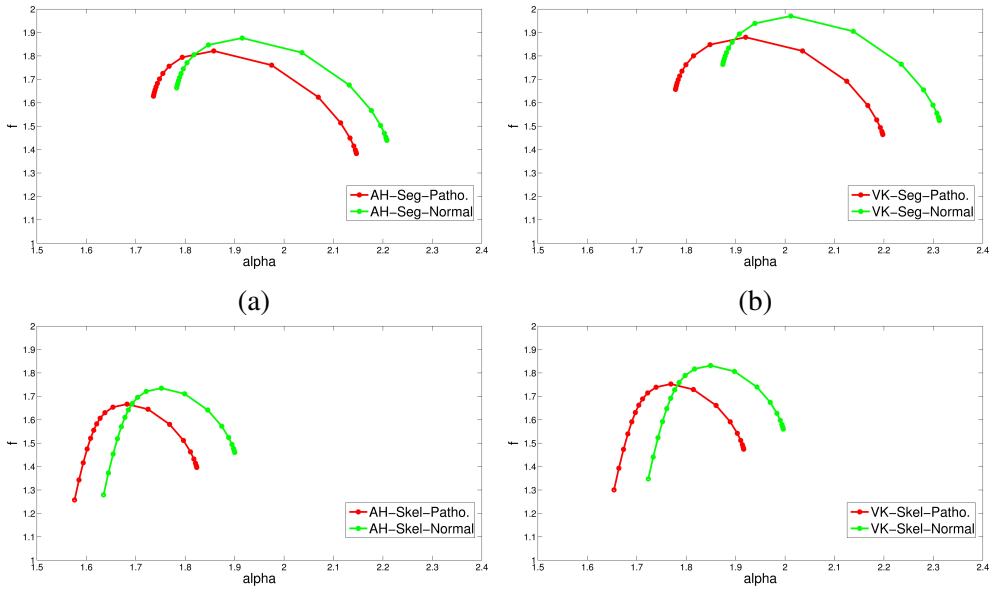


(a) (b) (c) (d)

Figure 7.2: The $f(\alpha)$ spectrum averaged separately for normal (green) and pathological (red) images in the STARE dataset. (a) and (c) f-spectrums from manually segmented and skeletonised vessels maps by observer AH. (b) and (d) f-spectrums from manually segmented and skeletonised vessels maps by observer VK.

the vascular pattern.

Table 7.2 shows the $D_0$ values calculated by MFA after the removal of either all of the detected junctions or half of the detected junctions from the left or right of image centre on both segmented and skeletonised images (by observer AH). Furthermore, it also contains the $D_0$ values obtained after removing some segments from the image. From Table 7.2, it can be concluded that the p-values (obtained by a t-test) in all the cases were $< 0.01$, hence showed a significant difference between the normal and pathological subgroups. A similar set of observation (i.e. p-value $< 0.01$) was established between the pathological and normal subgroups for images segmented by observer VK (see Table 7.3).

Table 7.4 shows $D_0$ values when noise was introduced into the segmentations of observer AH. The student t-test result obtained again showed a significant difference between the two subgroups ($p < 0.05$). In short, there was a significant difference between the two subgroups when MFA was performed on noisy images, vessels maps and skeletonised versions, from both observers (see APPENDIX B).

2. **Fourier Fractal Analysis**

   Table 7.1 presents results for FFA applied to the contrast enhanced grayscale STARE images. It can be seen that the FFD calculated for pathological and normal cases showed a significant difference ($p < 0.01$) between subgroups with a t-test ($p=0.007$). The results when FFA was applied to the noise corrupted, contrast enhanced grayscale images are also displayed in Table 7.4. A similar observation was made here, that two groups differ significantly ($p < 0.05$). A significant difference ($p < 0.05$) was also found when the green channel was used as the input to FFA for the STARE images (see APPENDIX B).

### 7.2.2 Edinburgh Mild Stroke Dataset

1. **Multifractal Fractal Analysis**

   In Table 7.5 the mean (and std.) for capacity dimension, $D_0$, obtained using MFA for computer segmented and skeletonised images from the mild stroke study database are given for different regions. It also shows the p-values obtained using a student's t-test to ascertain whether a significant difference exists or not between the two stroke subtypes (cortical and lacunar). It can be observed from the analysis performed on segmented images that region *S3* from PROCEDURE 4 and region *e* from PROCEDURE 7 show a significant difference ($p < 0.05$). Whereas, when analysis was performed on skeletonised images, quadrant II of PROCEDURE 2, region $S1$ and $S3$ of PROCEDURE 4, region *B* of PROCEDURE 6 and region *a* and *e* of PROCEDURE 7 showed significant differences ($p < 0.05$) between two ischaemic stroke subtypes.

   Figure 7.3 shows the $f(\alpha)$ spectrum for cortical and lacunar images when the MFA was performed on whole image (PROCEDURE 1). It shows that there is no significant difference between the two subgroups. Figure 7.4 shows an example of $f(\alpha)$ spectrum for $S1$, $S2$ and $S3$ regions of cortical and lacunar images as obtained from MFA using PROCEDURE 4 where two subgroups showed a significant difference in region $S1$ and $S3$.

| Images | Status | AH Seg. D0 | AH Skel. D0 | VK Seg. D0 | VK Skel. D0 | FFD D |
|---|---|---|---|---|---|---|
| im0001 | **P** | 1.870 | 1.715 | 1.905 | 1.759 | 1.604 |
| im0002 | **P** | 1.833 | 1.694 | 1.815 | 1.704 | 1.591 |
| im0003 | **P** | 1.815 | 1.668 | 1.844 | 1.753 | 1.639 |
| im0004 | **P** | 1.821 | 1.646 | 1.819 | 1.706 | 1.588 |
| im0005 | **P** | 1.883 | 1.706 | 1.939 | 1.812 | 1.598 |
| im0044 | **P** | 1.824 | 1.675 | 1.936 | 1.810 | 1.572 |
| m0077 | N | 1.875 | 1.732 | 1.975 | 1.834 | 1.638 |
| im0081 | N | 1.858 | 1.718 | 1.987 | 1.853 | 1.663 |
| im0082 | N | 1.841 | 1.723 | 1.955 | 1.852 | 1.671 |
| im0139 | **P** | 1.840 | 1.708 | 1.983 | 1.84 | 1.581 |
| im0162 | N | 1.873 | 1.777 | 1.97 | 1.867 | 1.678 |
| im0163 | N | 1.865 | 1.717 | 1.939 | 1.778 | 1.634 |
| im0235 | N | 1.882 | 1.724 | 1.98 | 1.829 | 1.633 |
| im0236 | N | 1.884 | 1.727 | 1.967 | 1.812 | 1.590 |
| im0239 | N | 1.889 | 1.741 | 1.964 | 1.809 | 1.583 |
| im0240 | N | 1.894 | 1.714 | 1.982 | 1.819 | 1.627 |
| im0255 | N | 1.903 | 1.777 | 1.987 | 1.866 | 1.662 |
| im0291 | **P** | 1.780 | 1.632 | 1.830 | 1.693 | 1.566 |
| im0319 | **P** | 1.751 | 1.611 | 1.830 | 1.694 | 1.640 |
| im0324 | **P** | 1.797 | 1.613 | 1.899 | 1.754 | 1.604 |
| **Average** | **All** | 1.849 | 1.70 | 1.925 | 1.792 | 1.618 |
| **(Std.)** | | (0.041) | (0.047) | (0.063) | (0.058) | (0.034) |
| **Average** | **P** | **1.821** | **1.667** | **1.880** | **1.753** | **1.598** |
| **(Std.)** | | **(0.039)** | **(0.039)** | **(0.060)** | **(0.054)** | **(0.025)** |
| **Average** | N | 1.876 | 1.735 | 1.971 | 1.832 | 1.638 |
| **(Std.)** | | (0.018) | (0.023) | (0.015) | (0.028) | (0.032) |
| | **p-value** | 0.001 | $< 0.001$ | 0.001 | 0.001 | 0.007 |

Table 7.1: Capacity Dimension, $D_0$, for images from the STARE database segmented by observers AH and VK, together with their skeletonised version. Second column shows classification status for each of the image (*pathological* Or *normal*), and the last column gives FFD calculated from contrast enhanced grayscale images. Average and standard deviation (Std.) of fractal dimensions of **All**, *pathological* (**P**) and *normal* (**N**) images are also indicated.

| | | No Junction | | Half Junction | | Vessel removed | |
|---|---|---|---|---|---|---|---|
| | | Segmented | Skeltonised | Segmented | Skeltonised | Segmented | Skeltonised |
| **Images** | **Status** | **D0** | **D0** | **D0** | **D0** | **D0** | **D0** |
| im0001 | **P** | 1.859 | 1.705 | 1.864 | 1.710 | 1.850 | 1.692 |
| im0002 | **P** | 1.826 | 1.686 | 1.829 | 1.689 | 1.802 | 1.662 |
| im0003 | **P** | 1.807 | 1.660 | 1.811 | 1.665 | 1.791 | 1.640 |
| im0004 | **P** | 1.810 | 1.639 | 1.815 | 1.643 | 1.769 | 1.595 |
| im0005 | **P** | 1.868 | 1.696 | 1.875 | 1.700 | 1.851 | 1.675 |
| im0044 | **P** | 1.815 | 1.667 | 1.820 | 1.671 | 1.782 | 1.633 |
| im0077 | N | 1.866 | 1.721 | 1.870 | 1.726 | 1.854 | 1.707 |
| im0081 | N | 1.845 | 1.706 | 1.850 | 1.711 | 1.840 | 1.695 |
| im0082 | N | 1.831 | 1.712 | 1.836 | 1.717 | 1.814 | 1.694 |
| im0139 | **P** | 1.828 | 1.698 | 1.835 | 1.702 | 1.803 | 1.674 |
| im0162 | N | 1.859 | 1.763 | 1.865 | 1.769 | 1.861 | 1.764 |
| im0163 | N | 1.856 | 1.713 | 1.859 | 1.716 | 1.832 | 1.688 |
| im0235 | N | 1.873 | 1.716 | 1.877 | 1.719 | 1.865 | 1.702 |
| im0236 | N | 1.874 | 1.718 | 1.878 | 1.721 | 1.867 | 1.706 |
| im0239 | N | 1.877 | 1.729 | 1.882 | 1.734 | 1.864 | 1.717 |
| im0240 | N | 1.882 | 1.706 | 1.888 | 1.707 | 1.860 | 1.679 |
| im0255 | N | 1.888 | 1.762 | 1.894 | 1.768 | 1.89 | 1.766 |
| im0291 | **P** | 1.777 | 1.630 | 1.778 | 1.631 | 1.737 | 1.592 |
| im0319 | **P** | 1.746 | 1.604 | 1.749 | 1.608 | 1.702 | 1.557 |
| im0324 | **P** | 1.787 | 1.606 | 1.792 | 1.607 | 1.727 | 1.541 |
| **Average** | **All** | 1.839 | 1.692 | 1.843 | 1.696 | 1.818 | 1.669 |
| **(Std.)** | | (0.0389) | (0.0449) | (0.0396) | (0.0458) | ( 0.0527) | (0.06) |
| **Average** | **P** | **1.812** | **1.659** | **1.817** | **1.663** | **1.781** | **1.626** |
| **(Std.)** | | **(0.037)** | **(0.038)** | **(0.038)** | **(0.039)** | **(0.049)** | **(0.052)** |
| **Average** | **N** | 1.865 | 1.725 | 1.870 | 1.729 | 1.855 | 1.712 |
| **(Std.)** | | (0.018) | (0.021) | (0.018) | (0.022) | (0.021) | (0.030) |
| | **p-value** | 0.001 | $< 0.001$ | 0.001 | $< 0.001$ | 0.001 | $< 0.001$ |

Table 7.2: Capacity Dimension, $D_0$, for images from the STARE database when all or half of the detected junctions were removed from skeletonised and segmented versions (observer AH). $7^{th}$ and $8^{th}$ columns give $D_0$ values when vessel sections were removed from segmented and skeletonised images. Average and standard deviation (Std.) of fractal dimensions of **All**, *pathological* (**P**) and *normal* (**N**) images are also indicated.

| | | No Junction | | Half Junction | | Vessel removed | |
|---|---|---|---|---|---|---|---|
| | | Segmented | Skeltonised | Segmented | Skeltonised | Segmented | Skeltonised |
| **Images** | **Status** | **D0** | **D0** | **D0** | **D0** | **D0** | **D0** |
| im0001 | **P** | 1.893 | 1.752 | 1.898 | 1.755 | 1.887 | 1.735 |
| im0002 | **P** | 1.810 | 1.698 | 1.812 | 1.701 | 1.792 | 1.68 |
| im0003 | **P** | 1.835 | 1.747 | 1.84 | 1.750 | 1.824 | 1.731 |
| im0004 | **P** | 1.807 | 1.697 | 1.812 | 1.702 | 1.785 | 1.666 |
| im0005 | **P** | 1.916 | 1.792 | 1.928 | 1.801 | 1.927 | 1.797 |
| im0044 | **P** | 1.917 | 1.795 | 1.926 | 1.802 | 1.914 | 1.791 |
| im0077 | N | 1.958 | 1.818 | 1.966 | 1.825 | 1.964 | 1.822 |
| im0081 | N | 1.970 | 1.840 | 1.976 | 1.845 | 1.973 | 1.840 |
| im0082 | N | 1.933 | 1.831 | 1.945 | 1.842 | 1.944 | 1.841 |
| im0139 | P | 1.968 | 1.834 | 1.976 | 1.836 | 1.966 | 1.824 |
| im0162 | N | 1.949 | 1.848 | 1.956 | 1.855 | 1.960 | 1.858 |
| im0163 | N | 1.924 | 1.769 | 1.930 | 1.774 | 1.911 | 1.757 |
| im0235 | N | 1.968 | 1.822 | 1.973 | 1.823 | 1.963 | 1.810 |
| im0236 | N | 1.953 | 1.804 | 1.959 | 1.807 | 1.952 | 1.795 |
| im0239 | N | 1.952 | 1.800 | 1.957 | 1.803 | 1.943 | 1.791 |
| im0240 | N | 1.965 | 1.815 | 1.974 | 1.816 | 1.955 | 1.793 |
| im0255 | N | 1.966 | 1.848 | 1.974 | 1.856 | 1.978 | 1.857 |
| im0291 | **P** | 1.824 | 1.689 | 1.826 | 1.690 | 1.805 | 1.665 |
| im0319 | **P** | 1.821 | 1.686 | 1.826 | 1.690 | 1.810 | 1.671 |
| im0324 | **P** | 1.875 | 1.730 | 1.888 | 1.741 | 1.867 | 1.725 |
| **Average** | **All** | 1.910 | 1.781 | 1.917 | 1.786 | 1.906 | 1.773 |
| **(Std.)** | | (0.060) | (0.056) | (0.061) | (0.057) | (0.067) | (0.065) |
| **Average** | **P** | **1.867** | **1.742** | **1.873** | **1.747** | **1.858** | **1.729** |
| **(Std.)** | | **(0.055)** | **(0.052)** | **(0.058)** | **(0.052)** | **(0.064)** | **(0.059)** |
| **Average** | **N** | 1.954 | 1.819 | 1.961 | 1.825 | 1.954 | 1.816 |
| **(Std.)** | | (0.015) | (0.024) | (0.015) | (0.026) | (0.019) | (0.033) |
| | **p-value** | $< 0.001$ | 0.001 | 0.001 | 0.001 | 0.001 | 0.001 |

Table 7.3: Capacity Dimension, $D_0$, for images from the STARE database when all or half of the detected junctions were removed from skeletonised and segmented versions (observer VK). $7^{th}$ and $8^{th}$ column shows $D_0$ values when the vessels were removed from segmented and skeletonised images. Average and standard deviation (Std.) of fractal dimensions of **All**, *pathological* (**P**) and *normal* (**N**) images are also indicated.

| Images | Status | Multifractal AH-Segmented With Noise D0 | FFD Gaussian | FFD Sat and pepper D | FFD Poissons |
|---|---|---|---|---|---|
| im0001 | **P** | 1.946 | 2.054 | 2.112 | 1.847 |
| im0002 | **P** | 1.924 | 1.998 | 2.076 | 1.810 |
| im0003 | **P** | 1.914 | 1.962 | 2.057 | 1.824 |
| im0004 | **P** | 1.911 | 1.946 | 2.044 | 1.792 |
| im0005 | **P** | 1.955 | 1.913 | 2.002 | 1.773 |
| im0044 | **P** | 1.919 | 1.939 | 2.029 | 1.775 |
| im0077 | N | 1.949 | 2.001 | 2.101 | 1.850 |
| im0081 | N | 1.938 | 2.008 | 2.099 | 1.855 |
| im0082 | N | 1.927 | 1.998 | 2.100 | 1.862 |
| im0139 | **P** | 1.925 | 1.895 | 1.989 | 1.760 |
| im0162 | N | 1.944 | 1.994 | 2.083 | 1.853 |
| im0163 | N | 1.942 | 2.006 | 2.078 | 1.837 |
| im0235 | N | 1.953 | 2.080 | 2.146 | 1.881 |
| im0236 | N | 1.954 | 2.020 | 2.102 | 1.833 |
| im0239 | N | 1.958 | 1.920 | 2.000 | 1.772 |
| im0240 | N | 1.961 | 1.929 | 2.038 | 1.793 |
| im0255 | N | 1.965 | 1.978 | 2.051 | 1.830 |
| im0291 | **P** | 1.890 | 1.873 | 1.967 | 1.731 |
| im0319 | **P** | 1.875 | 1.946 | 2.063 | 1.820 |
| im0324 | **P** | 1.896 | 1.909 | 2.016 | 1.783 |
| **Average** | **All** | 1.932 | 1.968 | 2.058 | 1.814 |
| **(Std.)** | | (0.025) | (0.054) | (0.047) | (0.040) |
| **Average** | **P** | **1.915** | **1.943** | **2.035** | **1.791** |
| **(Std.)** | | **(0.024)** | **(0.052)** | **(0.043)** | **(0.034)** |
| **Average** | **N** | 1.950 | 1.993 | 2.079 | 1.836 |
| **(Std.)** | | (0.011) | (0.045) | (0.041) | (0.033) |
| | **p-value** | 0.002 | 0.035 | 0.030 | 0.007 |

Table 7.4: Capacity Dimension, $D_0$, for images from the STARE database calculated using MFA (Column 3) after noise was introduced into the images that were segmented by observer AH. Column 4 shows the FFD with different noise introduced in grayscale images. Average and standard deviation (Std.) of fractal dimensions of **All**, *pathological* (**P**) and *normal* (**N**) images are also indicated.

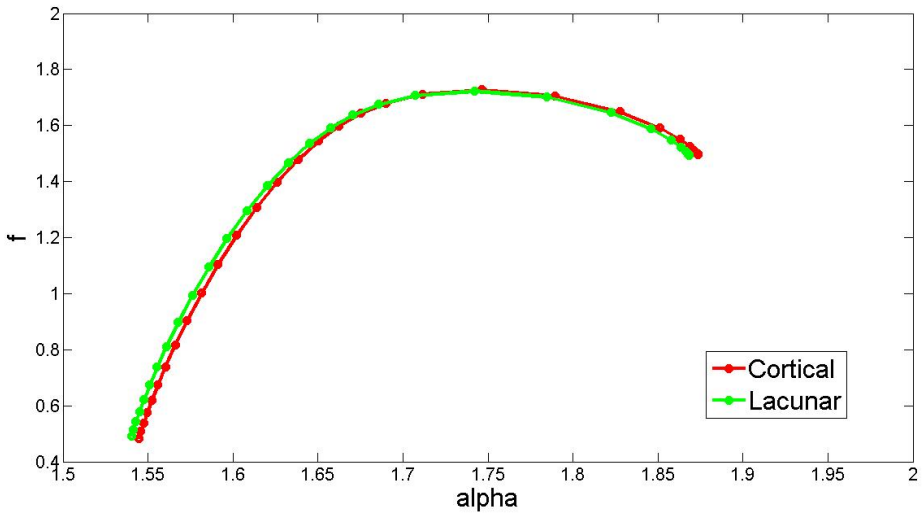


Figure 7.3: $f(\alpha)$ spectrum for cortical and lacunar stroke subtypes for skeletonise images with PROCEDURE 1.

Figure 7.5 illustrates regions where the subsequent testing showed a significant difference in the MFA between the cortical and lacunar groups using skeletonised version of images. They were regions in the upper and lower half on left or right of OD.

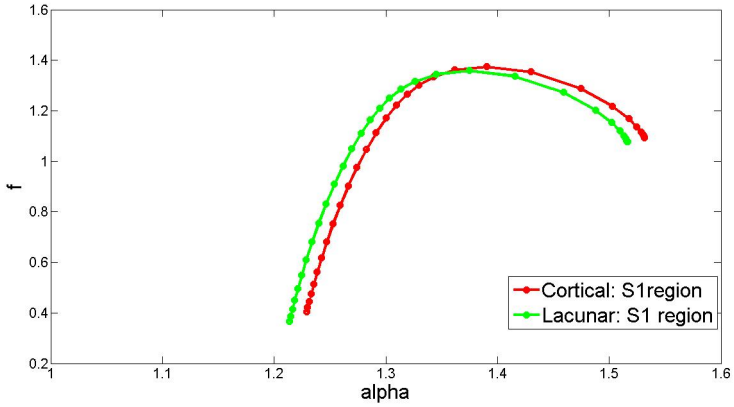


(a)

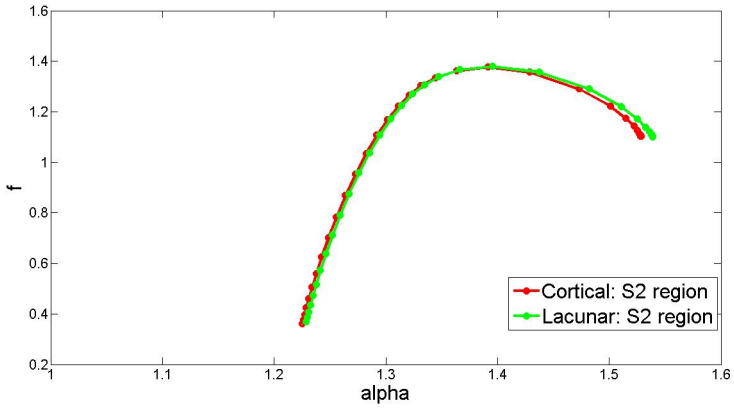


(b)

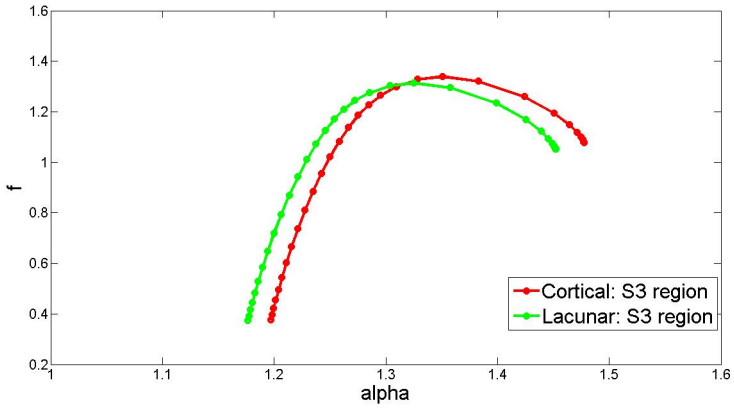


(c)

Figure 7.4: $f(\alpha)$ spectrum for cortical and lacunar stroke subtypes for skeletonise images with PROCEDURE 4

**SEGMENTED**

| **Cortical** | **PROCEDURE** 1 | **PROCEDURE** 2 | | | | **PROCEDURE** 3 | | | | **PROCEDURE** 4 | | | **PROCEDURE** 5 | | | **PROCEDURE** 6 | | **PROCEDURE** 7 | | | | | | **PROCEDURE** 8 | |
|---|---|---|---|---|---|---|---|---|---|---|---|---|---|---|---|---|---|---|---|---|---|---|---|---|---|
| | D0 | D0-I | D0-II | D0-III | D0-IV | D0-I | D0-II | D0-III | D0-IV | S1 | S2 | S3 | S1 | S2 | S3 | B | D | a | b | c | d | e | f | Zone B | Zone C |
| **mean** | 1.854 | 1.534 | 1.585 | 1.581 | 1.535 | 1.604 | 1.539 | 1.617 | 1.409 | 1.509 | 1.496 | 1.468 | 1.634 | 1.614 | 1.599 | 1.585 | 1.581 | 1.452 | 1.187 | 1.446 | 1.124 | 1.400 | 1.173 | 1.485 | 1.737 |
| **std.** | 0.058 | 0.062 | 0.042 | 0.051 | 0.079 | 0.039 | 0.071 | 0.049 | 0.087 | 0.056 | 0.063 | 0.075 | 0.036 | 0.039 | 0.044 | 0.042 | 0.0513 | 0.048 | 0.141 | 0.0625 | 0.201 | 0.069 | 0.160 | 0.053 | 0.047 |
| **p-value** | 0.906 | 0.082 | 0.060 | 0.180 | 0.566 | 0.796 | 0.329 | 0.869 | 0.166 | 0.106 | 0.677 | **0.040** | 0.925 | 0.896 | 0.352 | 0.060 | 0.180 | 0.097 | 0.322 | 0.791 | 0.163 | **0.008** | 0.925 | 0.771 | 0.882 |

| **Lacunar** | **PROCEDURE** 1 | **PROCEDURE** 2 | | | | **PROCEDURE** 3 | | | | **PROCEDURE** 4 | | | **PROCEDURE** 5 | | | **PROCEDURE** 6 | | **PROCEDURE** 7 | | | | | | **PROCEDURE** 8 | |
|---|---|---|---|---|---|---|---|---|---|---|---|---|---|---|---|---|---|---|---|---|---|---|---|---|---|
| | D0 | D0-I | D0-II | D0-III | D0-IV | D0-I | D0-II | D0-III | D0-IV | S1 | S2 | S3 | S1 | S2 | S3 | B | D | a | b | c | d | e | f | Zone B | Zone C |
| **mean** | 1.853 | 1.549 | 1.573 | 1.571 | 1.541 | 1.602 | 1.529 | 1.615 | 1.426 | 1.495 | 1.500 | 1.444 | 1.635 | 1.615 | 1.593 | 1.573 | 1.571 | 1.439 | 1.166 | 1.448 | 1.162 | 1.370 | 1.175 | 1.482 | 1.734 |
| **std.** | 0.055 | 0.052 | 0.040 | 0.0489 | 0.061 | 0.0367 | 0.056 | 0.042 | 0.071 | 0.050 | 0.054 | 0.079 | 0.033 | 0.032 | 0.0435 | 0.0402 | 0.0489 | 0.050 | 0.134 | 0.056 | 0.144 | 0.073 | 0.141 | 0.049 | 0.040 |

**SKELETONISED**

| **Cortical** | **PROCEDURE** 1 | **PROCEDURE** 2 | | | | **PROCEDURE** 3 | | | | **PROCEDURE** 4 | | | **PROCEDURE** 5 | | | **PROCEDURE** 6 | | **PROCEDURE** 7 | | | | | | **PROCEDURE** 8 | |
|---|---|---|---|---|---|---|---|---|---|---|---|---|---|---|---|---|---|---|---|---|---|---|---|---|---|
| | D0 | D0-I | D0-II | D0-III | D0-IV | D0-I | D0-II | D0-III | D0-IV | S1 | S2 | S3 | S1 | S2 | S3 | B | D | a | b | c | d | e | f | Zone B | Zone C |
| **mean** | 1.728 | 1.407 | 1.457 | 1.458 | 1.408 | 1.464 | 1.427 | 1.479 | 1.306 | 1.375 | 1.377 | 1.339 | 1.501 | 1.494 | 1.468 | 1.457 | 1.457 | 1.309 | 1.081 | 1.321 | 1.037 | 1.263 | 1.065 | 1.349 | 1.607 |
| **std.** | 0.0527 | 0.062 | 0.046 | 0.052 | 0.075 | 0.040 | 0.072 | 0.049 | 0.086 | 0.057 | 0.053 | 0.071 | 0.037 | 0.034 | 0.043 | 0.046 | 0.052 | 0.046 | 0.133 | 0.047 | 0.194 | 0.065 | 0.147 | 0.0542 | 0.046 |
| **p-value** | 0.619 | 0.144 | **0.014** | 0.084 | 0.655 | 0.418 | 0.189 | 0.583 | 0.158 | **0.048** | 0.707 | **0.024** | 0.417 | 0.873 | 0.162 | **0.014** | 0.084 | **0.007** | 0.124 | 0.405 | 0.414 | **0.002** | 0.624 | 0.508 | 0.495 |

| **Lacunar** | **PROCEDURE** 1 | **PROCEDURE** 2 | | | | **PROCEDURE** 3 | | | | **PROCEDURE** 4 | | | **PROCEDURE** 5 | | | **PROCEDURE** 6 | | **PROCEDURE** 7 | | | | | | **PROCEDURE** 8 | |
|---|---|---|---|---|---|---|---|---|---|---|---|---|---|---|---|---|---|---|---|---|---|---|---|---|---|
| | D0 | D0-I | D0-II | D0-III | D0-IV | D0-I | D0-II | D0-III | D0-IV | S1 | S2 | S3 | S1 | S2 | S3 | B | D | a | b | c | d | e | f | Zone B | Zone C |
| **mean** | 1.724 | 1.419 | 1.441 | 1.4442 | 1.412 | 1.458 | 1.414 | 1.475 | 1.323 | 1.359 | 1.379 | 1.314 | 1.497 | 1.493 | 1.459 | 1.441 | 1.444 | 1.288 | 1.051 | 1.315 | 1.059 | 1.231 | 1.054 | 1.343 | 1.602 |
| **std.** | 0.053 | 0.055 | 0.040 | 0.048 | 0.0611 | 0.041 | 0.054 | 0.043 | 0.072 | 0.047 | 0.049 | 0.071 | 0.0316 | 0.032 | 0.0407 | 0.040 | 0.048 | 0.049 | 0.115 | 0.044 | 0.138 | 0.067 | 0.131 | 0.055 | 0.0433 |

Table 7.5: Mean and standard deviation (std.) of capacity dimension, $D_0$, for segmented and skeletonised images from the stroke database for different region wise analysis. Here p-value is highlighted for regions which shows significant difference ($p < 0.05$).

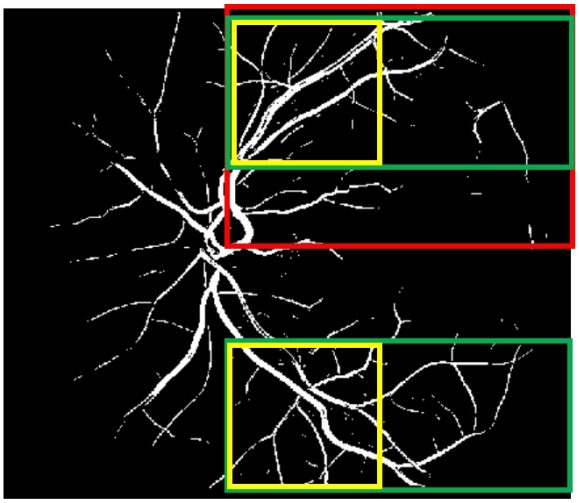

(a)

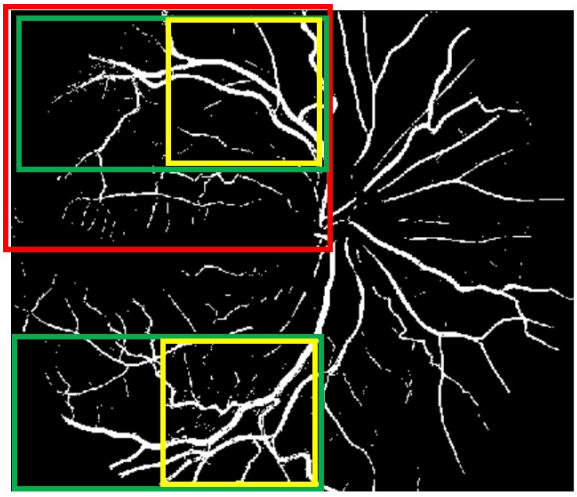

(b)

Figure 7.5: The regions which showed a significance difference between the two stroke subtype in skeletonised version of images when OD was located in the (a) left and (b) right hand side of a fundus image. Quadrant II of PROCEDURE 2 and region *B* of PROCEDURE 6 is marked in red, region $S1$ and $S3$ of PROCEDURE 4 are marked in green whereas region *a* and *e* of PROCEDURE 7 is marked in yellow.

2. **Fourier Fractal Analysis**

   Region wise analysis was also performed using FFA. It was observed that using FFA none of the region-based methods showed any significant differences between two stroke subtypes.

## 7.3 Discussion

The goal of the fractal analysis performed on the STARE dataset was primarily focussed on evaluating the potential of FFA and MFA to distinguish between the vasculature in images which had been classified as normal and pathological by the creators of the database. The proposed approach for the calculation of FD of an image using MFA took approximately $3-5$ seconds using a Windows $8$ PC with $2.5$ GHz processor and $6$ GB RAM which is significantly faster than methods previously investigated for retinal imaging [28] [92] [142]. Their approach took approximately $45$ minutes to $1$ hour to calculate fractal dimension (this observation is based on an implementation of the method).

The multifractal behaviour of the retinal vasculature was observed in all images. It was also observed that the images classified as *pathological* have lower generalised dimensions and a shift of the $f(\alpha)$ spectrum in comparison with the *normal* cases. The $f(\alpha)$ spectrum for skeletonised images were found to be narrower as compared to segmented images for both observers. This observation is in agreement with the conclusions made in [28], that fractal analysis after skeletonisation may be more sensitive to changes in vascular patterns. FFA also showed that *pathological* images have lower fractal dimension compared to *normal* cases. A significant difference in the FD of *normal* and *pathological* images was observed using both MFA and FFA techniques. Removal of some junctions and vessels from the segmented images did not hinder the performance of the algorithms as still a significant difference between *normal* and *pathological* groups was observed. Furthermore, the addition of noise did not impede the ability MFA and FFA to detect differences between the two subgroups of images.

In STARE dataset, there was a difference in the level of details in the manual segmentation by two observers (AH and VK). The images segmented by observer VK demonstrates a higher level of detail as compared to observer AH. The MFA performed on both set of images showed a significant difference between two subgroups. For

the comparative analysis, junctions and vessels were removed from STARE images to mimic the varying segmentation to some extent. Dropping out junctions and vessel sections simulates varying image/segmentation quality and implies a certain robustness to FD as a measure.

The retinal blood vessels have same morphological and physiological properties with that of cerebral small vessels [7]. Thus retinal vasculature may act as a surrogate marker for these cerebral small vessels [44][7] [218]. Moreover, the retina reflects pathological changes that occur due to microvascular disease such as stroke [46]. When the region wise MFA was performed on Edinburgh MSS images, the mean FDs were found to be lower in case of lacunar images for the regions where the significant difference were found. The decreased FD represents the decreased branching complexity. As lacunar stroke is related to small vessel disease therefore, the present results (i.e. decreased FD in case of lacunar stroke) reflect that it is so likely that the decreased FD is related to damage of the small vessels in the brain as a result of lacunar stroke.

## 7.4 Conclusions

Distinguishing between the retinal vascular networks of different groups of people in large imaging datasets with varying noise levels requires reliable as well as fast pattern recognition algorithms. Fractal analysis seems to be a robust source of potential biomarkers with a degree of reliance to varying image quality. From the results of the experiments described above, it can be concluded that it is possible to distinguish between the images of subjects which are normal and those which are suffering from any pathological conditions using fractal dimension. Fractal dimensions can be considered as a potential biomarker even in the presence of degrading segmentation quality and noise. MFA approach was very fast to calculate while FFA does not require any prior vessel segmentation.

Similarly, based on the analysis performed, it can safely be concluded that it

is not possible to distinguish between lacunar and cortical stroke based on fractal dimensions obtained from whole retinal vasculature. Whereas, it is possible to distinguish when analysis was performed on different regions of retinal vasculature using MFA. Region wise fractal analysis supported the hypothesis that patients with lacunar stroke will have altered retinal vascular geometry reflecting small vessel disease compared with patients with cortical stroke in specific retinal regions.

# Chapter 8

# Summary and Conclusions

## 8.1 Introduction

In this chapter an overall summary of the research performed, its contributions, the limitations and the possible directions for the future work are presented. Section 8.2 presents a concise summary of each chapter and discusses briefly the major outcomes. Section 8.3 considers the contributions of this thesis while section 8.4 discusses some of the limitations of the developed methodologies. Finally, section 8.5 gives some recommendations for the future extensions of this research.

## 8.2 Summary of achievements and results

The major emphasis of this thesis was to develop an automatic software framework for biomarker identification in large datasets of retinal images. This framework contributes to the VAMPIRE software suite. Two of the main aims of this research were:

1. Develop automatic system for classification of retinal vessels into arterioles and venules in order to aid the identification and quantification of AVR and other

biomarkers.

2. Investigate and implement a novel fractal analysis approach to characterise the state of the retinal vasculature and distinguish between pathological and normal images.

In Chapter 2 the anatomy of the human eye was introduced along with the principal techniques of retinal imaging. This chapter also discussed various abnormalities (i.e. vascular and retinopathy) appearing in the retina, information on which can be exploited to detect the presence of retinal and systemic diseases. The aim of this chapter was to introduce terminology related to the retina and retinal imaging to the reader.

Chapter 3 provided a literature review in the fields of retinal vessel classification, AVR and fractal analysis. This chapter reported different approaches of classifying retinal vessels with different unsupervised and supervised classifier using different features. Diverse approaches and framework on different dataset yielded different set of results. To the best of knowledge the thesis system of vessel classification was the first attempt to categorise vessels using GMM-EMM, SMIC and LS-SVM classifiers. Also, this thesis demonstrated for the first time to classify the retinal vessels using dimensionality reduction techniques like OLPP, MICI and LS. In this chapter three algorithms for the calculation of AVR was also explained. This chapter also provided some of the studies in the past showing how the pathology can affect the retinal vasculature which will in turn alters the FD of pathological images as compared to images acquired from normal cases.

In Chapter 4 the framework and stages of development of both unsupervised and supervised approaches for automated retinal vessel classification in fundus camera images based on colour features were presented. The task of vessel classification was first handled with a GMM-EM unsupervised approach. An improvement in performance was sought by using a SMIC unsupervised classifier. The unsupervised vessel classification framework was tested and validated on different datasets. This chapter then discussed vessel classification with the aid of dimensionality reduction

techniques with the aim of keeping the classification rate as high as possible by using only the dominant distinguishing colour features. A LS-SVM supervised approach for vessel classification was developed to achieve further increase in the classification rate but keeping the processing time as low as possible. This chapter also introduced a method to reduce the number of instances of unclassified vessels.

The mathematical background to two methods of fractal analysis - MFA and FFA was introduced in Chapter 6. These techniques were used to examine whether global or regional changes in vascular network complexity in response to disease were quantifiable. Fractal analysis was explored to investigate its potential to distinguish between retinal images classified as pathological and normal as well as between images from patients with different stroke subtypes (i.e. lacunar and cortical).

In Chapter 5, results obtained by utilising unsupervised and supervised methods for vessel classification on different datasets were detailed. It was observed that among the unsupervised approaches, SMIC outperforms the GMM-EM method on all the tested datasets both in terms of classification accuracy and unclassified vessels in zone B as well as in the extended zone. It was also observed that OLPP outperformed all the tested dimensionality reduction methods. Moreover, the LS-SVM supervised method showed excellent result even with a small set of training images (leading to a short training time). Results obtained by utilising the output of automatic vessel classification in conjunction with three different methods for calculating AVR were also discussed in this chapter. Significant difference between system AVR and ground truth was observed. The accuracy with which vessel's width were measured and/or the number/choice of vessels for AVR calculation might be the reason for this significant difference.

Finally, in chapter 7 the results of fractal analysis performed on two datasets were presented. It was observed that the time taken for the execution of MFA was quite low and that the technique was able to distinguish between the vascular patterns in retinal images previously classified as normal and pathological. MFA was also able to distinguish between subtle differences in the stroke patient images during regional

wise analysis. FFA was able to distinguish between the normal and pathological retinal images but not between the stroke subtypes.

## 8.3 Contributions

The key contributions of the work presented in this thesis are:

1. Automatic retinal vessel classification algorithms for fundus camera images using supervised (LS-SVM) and unsupervised (GMM-EM and SMIC) classifiers was developed and validated on three datasets, two of which were publically available. The LS-SVM classification approach has since been incorporated into the VAMPIRE software suite.

2. Classifying the vessels with the optimal features is likely to impact the classification performance. Therefore, with the aim of classifying the retinal vessels with the most distinctive features, several dimensionality reduction techniques were evaluated.

3. Three different methods of calculating the AVR biomarker were implemented and tested.

4. Two different approaches of calculating fractal dimension (MFA and FFA), were tested to examine whether global or regional changes occurs in the retinal vasculature in presence of disease. The global MFA technique has since been incorporated into VAMPIRE software.

5. Around 2,000 images from the ORCADES dataset were analysed for a large study (funded by the Leverhulme trust) using the best performing vessel classification and fractal analysis methods, and the measurements are undergoing further statistical analysis.

## 8.4 Limitations

There were some limitations associated with the designed automated systems. Some of these, which were acknowledged but could not be addressed within the time frame of this thesis, are described below:

1. The results of automatic vessel classification on the publically available DRIVE and INSPIRE-AVR datasets were presented w.r.t. the labels of only one observer i.e. observer 1. Though the high level of agreement between two observers was demonstrated in section 5.2.1, but it would be interesting to see how classification rate varies w.r.t. labels generated by any other annotator (i.e. other than observer 1).

2. The performance of unsupervised classification was validated on two publically available datasets (i.e. DRIVE and INSPIRE-AVR) whereas the performance of supervised classification was validated on only one (i.e. DRIVE). Further tests on larger banks of images, preferably acquired from subjects presenting different pathologies, is required in order to further establish the suitability of these methods in biomarker research.

3. Fractal analysis was performed on the unclassified, segmented retinal vasculature and not the separated arteriolar and venular components. Different diseases are known to affect these components differently, and so fractal analysis might have been more sensitive to detecting vascular changes if this had been undertaken.

## 8.5 Future work

Besides tackling the unresolved issues discussed in the previous section, there are several ways in which the work of this thesis could be extended. These are described below:

1. Even though results obtained with supervised and unsupervised classification using only the four most dominant colour features were promising, the classification performance was highly dependent on the set of features and its dimensions. Classification performance will vary with different datasets and with different number of features. Hence types of features such as textural-based or morphological-based could be incorporated which may enhance classification performance.

2. The OLPP dimensionality reduction technique in conjunction with GMM-EM classification outperformed all other tested methods for retinal vessel classification, using a set of 47 features. The performance of OLPP with different clustering method(s) using an even larger bank of features presents another opportunity for improving vessel classification.

3. A quadrant-pairwise approach for vessel classification assigns four labels to each pixel from a group of three classes: *arterioles* (*a*), *venules* (*v*) and *not labelled* (*n*). In order to improve classification some additional votes could also be assigned to a centreline pixel. For example by classifying vessels in quadrant wise and/or rotating the coordinate axes of a quadrants several times by some angles.

4. The unsupervised classification algorithms were tested in zone B and an extended zone. The classification rate was found to be lower in the extended zone as compared to zone B. Thus further refinements in the presented vessel classification algorithm are required to make it suitable for vessel classification of the whole visible vasculature. For example incorporating some structural features of retinal vessel such as (1) arteries (or vein) never cross arteries (or veins), (2) a vessel branches into two vessels of the same kind etc.

5. Performance of LS-SVM classification was found to be good even with a relatively small set of training data. Hence annotation of a large number of images to generate training data was not needed. This supervised framework was tested on a publically available dataset and yielded a good classification rate in both zone B and the extended zone. The major drawback of supervised

classification method is the need to retrain the classifier separately for different datasets. Thus, it would be worth exploring how classification performance varies with the classifier trained on one dataset and then applied to another.

6. Fractal analysis was performed on the STARE dataset which contains images of patients with different pathologies that are not well defined or characterised. Further investigations are required to test and validate the performance of fractal analysis on other datasets which contain images with a much more prescriptive categorisation of what they relate to.

7. Fractal analysis was performed on fundus camera images where the retinal vasculature had been segmented but not classified into arterioles and venules. Given that two key outputs from this thesis were automatic vessel classification and regional fractal analysis, the exciting opportunity now exists to combine these into one framework and deliver automatic analysis of the arteriolar and venular components of the retinal vasculature separately and investigate any changes in these in conjunction with systemic diseases.

8. STARE dataset was used to test the stability (with varying segmentation and noise) of fractal analysis. Further study can be carried out to test the stability of fractal analysis using Edinburgh Mild Stroke Study.

9. Extracting and generating a large feature bank that might improve vessel classification is a time consuming and computationally intensive task. Thus to resolve this issue and to reduce the overall computational cost for pixel based classification methods, a more efficient implementation of the feature extraction, feature selection and classification methods in a different high level programming language (e.g. C, C++, or Java) would be beneficial.

10. Classification algorithms were tested on images acquired only from European-based populations. Further tests are required on images acquired from different races and ethnicity to see how the system might be adapted to handle inherent differences in the appearance of the human retina.

11. The designed system was tested on fundus camera images. The applicability of the system to other imaging modalities such as the ultra-widefield or infra-red scanning laser ophthalmoscope can be prospectively explored.

# Bibliography


[1] H. Li, W. Hsu, M. L. Lee, and T. Y. Wong, "Automatic grading of retinal vessel caliber." *IEEE transactions on bio-medical engineering*, vol. 52, no. 7, pp. 1352–5, Jul. 2005. [Online]. Available: http://www.ncbi.nlm.nih.gov/pubmed/16042001

[2] T. Wong, R. Klein, B. Klein, J. Tielsch, L. Hubbard, and F. Nieto, "Retinal microvascular abnormalities and their relationship with hypertension, cardiovascular disease, and mortality," *Survey of ophthalmology*, vol. 46, no. 1, pp. 59–80, 2001. [Online]. Available: http://www.sciencedirect.com/science/article/pii/s003962570100234x

[3] M. D. Abramoff, M. K. Garvin, and M. Sonka, "Retinal imaging and image analysis," *IEEE reviews in biomedical engineering*, vol. 3, pp. 169–208, 2010. [Online]. Available: http://www.ncbi.nlm.nih.gov/pubmed/21904394

[4] S. Van Doornum, G. Strickland, R. Kawasaki, J. Xie, I. P. Wicks, L. a. B. Hodgson, and T. Y. Wong, "Retinal vascular calibre is altered in patients with rheumatoid arthritis: a biomarker of disease activity and cardiovascular risk?" *Rheumatology (Oxford, England)*, vol. 50, no. 5, pp. 939–43, May 2011. [Online]. Available: http://www.ncbi.nlm.nih.gov/pubmed/21172929

[5] R. Chrástek, M. Wolf, K. Donath, H. Niemann, D. Paulus, T. Hothorn, B. Lausen, R. Lämmer, C. Y. Mardin, and G. Michelson, "Automated segmentation of the optic nerve head for diagnosis of glaucoma." *Medical image analysis*, vol. 9, no. 4, pp. 297–314, Aug. 2005. [Online]. Available: http://www.ncbi.nlm.nih.gov/pubmed/15950894

[6] Q. Mirsharif, F. Tajeripour, and . H. Pourreza, "Automated characterization of blood vessels as arteries and veins in retinal images," *Computerized Medical Imaging and Graphics*, vol. 37, pp. 607–617, 2013.

[7] N. Patton, T. Aslam, T. Macgillivray, A. Pattie, I. J. Deary, and B. Dhillon, "Retinal vascular image analysis as a potential screening tool for cerebrovascular disease: a rationale based on homology between cerebral and retinal microvasculatures." *Journal of anatomy*, vol. 206, no. 4, pp. 319–48, Apr. 2005. [Online]. Available: http://www.pubmedcentral.nih.gov/articlerender.fcgi?artid=1571489&tool=pmcentrez&rendertype=abstract

[8] R. Klein, B. Klein, and S. Moss, "The relation of systemic hypertension to changes in the retinal vasculature: the beaver dam eye study," *Trans Am Ophthalmol*, pp. 329–48, 1997.

[9] R. Klein, B. Klein, S. Moss, and Q. Wang, "Hypertension and retinopathy, arteriolar narrowing, and arteriovenous nicking in a population." *Arch Ophthalmol*, vol. 112, pp. 92–8, 1994.

[10] M. Hanafi, A. Hijazi, F. Coenen, and Y. Zheng, "Retinal Image Classification for the Screening of Age-related Macular Degeneration," *Chapter: Research and Development in Intelligent Systems XXVII*, pp. 325–338.

[11] L. Giancardo, "Quality Analysis of Retina Images for the Automatic Diagnosis of Diabetic Retinopathy," Ph.D. dissertation, 2008.

[12] A. Perez-Rovira, T. MacGillivray, E. Trucco, K. S. Chin, K. Zutis, C. Lupascu, D. Tegolo, a. Giachetti, P. J. Wilson, a. Doney, and B. Dhillon, "VAMPIRE: Vessel assessment and measurement platform for images of the REtina." *Annual International Conference of the IEEE Engineering in Medicine and Biology Society*, vol. 2011, pp. 3391–4, Jan. 2011. [Online]. Available: http://www.ncbi.nlm.nih.gov/pubmed/22255067

[13] E. D. Kurniawan, N. Cheung, and et al., "Elevated blood pressure is associated with rarefaction of the retinal vasculature in children," *Investigative Ophthalmology & Visual Science*, vol. 53, no. 1, pp. 470–4, 2012.

[14] M. K. Ikram, J. C. M. Witteman, J. R. Vingerling, M. M. B. Breteler, A. Hofman, and P. T. V. M. de Jong, "Retinal vessel diameters and risk of hypertension: the Rotterdam Study." *Hypertension*, vol. 47, no. 2, pp. 189–94, Feb. 2006. [Online]. Available: http://www.ncbi.nlm.nih.gov/pubmed/16380526

[15] F. Doubal, P. Hokke, and J. Wardlaw, "Retinal microvascular abnormalities and stroke - a systematic review," *J. Neurol. Neurosurg Psychiatry,*, vol. 80, no. 2, pp. 158–165, 2009.

[16] J. Ding, N. Patton, I. J. Deary, M. W. Strachan, F. G. Fowkes, R. J. Mitchell, and J. F. Price, "Retinal microvascular abnormalities and cognitive dysfunction: a systematic review," *Brit. J. Ophth*, vol. 92, no. 8, pp. 1017–1025, 2008.

[17] X. Xu, "Automated delineation and quantitative analysis of blood vessels in retinal fundus image," *Ph.D. dissertation*, 2012.

[18] S. R. Nirmala, M. K. Nath, and S. Dandapat, "Retinal Image Analysis : A Review," *International Journal of Computer & Communication Technology (IJCCT)*, vol. 2,, no. VI, pp. 11–15, 2011.

[19] C. Sun, G. Liew, J. J. Wang, P. Mitchell, S. M. Saw, T. Aung, E. S. Tai, and T. Y. Wong, "Retinal vascular caliber, blood pressure, and cardiovascular risk factors in an Asian population: the Singapore Malay Eye Study." *Investigative ophthalmology & visual science*, vol. 49, no. 5, pp. 1784–90, May 2008. [Online]. Available: http://www.ncbi.nlm.nih.gov/pubmed/18436813

[20] T. Y. Wong, F. M. A. Islam, R. Klein, B. E. K. Klein, M. F. Cotch, C. Castro, a. R. Sharrett, and E. Shahar, "Retinal vascular caliber, cardiovascular risk factors, and inflammation: the multi-ethnic study of atherosclerosis (MESA)." *Investigative ophthalmology & visual science*, vol. 47, no. 6, pp. 2341–50, Jun. 2006. [Online]. Available: http://www.pubmedcentral.nih.gov/articlerender.fcgi?artid=2258139&tool=pmcentrez&rendertype=abstract

[21] N. Patton, T. M. Aslam, T. MacGillivray, I. J. Deary, B. Dhillon, R. H. Eikelboom, K. Yogesan, and I. J. Constable, "Retinal image analysis: concepts, applications and potential." *Progress in Retinal and Eye Research*, vol. 25, no. 1, pp. 99–127, Jan. 2006. [Online]. Available: http://www.ncbi.nlm.nih.gov/pubmed/16154379

[22] T. Y.Wong, R. Klein, A. R. Sharrett, B. B. Duncan, D. J. Couper, J. M. Tielsch, B. E. K. Klein, and L. D. Hubbard, "Retinal arteriolar narrowing and risk of coronary heart disease in men and women," *JAMA*, vol. 287, no. 9, pp. 1153–1159, 2002.

[23] C. Sun, J. J. Wang, D. A. Mackey, and T. Y. Wong, "Retinal vascular caliber: systemic, environmental, and genetic associations." *Survey of Ophthalmology*, vol. 54, no. 1, pp. 74–95, 2009. [Online]. Available: http://www.ncbi.nlm.nih.gov/pubmed/19171211

[24] J. C. Parr and G. F. S. Spears, "Mathematic relationship between the width of a retinal artery and the width of its branches," *Am. J. Ophthalmol*, vol. 77, no. 4, pp. 478–483, 1974.

[25] T. Y. Wong, M. D. Knudtson, R. Klein, B. E. K. Klein, S. M. Meuer, and L. D. Hubbard, "Computer-assisted measurement of retinal vessel diameters in the Beaver Dam Eye Study: methodology, correlation between eyes, and effect of refractive errors." *Ophthalmology*, vol. 111, no. 6, pp. 1183–90, Jun. 2004. [Online]. Available: http://www.ncbi.nlm.nih.gov/pubmed/15177969

[26] F. de Jong, E. Schrijvers, M. Ikram, P. Koudstaal, P. de Jong, A. Hofman, J. Vingerling, and M. M. Breteler, "Retinal vascular caliber and risk of dementia: the rotterdam study." *Neurology*, vol. 76, no. 9, pp. 816–21, 2011.

[27] S. Talu and S. Giovanzana, "Image analysis of the normal human retinal vasculature using fractal geometry," *Human and Veterinary Medicine Bioflux*, vol. 4, no. 1, pp. 14–18, 2012.

[28] T. Stosić and B. D. Stosić, "Multifractal analysis of human retinal vessels." *IEEE transactions on medical imaging*, vol. 25, no. 8, pp. 1101–7, Aug. 2006. [Online]. Available: http://www.ncbi.nlm.nih.gov/pubmed/16895002

[29] N. Cheung and et al, "Quantitative assessment of early diabetic retinopathy using fractal analysis," *DIABETES CARE*, vol. 32, pp. 106–110, January 2009.

[30] G. Liew, P. Mitchell, E. Rochtchina, T. Y. Wong, W. Hsu, M. L. Lee, A. Wainwright, and J. J. Wang, "Fractal analysis of retinal

microvasculature and coronary heart disease mortality." *European heart journal*, vol. 32, no. 4, pp. 422–9, Feb. 2011. [Online]. Available: http://www.ncbi.nlm.nih.gov/pubmed/21138936

[31] W. E. Hart, M. Goldbaum, B. Côté, P. Kube, and M. R. Nelson, "Measurement and classification of retinal vascular tortuosity." *International journal of medical informatics*, vol. 53, no. 2-3, pp. 239–52, 1999. [Online]. Available: http://www.ncbi.nlm.nih.gov/pubmed/10193892

[32] Y. Jiang and A. B. Morris, "Blood vessel tracking in retinal images," *Proceedings of Image and Vision Computing New Zealand*, vol. 1, no. December, pp. 126–131, 2007.

[33] C. Kondermann, D. Kondermann, and M. Yan, "Blood vessel classification into arteries and veins in retinal images," *Proceedings of SPIE*, vol. 6512, 2007. [Online]. Available: http://link.aip.org/link/PSISDG/v6512/i1/p651247/s1&Agg=doi

[34] M. Niemeijer, B. van Ginneken, and M. D. Abramoff, "Automatic classification of retinal vessels into arteries and veins," *Proceedings of SPIE*, vol. 7260, pp. 72 601F–72 601F–8, 2009. [Online]. Available: http://link.aip.org/link/PSISDG/v7260/i1/p72601F/s1&Agg=doi

[35] H. Narasimha-Iyer, J. M. Beach, B. Khoobehi, and B. Roysam, "Automatic identification of retinal arteries and veins from dual-wavelength images using structural and functional features." *IEEE transactions on bio-medical engineering*, vol. 54, no. 8, pp. 1427–35, Aug. 2007. [Online]. Available: http://www.ncbi.nlm.nih.gov/pubmed/17694863

[36] "Anatomy of eye," http://www.larsoneyecenter.com/chicago/patient-education/anatomy-of-the-eye.htm.

[37] "Layers of the retina," http://www.ncbi.nlm.nih.gov/books/NBK10885/.

[38] "Structure of the retina," www.studydroid.com/printerFriendlyViewPack.php?packId=293951.

[39] X. Xu, "Automated delineation and quantitative analysis of blood vessels in retinal fundus image." Ph.D. dissertation, University of Iowa, 2012.

[40] K. S. Chin, "Computer-assisted colour fundus image analysis 2011," Master's thesis, University of Dundee, U.K, 2011.

[41] T. MacGillivray, E. Trucco, J. Cameron, B. Dhillon, J. Houston, and E. van Beek, "Retinal imaging as a source of biomarkers for diagnosis, characterization and prognosis of chronic illness or long-term conditions," *British journal of Radiology*, vol. 87(1040), 2014.

[42] "Anatomy of retina," http://webvision.med.utah.edu/book/part-i-foundations/simple-anatomy-of-the-retina/.

[43] G. Liew and J. J. Wang, "Retinal Vascular Signs: A Window to the Heart?" *Revista Española de Cardiología (English Edition)*, vol. 64, no. 6, pp. 515–521, Jun. 2011. [Online]. Available: http://linkinghub.elsevier.com/retrieve/pii/S1885585711002738

[44] F. N. Doubal, "Do retinal microvascular abnormalities shed light on the pathophysiology of lacunar stroke ? Doctor of Philosophy," 2010.

[45] T. Yu, P. Mitchell, G. Berry, and et al, "Retinopathy in older persons without diabetes and its relationship to hypertension." *Arch Ophthalmol*, vol. 116, pp. 83–9, 1998.

[46] M. Baker, P.J.Hand, J.J.Wang, and T. Wong, "Retinal signs and stroke: revisiting the link between the eye and brain." *Stroke*, vol. 39, pp. 1371–1379, 2008.

[47] S. Frost, Y. Kanagasingam, H. Sohrabi, J. Vignarajan, P. Bourgeat, O. Salvado, V. Villemagne, C. C. Rowe, and et al., "Retinal vascular biomarkers for early detection and monitoring of alzheimers disease," *Translational Psychiatry*, vol. 3(2), 2013.

[48] G. Liew, J. J. Wang, P. Mitchell, and T. Y. Wong, "Retinal vascular imaging: a new tool in microvascular disease research." *Circulation. Cardiovascular imaging*, vol. 1, no. 2, pp. 156–61, Sep. 2008. [Online]. Available: http://www.ncbi.nlm.nih.gov/pubmed/19808533

[49] T. Y. Wong, A. Shankar, R. Klein, B. E. K. Klein, and L. D. Hubbard, "Prospective cohort study of retinal vessel diameters and risk of hypertension." *BMJ (Clinical research ed.)*, vol. 329, no. 7457, p. 79, Jul. 2004. [Online]. Available: http://www.pubmedcentral.nih.gov/articlerender.fcgi?artid=449809&tool=pmcentrez&rendertype=abstract

[50] H. Leung, "Relationships between age, blood pressure, and retinal vessel diameters in an older population," *Investigative Ophthalmology & Visual Science*, vol. 44, no. 7, pp. 2900–2904, Jul. 2003. [Online]. Available: http://www.iovs.org/cgi/doi/10.1167/iovs.02-1114

[51] B. Dashtbozorg, A. Mendonca, and A. Campilho, "An automatic graph-based approach for artery/vein classification in retinal images," *IEEE Transactions on Image Processing*, pp. 1–10, 2013.

[52] E. Trucco, L. Ballerini, A. Giachetti, D. Relan, T. Macgillivray, K. Zutis, and et al., "Novel VAMPIRE Algorithms for Quantitative Analysis of the retinal vasculature," *Biosignals and Biorobotics Conference (BRC), Rio de Janerio*, pp. 1–4, 2013.

[53] A. M. Miller, "Eyewiki," *http://eyewiki.aao.org/Fluorescein Angiography*, 2012.

[54] R. Webb and G. Hughes, "Scanning laser ophthalmoscope," *IEEE Transaction on Biomedical Engineering*, vol. vol. 28, no. 7, pp. 488–492, 1981.

[55] "Fluorescein angiogram," http://www.medicine.uiowa.edu/eye/fluoresceinangiography/.

[56] T. J. Bennett, "Scanning laser ophthalmoscopy," http://www.opsweb.org/?page=SLO.

[57] "Slo image," https://www.optos.com/en-US/Products/Retinal-imaging-products/Retinal-imaging-products/Ophthalmoscopy/.

[58] J. G. Fujimoto, C. Pitris, and S. A. B. et al, "Optical coherence tomography: An emerging technology for biomedical imaging and optical biopsy," *Neoplasia.*, vol. 2, no. 1-2, pp. 9–25, Jan 2000.

[59] M. Hee, J. Izatt, and E. S. et al, "Optical coherence tomography of the human retina," *Arch Ophthalmol.*, vol. 113, pp. 325–332., 1995.

[60] M. Hee, C. Puliafito, and e. a. Wong C, "Optical coherence tomography of macular holes." *Ophthalmology.*, vol. 102, pp. 748–756., 1995.

[61] M. H. anda CA Puliafito CA and C. W. et al, "Optical coherence tomography of central serous chorioretinopathy." *Am J Ophthalmol.*, vol. 120, pp. 65–74, 1995.

[62] M. Hee, C. Puliafito, and C. W. et al, "Quantitative assessment of macular edema with optical coherence tomography." *Arch Ophthalmol.*, vol. 113, pp. 1019–1029., 1995.

[63] M. Hee, C. Baumal, and C. P. et al Ophthalmology., "Optical coherence tomography of age-related macular degeneration and choroidal neovascularization." *1996*, vol. 103, pp. 1260–1270.

[64] D. K. D, R. Gentile, and J. L. al, "Imaging congenital optic disc pits and associated maculopathy using optical coherence tomography." *Arch Ophthalmol.*, vol. 114, pp. 165–170, 1996.

[65] H. Lincoff and I. Kreissig, "Optical coherence tomography of pneumatic displacement of optic disc pit aculopathy." *Br J Ophthalmol.*, vol. 82, pp. 367–372, 1998.

[66] U. Schaudig, A. Hassenstein, and A. B. et al, "Limitations of imaging choroidal tumors in vivo by optical coherence tomography." *Graefe's Arch Clin Exp Ophthalmol.*, vol. 236, pp. 588–592., 1998.

[67] "Oct image," http://multiple-sclerosis-research.blogspot.com/2012/10/the-eye-window-to-brain.html.

[68] H. Jelinek and M. Cree, "Automated image detection of retinal pathology," *Book publiser: CRC Press*, 2010.

[69] E. Grisan, "Automatic analysis of retinal images : Retinopathy detection and grading," Ph.D. dissertation, University of Padova, 2005.

[70] E. Grisan and a. Ruggeri, "A divide et impera strategy for automatic classification of retinal vessels into arteries and veins," *Proceedings of the 25th Annual International Conference of the IEEE Engineering in Medicine and Biology Society (IEEE Cat. No.03CH37439)*, pp. 890–893, 2003. [Online]. Available: http://ieeexplore.ieee.org/lpdocs/epic03/wrapper.htm?arnumber=1279908

[71] "Focal arteriolar narrowing," http://www.revespcardiol.org/en/retinal-vascular-signs-a-window/articulo/90020937/.

[72] M. Sasongko, J. Wang, K. Donaghue, N. Cheung, P. Benitez-Aguirre, A. Jenkins, W. Hsu, M. Lee, and T. Wong, "Alterations in retinal microvascular geometry in young type 1 diabetes," *DIABETES CARE*, vol. 33, no. 6, pp. 1332–1336, 2010.

[73] N. Chapman, G. Dellomo, M. Sartini, N. Witt, A. Hughes, S. Thom, and R. Pedrinelli, "Peripheral vascular disease is associated with abnormal arteriolar diameter relationships at bifurcations in the human retina," *Clin Sci (Lond)*, vol. 103, no. 2, pp. 111–6, 2002.

[74] V. S. Joshi, "Analysis of retinal vessel networks using quantitative descriptors of vascular morphology," *PhD Dissertation*, 2012.

[75] F. Doubal, T. MacGillivray, N. Patton, and et al., "Fractal analysis of retinal vessels suggests that a distinct vasculopathy causes lacunar stroke," *Neurology*, vol. 74, no. 14, pp. 1102– 1107, 2010.

[76] F. Doubal, H. R. de, T. J. MacGillivray, P. Cohn-Hokke, B. D. B, M. S. Dennis, and J. M. Wardlaw, "Retinal arteriolar geometry is associated with cerebral white matter hyperintensities on magnetic resonance imaging." *Int J Stroke*, pp. 434–9., 2010.

[77] M. M. Zamir and J. Cunningham, "Arterial bifurcations in the human retina," *J. Gen. Physiol.*, vol. 74, pp. 537–548, 1979.

[78] L. D. Hubbard, R. J. Brothers, W. N. King, L. X. Clegg, R. Klein, L. S. Cooper, a. R. Sharrett, M. D. Davis, and J. Cai, "Methods for evaluation of retinal microvascular abnormalities associated with hypertension/sclerosis in the Atherosclerosis Risk in Communities Study." *Ophthalmology*, vol. 106, no. 12, pp. 2269–80, Dec. 1999. [Online]. Available: http://www.ncbi.nlm.nih.gov/pubmed/10599656

[79] "Gunns sign," http://optometrytimes.modernmedicine.com/optometrytimes/content/tags/chronic-hypertensive-choroidopathy/ocular-manifestations-systemic-hypert?page=full.

[80] "Salus's signs," http://bdweb9051f1.bluedomino.com/retina-abnormality.htm.

[81] T. Wong, R. Klein, and C. D. et al., "Retinal microvascular abnormalities and incident strokes: the atherosclerosis risk in the communities study." *Lancet*, vol. 358, no. 1134 - 1140, 2001.

[82] N. Cheung and T. Y. Wong, "The retinal arteriole to venule ratio: informative or deceptive?" *Graefe Archive for Clinical and Experimental Ophthalmology*, vol. 245, no. 1245-1246, 2007.

[83] G. Liew, P. Mitchell, J. Wang, and T. Wong, "Effect of axial length on retinal vascular network geometry," *Am J Ophthalmol*, vol. 141, no. 597-598, March 2006.

[84] H.-C. Chen, "Vascular complications of diabetes; current issues in pathogenesis and treatment,," *chapter 10*.

[85] J. A. Lowell, "Automated retinal analysis," *Doctoral thesis, Durham University*, 2006.

[86] "Retinapathy," http://www.mohaneyeinstitute.org/retina/diabetic-retinopathy.html.

[87] "Cotton-wool spot," http://www.pitt.edu/~super1/lecture/lec45171/027.htm.

[88] "Soft and hard drusen," http://www.illinoisretinainstitute.com/index.php?p=1_12.

[89] V. B. Soares, J. J. G. Leandro, R. M, H. F. Jelinek, and M. J. Cree, "Retinal vessel segmentation using the 2-D Gabor wavelet and supervised classification." *IEEE transactions on medical imaging*, vol. 25, no. 9, pp. 1214–22, Sep. 2006. [Online]. Available: http://www.ncbi.nlm.nih.gov/pubmed/16967806

[90] S.S.Tiew, A.Perez-Rovirez, E. Trucco, S. Mahmood, P. Bishop, and T. M. Aslam, "Experience in using the vampire retinal analysis tool to assess tortuosity in patients undergoing bevacizumab (avastin) treatment for wet age-related macular degeneration (amd)," *Proc ARVO (Assoc for Research in Vision and Ophthalmology) Annual Meeting Fort Lauderdale (USA),*, 2011.

[91] J. Ding, M. Strachan, R. Reynolds, and et al., "Diabetic retinopathy and cognitive decline in older people with type 2 diabetes: the edinburgh type 2 diabetes study." *Diabetes*, vol. 11, no. 59, pp. 2883–9, 2010.

[92] T. J. Macgillivray, F. N. Doubal, N. Patton, C. Graham, and J. M. Wardlaw, "Comparing Monofractal and Multifractal Analysis of the Human Retinal Vasculature," *Clinical Research*, vol. 1, pp. 0–4.

[93] F. N. Doubal, T. J.MacGillivray, P. E. Hokke, B. Dhillon, M. S. Dennis, and J. M. Wardlaw, "Differences in retinal vessels support a distinct vasculopathy causing lacunar stroke." *Neurology*, vol. 72, no. 1773 1778, 2009.

[94] A. Giachetti, L. Ballerini, E. Trucco, and P. J. Wilson, "The use of radial symmetry to localize retinal landmarks," *Computerized Medical Imaging and Graphics*, vol. 37, no. 5-6, pp. 369–376, 2013.

[95] A. Giachett, L. Ballerini, and E. Trucco, "Accurate and reliable segmentation of the optic disc in digital fundus images," *Journal of Medical Imaging'*, vol. 1, no. 2, 2014.

[96] C. A. Lupascu, D. Tegolo, and E. Trucco, "Accurate estimation of retinal vessel width using bagged decision trees and an extended multiresolution hermite model." *Medical Image Analysis*, vol. 17, no. 8, pp. 1164–1180, 2013.

[97] A. Lisowska, R. Annunziata, E. Trucco, D. Karl, and G. Loh, "An experimental assessment of five indices of retinal vessel tortuosity with the ret-tort public dataset," *36th Annual International Conference of the IEEE Engineering in Medicine and Biology Society (EMBC'14), Chicago, Illinois, USA.*

[98] E. Grisan, M. Foracchia, and A. Ruggeri, "A novel method for the automatic grading of retinal vessel tortuosity," *IEEE Transactions on Medical Imaging*, vol. 27, no. 310-319, 2008.

[99] R. Annunziata, A. Kheirkhah, S. Aggarwal, B. Cavalcanti, P. Hamrah, and E. Trucco, "Tortuosity classification of corneal nerves images using a multiple-scale-multiple-window approach," *Proceedings of the Ophthalmic Medical Image Analysis (OMIA) First International Workshop, MICCAI 2014*, pp. 113–120.

[100] R. Annunziata, A. Kheirkhah, S. Aggarwal, B. M.Cavalcanti, P. H. P, and E. Trucco, "Two-dimensional plane for multi-scale quantification of corneal subbasal nerve tortuosity," *Investigative Ophthalmology and Visual Science (in press).*, vol. 57(3), pp. 1132–9, 2016.

[101] "Clustering and classification," http://www.taborcommunications.com/dsstar/00/0704/101861.html.

[102] A. H. Fielding, *Cluster and Classification Techniques for the Biosciences*. Cambridge University Press.

[103] P. Arabie, L. J. Hubert, and G. D. Soete, Eds., *Clustering and Classification*. World Scientific.

[104] J. V. Ryzin, Ed., *Classification and Clustering*. Proceedings of an Advanced Seminar Conducted by the Mathematics Research Center, the University of Wisconsin-Madison, May, 1976.

[105] Jajuga, Krzystof, Sokolowski, Andrzej, Bock, and Hans-Herman, Eds., *Classification, Clustering, and Data Analysis*. Springer-Verlag Berlin Heidelberg, 2002.

[106] L. Vander Maaten, E. Postma, and J. van den Herik, "Dimensionality reduction: A comparative review." *Journal of Machine Learning Research*, vol. 10, pp. 1–41, January 2009.

[107] C. J. C. Burges, "Dimension reduction: A guided tour," *Foundations and Trends in Machine Learning*, vol. 2, no. 4, pp. 275–364., 2009.

[108] "Supervised and unsupervised learning," http://www.astro.caltech.edu/~george/aybi199/Donalek_Classif.pdf.

[109] L. Guerra, L. M. McGarry, V. Robles, and C. B. et al., "Comparison between supervised and unsupervised classifications of neuronal cell types: A case study," *Neurobiology*, vol. 71, no. 1, pp. 71 – 82, 2010.

[110] "Rgb colour space," https://en.wikipedia.org/wiki/RGB_color_model.

[111] "Rgb colour space," http://www.rapidtables.com/web/color/RGB_Color.htm.

[112] "Hsv colour space," http://desktoppub.about.com/od/glossary/g/HSV.htm.

[113] "Hsi colour space," http://www.lps.usp.br/hae/apostila/basico/HSI-wikipedia.pdf.

[114] "Lab colour space," https://en.wikipedia.org/wiki/Lab_color_space.

[115] "Lab colour space," http://www.colourphil.co.uk/lab_lch_colour_space.shtml.

[116] L. Tramontan, E. Grisan, and A. Ruggeri, "An improved system for the automatic estimation of the Arteriolar-to-Venular diameter Ratio (AVR) in retinal images." *Conference proceedings : Annual International Conference of the IEEE Engineering in Medicine and Biology Society. IEEE Engineering in Medicine and Biology Society. Conference*, vol. 2008, pp. 3550–3, Jan. 2008. [Online]. Available: http://www.ncbi.nlm.nih.gov/pubmed/19163475

[117] M. Saez, S. González-Vázquez, M. González-Penedo, M. A. Barceló, M. Pena-Seijo, G. Coll de Tuero, and A. Pose-Reino, "Development of an automated system to classify retinal vessels into arteries and veins." *Computer methods and programs in biomedicine*, pp. 1–10, Mar. 2012. [Online]. Available: http://www.ncbi.nlm.nih.gov/pubmed/22424729

[118] S. G. Vazquez, B. Cancela, N. Barreira, M. G. Penedo, and M. Saez, "On the Automatic Computation of the Arterio-Venous Ratio in Retinal Images: Using Minimal Paths for the Artery/Vein Classification," *2010 International Conference on Digital Image Computing: Techniques and Applications*, pp. 599–604, Dec. 2010. [Online]. Available: http://ieeexplore.ieee.org/lpdocs/epic03/wrapper.htm?arnumber=5692627

[119] W. M. B. W. Mohd, A. Beg, T. Herawan, A. Noraziah, and K. F. Rabbi, "Improved parameterless k-means: Auto-generation centroids and distance data point clusters," *International Journal of Information Retrieval Research (IJIRR)*, vol. 1, no. 3.

[120] C. M. Bishop, "Pattern recognition and machine learning," *Springer*.

[121] V. S. Joshi, M. K. Garvin, J. M. Reinhardt, and M. D. Abramoff, "Automated artery-venous classification of retinal blood vessels based on structural mapping method," vol. 8315, pp. 83 151C–83 151C–8, 2012. [Online]. Available: http://link.aip.org/link/PSISDG/v8315/i1/p83151C/s1&Agg=doi

[122] M. Niemeijer, X. Xu, A. V. Dumitrescu, P. Gupta, B. van Ginneken, J. C. Folk, and M. D. Abramoff, "Automated measurement of the arteriolar-to-venular width ratio in digital color fundus photographs." *IEEE transactions on medical imaging*, vol. 30, no. 11, pp. 1941–50, Nov. 2011. [Online]. Available: http://www.ncbi.nlm.nih.gov/pubmed/21690008

[123] A. Zamperini and A. Giachetti, "Effective features for artery-vein classification in digital fundus images," *25th International Symposium on Computer-Based Medical Systems (CBMS)*, 2012. [Online]. Available: http://ieeexplore.ieee.org/xpls/abs_all.jsp?arnumber=6266336

[124] C. Muramatsu, Y. Hatanaka, T. Iwase, T. Hara, and H. Fujita, "Automated selection of major arteries and veins for measurement of arteriolar-to-venular diameter ratio on retinal fundus images." *Computerized medical imaging and graphics*, vol. 35, no. 6, pp. 472–80, Sep. 2011. [Online]. Available: http://www.ncbi.nlm.nih.gov/pubmed/21489750

[125] H. Narasimha-Iyer, J. M. Beach, B. Khoobehi, J. Ning, H. Kawano, and B. Roysam, "Algorithms for automated oximetry along the retinal vascular tree from dual-wavelength fundus images," *J. Biomed. Opt.*, vol. 10, no. 5, Oct. 2005.

[126] N. Patton, T. Aslam, T. Macgillivray, B. Dhillon, and I. Constable, "Asymmetry of retinal arteriolar branch widths at junctions affects ability of formulae to predict trunk arteriolar widths." *Investigative ophthalmology & visual science*, vol. 47, no. 4, pp. 1329–33, Apr. 2006. [Online]. Available: http://www.ncbi.nlm.nih.gov/pubmed/16565364

[127] M. D. Knudtson, K. E. Lee, L. D. Hubbard, T. Y.Wong, R. Klein, and B. E. K. Klein, "Revised formulas for summarizing retinal vessel diameters," *Current Eye Research*, vol. 27, no. 3, pp. 143–149, 2003.

[128] M. C, "The physiological principle of minimum work 1. the vascular system and the cost of blood volume." *Proc Natl Acad Sci USA.*, vol. 12, pp. 207–214., 1926.

[129] K. A. Goatman, A. D. Fleming, J. A. Olson, and P. F. Sharp, "Automated measurement of generalised retinal vessel narrowing," *Conference : Medical Image Understanding and Analysis, University of Bristol*, July 2005.

[130] V. Hemminki, M.Kähönen, and M. et al., "Determination of retinal blood vessel diameters and arteriovenous ratios in systemic hypertension: comparison of different calculation formulae." *Graefes Arch Clin Exp Ophthalmol*, vol. 17, pp. 245–248, 2007.

[131] P. Mitchell, J. Wang, T. Wong, W. Smith, R. Klein, and S. Leeder, "Retinal microvascular signs and risk of stroke and stroke mortality." *Neurology*, vol. 65, pp. 1005 –1009, 2005.

[132] W. J. Longstreth, E. Larsen, and R. K. et al., "Associations between findings on cranial magnetic resonance imaging and retinal photography in the elderly: the cardiovascular health study." *Am J Epidemiol*, vol. 165, pp. 78–84, 2007.

[133] L. Cooper, T. Wong, and e. a. R. Klein, "Retinal microvascular abnormalities and mri-defined subclinical cerebral infarction: the atherosclerosis risk in communities study." *Stoke*, vol. 37, pp. 82–86, 2006.

[134] C. Y.-L. Cheung, W. Hsu, M. L. Lee, J. J. Wang, P. Mitchell, Q. P. Lau, H. Hamzah, M. Ho, and T. Y. Wong, "A new method to measure peripheral retinal vascular caliber over an extended area." *Microcirculation (New York, N.Y. : 1994)*, vol. 17, no. 7, pp. 495–503, Oct. 2010. [Online]. Available: http://www.ncbi.nlm.nih.gov/pubmed/21040115

[135] A. Avakian, R. E. Kalina, H. E. Sage, A. H. Rambhia, K. E. Elliott, E. L. Chuang, J. I. Clark, J.-N. Hwang, and P. Parsons-Wingerter, "Fractal analysis of region-based vascular change in the normal and non-proliferative diabetic retina," *Curr. Eye. Res*, vol. 24, pp. 274–280.

[136] M. Z. C. Azemin, D. K. Kumar, and e. a. T. Y. Wong, "Age-related rarefaction in the fractal dimension of retinal vessel," *Neurobiology of Aging*, vol. 33, pp. 194.e1–194.e4, 2012.

[137] G. Liew, J. J. Wang, N. Cheung, Y. P. Zhang, W. Hsu, M. L. Lee, P. Mitchell, G. Tikellis, B. Taylor, and T. Y. Wong, "The retinal vasculature as a fractal: methodology, reliability, and relationship to blood pressure." *Ophthalmology*, vol. 115, no. 11, pp. 1951–6, Nov. 2008. [Online]. Available: http://www.ncbi.nlm.nih.gov/pubmed/18692247

[138] "Box-counting method," http://rsb.info.nih.gov/ij/plugins/fraclac/FLHelp/BoxCounting.htm.

[139] "Box-counting method," http://www.wahl.org/fe/HTML_version/link/FE4W/c4.htm#box.

[140] "Box-counting mathod," http://users.math.yale.edu/public_html/People/frame/Fractals/.

[141] M. Kruk, B. Swiderski, and S. Osowski, "Box-counting fractal dimension in application to recognition of hypertension through the retinal image analysis," *Przeglad Elektrotechniczny*, vol. 89(9), pp. 286–289, 2013.

[142] W. O. C. Ward. and L. Bai, "Multifractal analysis of microvasculature in health and disease," *Annual International Conference of the IEEE Engineering in Medicine and Biology Society*, pp. 2336 – 2339, 2013.

[143] "The structured analysis of the retina (stare) project:," www.parl.clemson.edu/stare/probing.

[144] J. Wardlaw, "What causes lacunar stroke?" *Journal of Neurology, Neurosurgery, and Psychiatry*, vol. 76, no. 5, pp. 617–619, 2005.

[145] A. H. Cho, D. W. Kang, S. Kwon, and J. Kim, "Is 15 mm size criterion for lacunar infarction still valid? a study on strictly subcortical middle cerebral artery territory infarction using diffusion-weighted mri." *Cerebrovasc Dis*, vol. 23, pp. 14–19, 2007.

[146] B. Aliahmad, D. K. Kumar, H. Hao, P. Unnikrishnan, M. Z. C. Azemin, R. Kawasaki, and P. Mitchell., "Zone specific fractal dimension of retinal images as predictor of stroke incidence," *Hindawi Publishing Corporation, The Scientific World Journal*, vol. 2014, 2014.

[147] R. Kawasaki, M. Z. C. Azemin, D. K. Kumar, and et al., "Fractal dimension of the retinal vasculature and risk of stroke: a nested case-control study." *Neurology*, vol. 76, no. 20, pp. 1766–1767, 2011.

[148] J. Berke, "Using spectral fractal dimension in image classification," *Innovations and Advances in Computer Sciences and Engineering. Springer science+Business Media B.V. 2010*.

[149] M. Z. C. Azemin, D. K. Kumar, and e. a. T. Y. Wong, "Fusion of multiscale wavelet-based fractal analysis on retina image for stroke prediction," *32nd Annual International Conference of the IEEE EMBS Buenos Aires, Argentina.*, pp. 4308–11, 2010.

[150] J. C. Russ, "Fractal surfaces," *Plenum Press, New York*, 1994.

[151] J. A. Loaiza, "Experimental demonstration of the fractal nature of unstable-resonator modes," *Ph.D. Leiden: Leiden University*, 2005.

[152] M. Z. C. Azemin, D. K. Kumar, and T. Y. W. et al., "Robust methodology for fractal analysis of the retinal vasculature," *IEEE Transactions on Medical Imaging*, vol. 30, no. 2, pp. 243 – 250, 2011.

[153] M. Pechenizkiy, A. Tsymbal, and S. Puuronen, "PCA-based Feature Transformation for Classification," *Proceedings of the 17th IEEE Symposium on Computer-Based Medical Systems (CBMS-04)*, pp. 1–5, 2004.

[154] "Gaussian mixture model," http://home.deib.polimi.it/matteucc/Clustering/tutorial-html/mixture.html.

[155] J. W. Yoon, "An efficient model selection for gaussian mixture model in a bayesian framework," *EEE SIGNAL PROCESSING LETTER*, 2013.

[156] J. A. Bilmes, "A gentle tutorial of the em algorithm and its application to parameter estimation for gaussian mixture and hidden markov models," *International Computer Science Institute Berkeley CA, 94704 and Computer Science Division*.

[157] M. Sugiyama and et al., "Information-maximization clustering based on squared-loss mutual information," *Massachusetts Institute of Technology press Journal*, vol. 26, no. 1, pp. 84–131, January 2014.

[158] "Kmeans clustering." https://en.wikipedia.org/wiki/K-means-clustering.

[159] F. Agakov and D. Barber, *Kernelized infomax clustering*, ser. Advances in Neural Information Processing Systems 18, Y.Weiss, B. Scholkopf, and J. Platt, Eds. MIT Press, Cambridge, MA, USA, 2006.

[160] G. H. Golub and C. F. V. Loan, *Matrix Computations*. Johns Hopkins University Press, Baltimore, MD, USA, 1996.

[161] K. Pearson, "On the criterion that a given system of deviations from the probable in the case of a correlated system of variables is such that it can be reasonably supposed to have arisen from random sampling." *Philosophical Magazine Series 5*, vol. 50, no. 302, pp. 157–175, 1900.

[162] V. Vapnik, *The Nature of Statistical Learning Theory*. Springer, 1995.

[163] C. J. C. Burges, "A tutorial on support vector machines for pattern recognition." *Data Mining and Knowledge Discovery*, vol. 2, no. 2, pp. 121–167, 1998.

[164] N. Cristianini and J. Taylor, "Support vector machines and other kernel-based learning methods," *Cambridge University Press*, 2000.

[165] B. Schaokopf and A. Smola, *Learning with Kernels: Support Vector Machines, Regularization, Optimization and Beyond*. MIT Press, 2002.

[166] J. Ye and T. Xiong, "Svm versus least squares svm," *Web pdf: http://www.jmlr.org/proceedings/papers/v2/ye07a/ye07a.pdf*.

[167] T. Gestel, J. K. Suykens, and B. B. et al, "Benchmarking least squares support vector machine classifier," *Machine Learning*, vol. 54, no. 1, pp. 5–32, 2004.

[168] J. A. K. Suykens, T. V. Gestel, and J. D. B. et al, "Least squares support vector machines," *World Scientific Pub. Co., Singapore*, 2002.

[169] "Prof. andrew moore′s svm tutorial:," http://www.cs.cmu.edu/~awm/tutorials.

[170] G. H. Golub and C. F. V. Loan, *Matrix Computations*, third edition ed., U. Baltimore, MD, Ed. The Johns Hopkins University Press,, 1996.

[171] S. Alelyani, J. Tang, and H. Liu, "Feature Selection for Clustering : A Review."

[172] L. Yu and H. Liu, "Efficient feature selection via analysis of relevance and redundancy," vol. 5, pp. 1205–1224, 2004.

[173] I. Guyon, "An Introduction to Variable and Feature Selection," *Journal of Machine Learning Research*, vol. 3, pp. 1157–1182, 2003.

[174] J. a. Lee and M. Verleysen, "Unsupervised dimensionality reduction: Overview and recent advances," *The 2010 International Joint Conference on Neural Networks (IJCNN)*, pp. 1–8, Jul. 2010. [Online]. Available: http://ieeexplore.ieee.org/lpdocs/epic03/wrapper.htm?arnumber=5596721

[175] E. Cantu-Paz., "Feature subset selection, class separability, and genetic algorithms." *In Proceedings of Genetic and Evolutionary Computation Conference,*, pp. 959–970, 2004.

[176] E. Cantu-Paz, S. Newsam, and C. Kamath, "Feature selection in scientific applications," *In Proceedings of 2004 ACM SIGKDD International Conference on Knowledge Discovery and Data Mining*, pp. 788–793, 2004.

[177] G. Forman., "An extensive empirical study of feature selection metrics for text classification." *Journal of Medical Learning Research*, vol. 3, pp. 1289–1305, 2003.

[178] I. T. Jollife, "Principal component analysis." *Springer-Verlag, New York*, 1986.

[179] I. Cohen, Q. Tian, X. Sean, and Z. Thomas, "Feature Selection Using Principal Feature Analysis."

[180] D. Cai and X. He, "Orthogonal locality preserving indexing," *The 28th Annual International ACM SIGIR Conference (SIGIR'2005), Salvador, Brazil*, 2005.

[181] P. Mitra, S. Member, C. A. Murthy, and S. K. Pal, "Using Feature Similarity," vol. 24, no. 3, pp. 301–312, 2002.

[182] X. He, D. Cai, and P. Niyogi, "Laplacian Score for Feature Selection," *in NIPS*, 2005.

[183] X. H. D Cai, "Orthogonal locality preserving indexing deng," *Proceedings of the 28th annual international ACM SIGIR conference on Research and development in information retrieval. ACM*, pp. 3–10, 2005. [Online]. Available: http://sumtweets.googlecode.com/svn-history/r29/trunk/doc/report-draft.docx

[184] T. Baoping, L. I. Feng, and Q. I. N. Yi, "Fault Diagnosis Model Based on Feature Compression with Orthogonal Locality Preserving Projection," *Chinese Journal of Mechanical Engineering*, vol. 24(05):891, January 2011.

[185] M. Belkin and P. Niyogi, "Laplacian eigenmaps and spectral techniques for embedding and clustering," *Advances in Neural Information Processing Systems*, vol. 14, 2001.

[186] R. Mcquillan, A. Leutenegger, and et al., "Runs of homozygosity in european populations," *The American Journal of Human Genetics 83,*, no. 83, pp. 359–372., 2008.

[187] "Orcades images," http://www.orcades.ed.ac.uk/orcades/index.html.

[188] J. Staal, M. D. Abràmoff, M. Niemeijer, M. a. Viergever, and B. van Ginneken, "Ridge-based vessel segmentation in color images of the retina." *IEEE transactions on medical imaging*, vol. 23, no. 4, pp. 501–9, Apr. 2004. [Online]. Available: http://www.ncbi.nlm.nih.gov/pubmed/15084075

[189] J. Canny, "A computational approach to edge detection." *IEEE transactions on pattern analysis and machine intelligence*, vol. 8, no. 6, pp. 679–98, Jul. 1986. [Online]. Available: http://www.ncbi.nlm.nih.gov/pubmed/21869365

[190] H. F. Jelinek, C. Depardieu, C. Lucas, D. J. Cornforth, W. Huang, and M. J. Cree, "Towards vessel characterisation in the vicinity of the optic disc in digital retinal images," pp. 2–7.

[191] A. Rajaraman and J. D. Ullman, *Mining of Massive Dataasets, Chapter 11, Dimensionality Reduction*. Cambridge University Press,.

[192] "Inspire-avr: Iowa normative set for processing images of the retina- artery vein ratio." http://webeye.ophth.uiowa.edu/component/k2/item/270.

[193] G. Lin and M. Xie, "A face recognition algorithm using Gabor wavelet and orthogonal locality preserving projection," *2012 International Conference on Computational Problem-Solving (ICCP)*, pp. 320–324, Oct. 2012. [Online]. Available: http://ieeexplore.ieee.org/lpdocs/epic03/wrapper.htm?arnumber=6384230

[194] Y. Shekofteh, F. Almasganj, and M. M. Goodarzi, "Comparison of Linear based Feature transformations to Improve Speech Recognition Performance," *19th Iranian Conference on Electrical Engineering*, pp. 1–4, 2011.

[195] H. Wang and D. Hu, "Comparison of svm and ls-svm for regression," *International Conference on Neural Networks and Brain*, vol. 5, pp. 279–283, 2005.

[196] B. B. Mandelbrot, "The fractal geometry of nature." *Freeman, San Francisco*, 1983.

[197] K. M. Iftekharuddin, W. Jia, and R. Marsh, "Fractal analysis of tumor in brain mr images," *Machine Vision and Applications, Springer-Verlag 2003*, vol. 13, pp. 352–362, 2003.

[198] "Fractal dimension," http://math.bu.edu/DYSYS/chaos-game/node6.html.

[199] K.J.Falconer, *Hausdorff measure and dimension. In: Fractal geometry mathematical foundations and applications.* John Wiley, Cambridge, 1990.

[200] M. Schroeder, *Fractals, Chaos, Power Laws*, 6th ed. New York: W.H. Freeman and Company, 2006.

[201] N. Sarkar and B. Chaudhuri, "An efficient approach to estimate fractal dimension of textural images." *Pattern Recogn.*, vol. 23, no. 9, pp. 1035–1041, 1992.

[202] A.I.Penn, S. Thompson, S. Schnall, M. Loew, and L. Bolinger, "Fractal discrimination of mri breast masses using multiple segmentations," *Hanson KM (ed) Medical imaging 2000: Image processing. SPIE 3979*, pp. 959–966, 2000.

[203] B. R. Masters, "Fractal analysis of the vascular tree in the human retina." *Annual Review of Biomedical Engineering,*, vol. 6, pp. 427–52, 2004.

[204] A. Biswas, H. P. Cresswell, and C. S. Bing, "Application of multifractal and joint multifractal analysis in examining soil spatial variation: A review," *chapter 6, INTECH*.

[205] A. Chhabra, C. Meneveu, R. Jensen, and K. Sreenivasan., "Direct determination of the f (alpha) singularity spectrum and its application to fully developed turbulence," *Phys. Rev.*, vol. 40, pp. 5284–5294., 1989.

[206] A. N. D. Posadas, D. Gimenez, M. B. andC. M. P Vaz, and M. Flury, "Multifractal characterization of soil particle-size distributions," pp. 1361–1367.

[207] A. Giri, S. Tarafdar, P. Gouze, and T. Dutta, "Multifractal analysis of the pore space of real and simulated sedimentary rocks," *Geophys. J. Int.*, vol. 200(2), pp. 1106–1115., February, 2015.

[208] A. Wawrzaszek and W. M. Macek, "Observation of the multifractal spectrum in solar wind turbulence by ulysses at high latitudes," *Journal of Geophysics research, Space physics*, 2010.

[209] E. Ott, *Chaos in Dynamical Systems*. Cambridge University Press, 1993.

[210] J. B. Florindo and O. M. Bruno, "Fourier fractal descriptors for colored texture analysis,," *Lecture Notes in Computer Science (including subseries Lecture Notes in Artificial Intelligence and Lecture Notes in Bioinformatics)*, pp. 284–292., 2011.

[211] "Stoke," https://en.wikipedia.org/wiki/Stroke.

[212] "Lacunar stoke," http://www.drugs.com/health-guide/lacunar-stroke.html.

[213] "Cortical stoke," http://www.livestrong.com/article/194670-cortical-stroke-symptoms/.

[214] L. Lam, S. Lee, and C. Suen, "Thinning methodologies - a comprehensive survey," *IEEE TPAMI*, vol. 14, pp. 869–885, 1992.

[215] "Matlab code for finding junctions," http://www.peterkovesi.com/matlabfns/LineSegments/findendsjunctions.m.

[216] A. Wainwright and G. L. et al, "Effect of image quality, color, and format on the measurement of retinal vascular fractal dimension," *Investigative Ophthalmology & Visual Science*, vol. 51, no. 11, pp. 5525–9., 2010.

[217] E. Y. K. Ng, U. Rajendra Acharya, A. Campilho, and J. S. Suri, Eds., *Image Analysis and Modeling in Ophthalmology*. CRC press.

[218] F. Doubal, T. MacGillivray, and e. a. N. Patton, "Fractal analysis of retinal vessels suggests that a distinct vasculopathy causes lacunar stroke," *Neurology*, vol. 7, pp. 1102–1107, 2010.

# Appendix A

# Arteriole to Venule Ratio - Supplementary Results

## A.1 AVR

Chapter 5 discussed the BA analysis comparing AVR obtained by the computerised system to the reference standard (or ground truth) of measurements performed by Ob1. The mean, std, min and max of the AVR's calculated using the algorithms of Knudtson, Goatman and Patton (see section section 3.3) after vessels were classified using GMM-EM, SMIC and OLPP+Gmm-EM are shown in Table A.1. The table also gives the difference in readings between Ob1 and Ob2.

Table A.1 shows that the mean difference between AVR obtained by the thesis system and ground truth (Ob1) was smallest when vessels were classified using GMM-EM and using the Patton $(0.076)$ compared to the Goatman $(0.141)$ and Knudtson $(0.139)$ methods. The table also shows that the mean difference between Knudtson $(0.146)$ and Goatman $(0.147)$ w.r.t ground truth were almost the same and less than obtained with Patton $(0.202)$ method when vessels were classified using SMIC. Moreover a similar observation was obtained when vessels were classified using OLPP + GMM-EM approach i.e. the mean difference between Knudtson $(0.137)$ and

Goatman $(0.139)$ w.r.t. ground truth were less than that obtained with Patton $(0.192)$. These observation is in accordance with the BA plots (see section 5.3). It was also observed from Table A.1 and Figure A.1 - A.3 that the Knudtson and Goatman methods performed comparably.

BA analysis was also performed for AVR measurements by the computerised system compared to Ob2. As can be seen from Figures A.1 - A.3, the width of the LOA (i.e. the difference between the upper and lower LOA) are similar for Knudtson and Goatman w.r.t. Ob2 in all the cases. This observation was the same when analysis was performed w.r.t Ob1 (see section 5.3). This means that one can use any of the two methods (Knudtson or Goatman) interchangeably to calculate AVR

The bias of the measurements between AVR obtained with Knudtson using GMM-EM and Ob1 is $0.139$. That is, on average the first method (Knudtson) measures $0.139$ units more than the second one (Ob1). The bias increased to $0.146$ when comparing Knudtson measurements to those of Ob2. In all cases the bias obtained w.r.t. Ob1 (ground truth) was less then w.r.t. Ob2. This means that the mean difference between measurements (system-ob1) was less.

| Classifier | | Knudtson | Diff.= Knudtson-Ob1 | Diff.= Knudtson-Ob2 | Patton | Diff.= Patton-Ob1 | Diff.= Patton-Ob2 | Goatman | Diff.= Goatman-Ob1 | Diff.= Goatman-Ob2 |
|---|---|---|---|---|---|---|---|---|---|---|
| **GMM-EM** | mean (**Bias**) | 0.806 | **0.139** | **0.146** | 0.742 | **0.076** | **0.082** | 0.808 | **0.141** | **0.148** |
| | std | 0.105 | 0.136 | 0.122 | 0.084 | 0.097 | 0.121 | 0.105 | 0.136 | 0.121 |
| | min | 0.578 | -0.104 | -0.086 | 0.552 | -0.103 | -0.266 | 0.578 | -0.01 | -0.086 |
| | max | 1.087 | 0.457 | 0.407 | 0.881 | 0.316 | 0.386 | 1.087 | 0.457 | 0.407 |
| **SMIC** | mean (**Bias**) | 0.812 | **0.146** | **0.152** | 0.868 | **0.202** | **0.209** | 0.814 | **0.147** | **0.154** |
| | std | 0.096 | 0.123 | 0.108 | 0.098 | 0.129 | 0.115 | 0.096 | 0.123 | 0.109 |
| | min | 0.645 | -0.104 | -0.035 | 0.72 | -0.082 | 0.039 | 0.648 | -0.104 | -0.031 |
| | max | 1.019 | 0.432 | 0.444 | 1.071 | 0.489 | 0.552 | 1.022 | 0.432 | 0.45 |
| **OLPP + GMM-EM** | mean (**Bias**) | 0.803 | **0.137** | **0.143** | 0.858 | **0.192** | **0.198** | 0.805 | **0.139** | **0.145** |
| | std | 0.11 | 0.134 | 0.123 | 0.113 | 0.137 | 0.128 | 0.11 | 0.134 | 0.124 |
| | min | 0.626 | -0.125 | -0.059 | 0.656 | -0.051 | -0.034 | 0.63 | -0.121 | -0.059 |
| | max | 1.087 | 0.432 | 0.453 | 1.108 | 0.489 | 0.525 | 1.087 | 0.432 | 0.459 |

Table A.1: AVR results for INSPIRE-AVR images [192] calculated using Knudtson, Goatman and Patton method as describe in algorithms 1, 2 and 3 respectively in section 4.5. Results were obtained when vessels were classified by GMM-EM, SMIC and OLPP+ GMM-EM classifier. The difference in readings with Ob1 and Ob2 are also indicated. Mean, standard deviation (std.), minimum (min) and maximum (max) of AVR values are also mentioned.

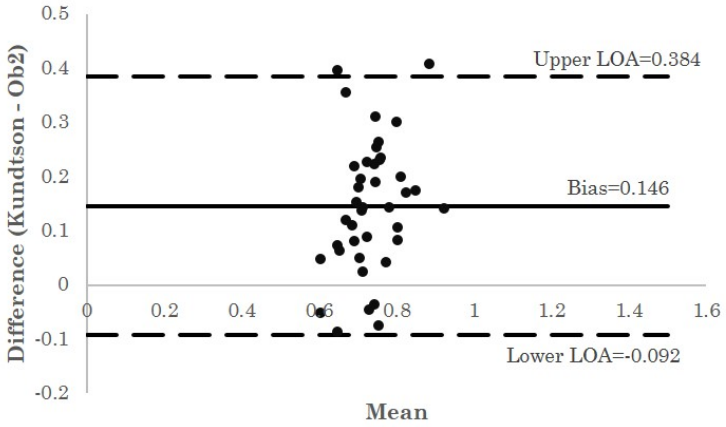


(a)

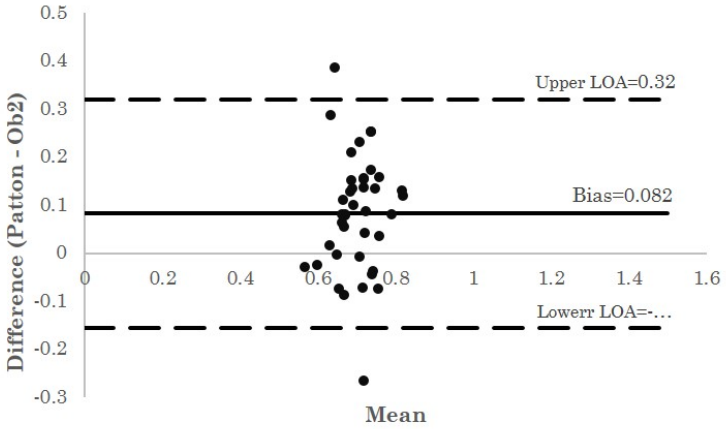


(b)

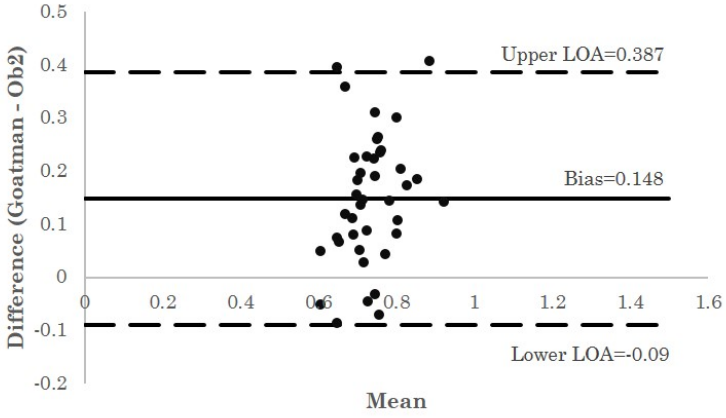


(c)

Figure A.1: Bland-Altman plots illustrating the difference and mean of the AVRs calculated by algorithms of (a) Knudtson, (b) Goatman and (c) Patton and Ob2. Results were obtained with vessels extracted from INSPIRE-AVR images and classified using GMM-EM.

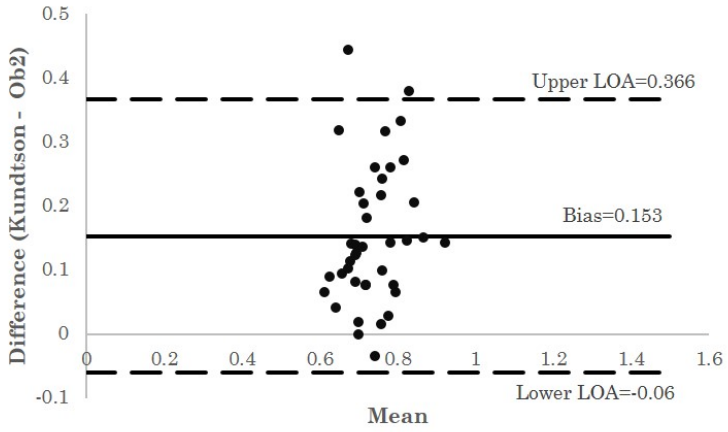


(a)

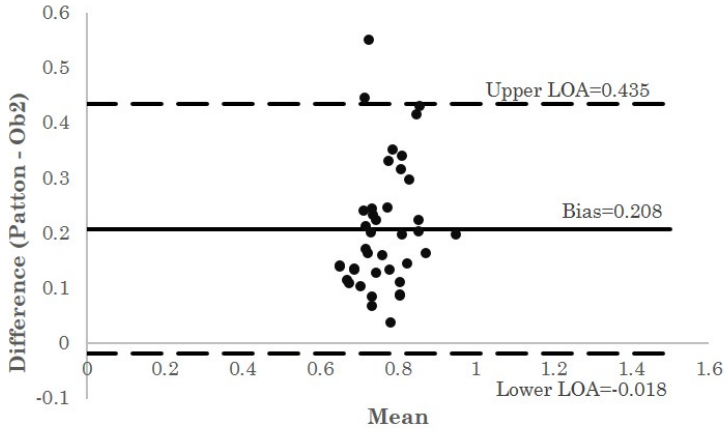


(b)

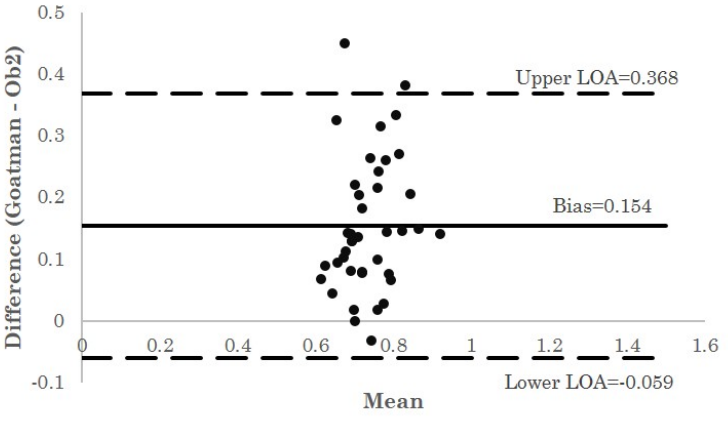


(c)

Figure A.2: Bland-Altman plots illustrating the difference and mean of the AVRs calculated by algorithms of (a) Knudtson, (b) Goatman and (c) Patton and Ob2. Results were obtained with vessels extracted from INSPIRE-AVR images and classified using SMIC.

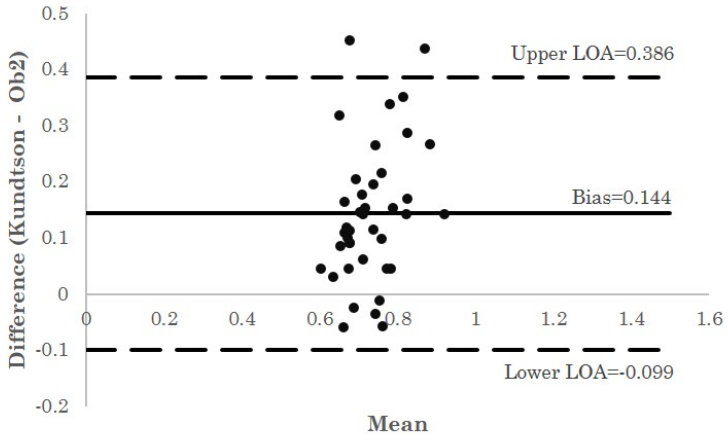


(a)

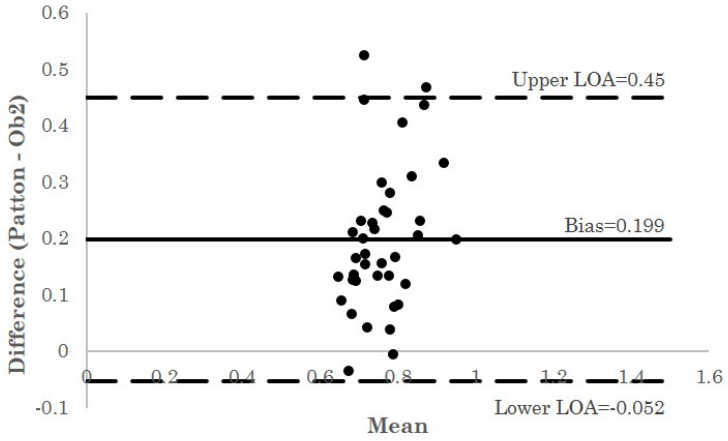


(b)

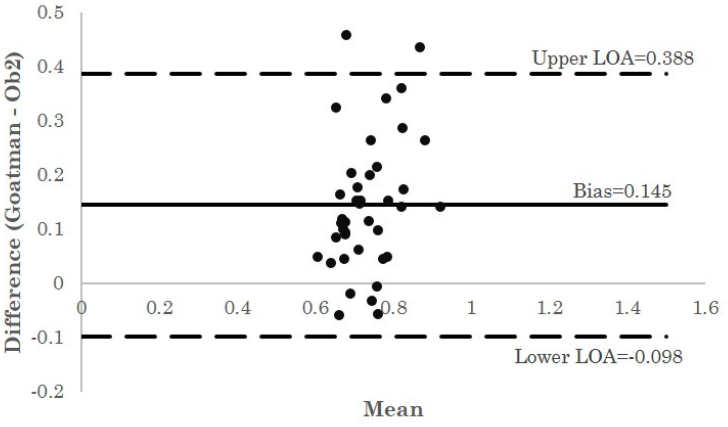


(c)

Figure A.3: Bland-Altman plots illustrating the difference and mean of the AVRs calculated by algorithms of (a) Knudtson, (b) Goatman and (c) Patton and Ob2. Results were obtained with vessels extracted from INSPIRE-AVR images and classified using OLPP in conjunction with GMMEM.

# Appendix B

# Fractal Analysis - Supplementary Results

## B.1 Multifractal Fractal Analysis

Item 1 of section 7.2.2 of Chapter 7 presented $D_0$ values obtained by MFA when noise was introduced into images segmented by observer AH. Table B.1 shows the additional results obtained by MFA on noise corrupted skeletonised images of AH segmentation. It also displays the results when noise was introduced into skeletonised and segmented versions of observer VK segmentation. The table shows the average and std of $D_0$ values of all the tested images, pathological (P) images and normal (N) images. The p-values were obtained from a student's t-test and show a significant difference existing between $D_0$ values for the two subgroups (i.e. $p \leq 0.05$).

| | | Multifractal | | |
|---|---|---|---|---|
| | | **AH-Skeletonised** | **VK-Segmented** | **VK-Skeletonised** |
| | | **D0** | **D0** | **D0** |
| **Average** | **All** | 1.93 | 1.98 | 1.98 |
| (std.) | | (0.025) | (0.04) | (0.04) |
| **Average** | **P** | 1.92 | 1.95 | 1.95 |
| (std.) | | (0.024) | (0.040) | (0.041) |
| **Average** | **N** | 1.95 | 2.01 | 2.01 |
| (std.) | | (0.01) | (0.01) | (0.01) |
| | **p-value** | 0.002 | 0.001 | 0.001 |

Table B.1: Average and standard deviation (Std.) of capacity dimension, $D_0$, (for **All**, *pathological* (**P**) and *normal* (**N**) images) calculated using MFA on the STARE image set when *salt and pepper* noise was introduced into segmented and skeletonised versions of images segmented by observers AH and VK are indicated.

## B.2 Fourier Fractal Analysis

Table B.2 presents the results of the FFA when applied to the contrast enhanced green channel STARE images with and without introduction of noise. It can be seen that in all the cases the FFD calculated for *pathological* and *normal* cases showed a significant difference between subgroups with a t-test ($p < 0.05$).

| | | FFD | | | |
|---|---|---|---|---|---|
| | | **No Noise** | **Gaussian** | **Sat and pepper** | **Poissons** |
| | | **D** | **D** | **D** | **D** |
| **Average** | **All** | 1.62 | 1.97 | 2.04 | 1.80 |
| (Std.) | | (0.050) | (0.060) | (0.054) | (0.046) |
| **Average** | **P** | 1.59 | 1.93 | 2.01 | 1.77 |
| (Std.) | | (0.034) | (0.047) | (0.042) | (0.034) |
| **Average** | **N** | 1.64 | 2.00 | 2.07 | 1.83 |
| (Std.) | | (0.048) | (0.057) | (0.050) | (0.039) |
| | **p-value** | 0.013 | 0.011 | 0.012 | 0.002 |

Table B.2: Average and standard deviation (Std.) of FFD, $D$, (for **All**, *pathological* (**P**) and *normal* (**N**) images) calculated using FFA on the STARE image set without noise (column 3) and with noise introduced into the contrast enhanced green channel images are indicated.

# Appendix C

# Publications

List of publications produced during the PhD:

**Conference Papers:**

1. Matteo Barbieri, Annalisa Barla, **Devanjali Relan**, Tom MacGillivray, Emanuele Trucco and Lucia Ballerini, **Finding a small subset of relevant features for the classification of retinal vessels**, In the Proceedings of the Medical Image Analysis Workshop 2015 SICSA Medical Imaging and Sensing in Computing Research Theme, Dundee, 27th March 2015

2. **Devanjali Relan**, L. Ballerini, E. Trucco, T. MacGillivray, **Retina Vessel Classification based on Maximization of Squared-Loss Mutual Information**, IEEE SPS-APSIPA Winter School on Machine Intelligence and Signal Processing, December 20-23, 2014

3. **D. Relan**, T. MacGillivray, L. Ballerini, E. Trucco, **Automatic Retinal Vessel classification using a Least Square- Support Vector Machine in VAMPIRE** , 36th IEEE International Conference on Engineering and Medicine and Biology (EMBC), Chicago, U.S.A, 2014.

4. **D. Relan**, T. MacGillivray, L. Ballerini, E. Trucco, **Retinal vessel classification:**

**sorting arteries and veins** , IEEE International Conference on Engineering and Medicine and Biology (EMBC), Osaka, Japan, 2013

5. E. Trucco, L. Ballerini, **D. Relan**, A. Giachetti, T. MacGillivray, K. Zutis, C. Lupascu, D. Tegolo, E. Pellegrini, G. Robertson, P.J. Wilson, A. Doney and B. Dhillon, **Novel VAMPIRE algorithms for quantitative analysis of the retinal vasculature**, in 4th IEEE Biosignals and Biorobotics Conference (ISSNIP/BRC), Rio de Janeiro, Brasil, 2013

**Abstract / Posters:**

1. Emanuele Trucco, R Annunziata, L Ballerini, E Pellegrini, S J MacKenna, T MacGillivray, T Pearson, **D Relan**, G Robertson, A Doney, B Dhillon, J Cameron, **VAMPIRE: Vessel Assessment and Measurement Platform for Images of the REtina**, Dundee Medical Image Analysis Workshop 2015, Part of the SICSA Medical Imaging and Sensing in Computing Research Theme, 27th March 2015

2. Tom MacGillivray, Gavin Robertson, **Devanjali Relan**, Enrico Pellegrini, Kris Zutis et al, **VAMPIRE: Vasculature Assessment and Measurement Platform for Images of the REtina**, In proceeding of: SINAPSE Annual Scientific Meeting, Edinburgh, UK 2014

3. T MacGillivray, **D. Relan**, G Robertson, C Gray, E van Beek, **Retinal Imaging in Clinical Research: joint activities across Edinburgh and Dundee**, Centre for In Vivo Imaging Science (Edinburgh Imaging), LAUNCH EVENT, 21st Nov 2012.

4. **D. Relan**, T. MacGillivray, C. Gray, L. Ballerini, E. Trucco, **Retinal Vessel Classification In Fundus Imaging Using VAMPIRE For Biomarker Identification**, NHS Scotland, 31st Oct. 2013: Won Second Prize

**Book Chapters:**

1. Emanuele Trucco, Andrea Giachetti, Lucia Ballerini, **Devanjali Relan**, Alessandro Cavinato, Tom MacGillivray, **MORPHOMETRIC MEASUREMENTS OF THE RETINAL VASCULATURE IN FUNDUS IMAGES WITH VAMPIRE**, Chapter 3, Wiley series in Biomedical Image Understanding, Methods and Applications, Page 91-111, John Wiley & Sons, Inc

2. **Devanjali Relan**, L. Ballerini, E. Trucco, T. MacGillivray, **Retina Vessel Classification based on Maximization of Squared-Loss Mutual Information**, Machine Intelligence and Signal Processing, Advances in Intelligent Systems and Computing, Springer 2016, pp 77-84